Plasmonic Nanoantennas

Dissertation
der Mathematisch-Naturwissenschaftlichen Fakultät
der Eberhard Karls Universität Tübingen
zur Erlangung des Grades eines
Doktors der Naturwissenschaften
(Dr. rer. nat.)

vorgelegt von
Herr Jiyong Wang
aus Henan/China

Tübingen
2017

Gedruckt mit Genehmigung der Mathematisch-Naturwissenschaftlichen Fakultät der Eberhard Karls Universität Tübingen.

Tag der mündlichen Qualifikation: 21.09.2017
Dekan: Prof. Dr. Wolfgang Rosenstiel
1. Berichterstatter: Prof. Pierre-Francois Brevet
2. Berichterstatter: Prof. Dietrich R.T. Zahn

Acknowledgements

This Ph.D dissertation is impossible to be achieved without the supports from many people. It's my pleasure to express the appreciation here.

First of all, I would like to thank my supervisors: Prof. Dr. Pierre-Michel Adam in University of Technology of Troyes and PD. Dr. Dai Zhang in University of Tuebingen. Thank Pierre for his creative ideas, always encouragement and the support without reservation. Thank Dai for her meticulous scholarship, always help and thoughtful guidance. I appreciate all her contributions of time and efforts to make my Ph.D experience colourful and productive. They two become the most ideal and powerful combination to me: crease mind, full of freedom and everything self-organized on one side, feet down-to-earth, rigorous check-up and tight schedule on the other. It's really my honour to work with them together.

The members of AK Meixner group have been a source of friendship, good advice and collaborations during my stay in Tuebingen. I would like to thank Prof. Dr. Alfred. J. Meixner for his profound knowledge, fruitful discussion and optimistic attitude towards life. I am especially grateful for the time working together with Dr. Anke Horneber, a colleague with amazing hands-on capability, active mind and enthusiastic kindness. I am also thankful for the help from Marius van den Berg, Kathrin Eitel, Jan Rogalski, Xiao Wang, Kai Braun, Frank Wackenhut and other group members.

I would like to acknowledge the group members in Troyes as well. I thank my colleague and friend Feng Tang for all his help in my personal and professional live. I very appreciated the help from Sergei Kostcheev, an engineer with solid nano-fabrication skills and working patience. Thank him for the training hand by hand. I would also acknowledge honorary our kind director Prof. Dr. Renaud Bachelot, humorous engineer Regis Deturche, rigorous couple Dr. Anne-Laure Baudrion and Jeremy Beal, and other colleagues in LINO. My deep

appreciation also goes out to the Chinese circle in Troyes. It is all their kindness, help and trust makes my abroad live happy and wonderful.

Many works in this dissertation have been done in collaboration with other research groups. Regarding the dark-field scattering measurement, I would like to thank the colleagues from Prof. Dr. Monika Fleischer group in Applied Physics Department, University of Tuebingen. For the nonlinear optical response simulation, especially on SHG, I would like to acknowledge Dr.Jeremy Butet and Prof. Dr. Olivier J. F. Martin group in Nanophotonics and Metrology Laboratory, Swiss Federal Institute of Technology (EPFL). With respect to the linear optical response simulated via Green tensor method, I express special thank to Dr. Gaëtan Lévêque group in Institute of Electronics, Micro-electronics and Nano-technology, Lille, France.

Finally, I would like to thank my family for their support in all my pursuits. Special thanks to my wife for her love, trust and encouragement. Without their help, it’s impossible to complete this work.

Abstract

The material-, size- and shape-tuned plasmonic nanostructures are fabricated by electron-beam lithography (EBL). Their linear and nonlinear optical responses are detected via dark-field scattering microscope and scanning confocal optical microscope, respectively. The elastic scattering offers the fingerprints for the localized surface plasmon resonances (LSPRs) of plasmonic nanoparticles (NPs), which give the assistance to the enhancement of nonlinear optical signals, such as second-harmonic generation (SHG) and two-photon photoluminescence (TPL).

SHG from various types of nanoantennas is studied subsequently. The excitation polarization dependent far-field radiation of SHG shows a flipping effect, which is attributed to the resonant excitation condition and the SH phase interferenceduring the size of NP changes. The results clearly point out that the characterization of electromagnetic hot-spots using nonlinear optical processes is not straightforward, and that a competition between different contributions from parameters, such as polarization, geometry and resonance, to the enhancement often occurs.

The radiations of metallic photoluminescence (MPL) in the weak and strong electromagnetic field are investigated systematically, involving experiments and theoretical modelling. In the weak excitation, it is found that the MPL consists of two emission channels: the particle plasmons (PPs) and the electron-hole (e-h) pair radiation channels. PPs are excited via Auger scattering of photo-excited d-band holes, the radiative decay of which develops the former components. The latter derives from the plasmon-enhanced radiative decay process of e-h pairs. A model of total emission quantum efficiency (TEQE) involving both contributions is established, to quantify the radiative emission capability per e-h pair, and explain the size effect regarding the MPL difference between the bulk and the NPs. The experiment results and the theoretical model supply a new approach to predict MPL.

In the strong excitation, avalanche multiphoton photoluminescence (AMPL) is observed from the strong coupled Au-Al heterodimers once the incident beam exceeds critical laser intensity or incident polarization is closing to the longitudinal excitation. The emission intensity turns out approximately more than one order of magnitude larger and encounters dramatic spectral changes. The physic mechanism can be well explained via Keldysh's rate equations in strong field. It is interpreted that AMPL derives from the recombination of avalanche ionized hot carriers seeded by multiphoton ionization (MI). The MI is greatly assisted by the dramatic local field of coupled Au-Al nanoantennas at the excitation stage. The threshold of optical breakdown can be evaluated via two-temperature model (TTM), taking the source term into account. At the emission step, a linear relationship between the power law exponent coefficient and the emitted photon energy is experimentally observed. The giant AMPL intensity can be evaluated as a function of the local field environment and the thermal factor of hot carriers. The spectral change from the LSPR modulated profile to the one that indicates the direct recombination from hot e-h pairs is explained by the diminishment of d-band hole scattering rate as the carriers' temperature increases.

Contents

Nomenclature

1. EBL: electron-beam lithography

2. NP: nanoparticle

3. SPP: surface plasmon polariton

4. SPR: surface plasmon resonance

5. LSP: localized surface plasmon

6. LSPR: localized surface plasmon resonance

7. PP: particle plasmon

8. SHG: second-harmonic generation

9. THG: third-harmonic generation

10. SFG: sum-frequency generation

11. PL: photoluminescence

12. TPL: two-photon photoluminescence

13. MPL: metallic photoluminescence

15. MPPL: multiphoton photoluminescence

16. AMPL: avalanche multiphoton photoluminescence

17. TEQE: total emission quantum efficiency

18. TTM: two-temperature model

19. NA: numerical aperture

20. FWHM: full width at half maximum

21. e-h: electron-hole

22. PI: photoionization

23. MPI: multiphoton ionization

24. TI: tunnelling ionization

25. GTM: Green tensor method

26. BEM: boundary element method

27. FDTD: finite-difference time-domain

28. SIE: surface integration equation

29. LP: longitudinal polarization

30. TP: transverse polarization

31. SEM: scanning electron microscope

32. PVD: physicalvapourdeposition

33. UV: ultra-violet

34. NIR: near infrared

35. ITO: Indium tin oxide

Chapter 1 Introduction

Metallic nanostructures exhibit fascinating linear and nonlinear optical properties when they are excited by an incident light. Localized surface plasmons (LSPs) generated by a collective oscillation of electrons in the conduction bands offer the possibility of enhancing and concentrating electrical field in a subwavelength volume, which enable the nanostructures to act similar to antennas in the microwave or radiowave regime.[1-4] Their potential applications in a variety of fields ranging from biosensing,[5-7] light harvesting systems,[8] to field effect transistors[9, 10] have motivated researchers to understand their fundamental physical properties and the optical processes. The influences of localized surface plasmon resonances (LSPRs) on the linear optical properties of plasmonic nanoantennas, such as absorption, scattering, and single-photon photoluminescence emission have been intensively investigated.[11-15] To study the electromagnetic field amplitude in the so-called hot-spots, corresponding to the areas where the incident field intensity is enhanced by several orders of magnitude, researchers relied on several spectroscopic techniques such as photoluminescence emission from the metallic nanostructures,[16-18] fluorescence or Raman signal from molecules which are immobilized on the nanoantenna surface,[19, 20] and also electron energy loss spectroscopy.[21, 22]More recently, the observation of nonlinear optical processes from plasmonic nanoantennas starts to attract increasing attention. Various nonlinear optical processes, such as second-harmonic generation (SHG),[23-26] two-photon photoluminescence (TPL),[24, 27, 28] third and higher harmonics generation,[29, 30] as well as multiphoton photoluminescence (MPPL)[31] have been investigated. Compared to linear optical processes, the generation of nonlinear optical signals requires a much higher excitation field. Plasmonic nanoantennas can be used for the excitation of these optical processes since the field intensity at the fundamental wavelength is increased in their vicinities thanks to the LSPR.[32-34]

In this thesis, the plasmonic nanoantennas are systematically investigated, involving their fabrication and characterization. Electron-beam lithography (EBL) is employed as the main technique for the fabrication, since it supplies high resolution, regular shapes and reproducible nanostructures. The material is focused on Au and Al because of their tunable LSPR in the visible range. The researching objects include single monomers and dimers with varying sizes, inter-distances, shapes and dielectric environment. The optical properties include the elastic scattering and nonlinear responses such as SHG and metallic photoluminescence (MPL). The corresponding simulation methods such as Mie theory, boundary element method, finite-difference time-domain and surface integration equation are studied at the same time, treating the linear and nonlinear optical responses. Furthermore, new optical properties will appear when the plasmonic nanoantennas are exposed in a strong electromagnetic field, where thermal diffusion of electron and lattice becomes an innegligible issue. On the one hand, the hot carriers will be generated. The optical properties, such as the dielectric function and spectral properties of LSPRs, will be modified, as the electron population and distribution will be changed. Special attention should be paid on the threshold of optical breakdown. On the other hand, the hot carriers-mediated photoemission could be made full use in the surface enhanced spectroscopy and microscopy, with a clear electron dynamics in mind. Hot carrier- mediated photo-excitation and -emission is an interesting topic, which involves the knowledge of nonlinear optics, plasmonics and thermodynamics.

The thesis is organized as follows:

Chapter 1 - introduction. The state of art and the organization of the whole thesis will be presented here.

Chapter 2 - theoretical background. In this section, theories related to the following topics will be introduced: plasmonics, Mie scattering, mechanical analogues, SHG, TPL, electron dynamics, two-temperature mode (TTM), and Keldysh rate equations.

Chapter 3 - materials and methods. In this section, setups for the fabrication, linear and nonlinear optical characterization will be presented. The simulating methods will be introduced as well.

Chapter 4 - elastic scattering of Au and Al nanoantennas. The elastic scatterings of Au/Al monomers, Au-Au/Al-Al homodimers and Au-Al heterodimers will be presented and compared experimentally and theoretically, which paves the paths for the following chapters.

Chapter 5 -Far-field SHG radiation from various types of nanoantennas. The excitation polarization dependent far-field radiation of SHG shows a flip as the size of Au nanoantenna changes, which is analysed from the aspects of resonant excitation condition and SH phase interference.

Chapter 6 - MPL radiation channels in a weak electromagnetic field. In this section, the emission mechanism of MPL is discussed based on the classical description and beyond.

Chapter 7 - avalanche multiphoton photonluminescence (AMPL) in a strong electromagnetic field. The MPPL in a strong electromagnetic where the thermal effects cannot be neglected is studied in terms of dramatic changes in the emission intensity and spectral profile, comparing with the case in a weak excitation.

Chapter 8 - conclusions and outlooks. The summaries are made for each chapter and the future work is proposed.

The linear optical responses give the hints of LSPRs for specific nanostructures, which is the base of the whole following work. However, our main efforts will be focused on the nonlinear optical properties and the influences of LSPRs on the nonlinear optical responses. The frame of the whole thesis is organized as Fig. 1.1:

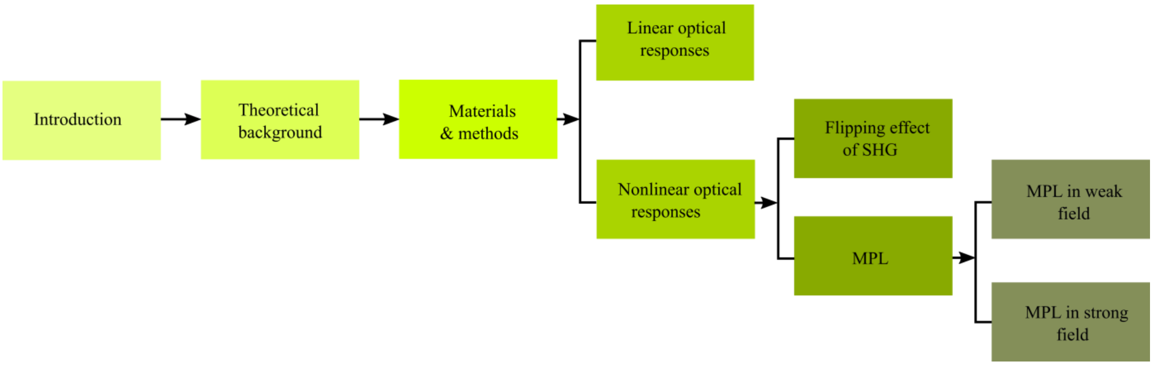

Figure 1.1 The frame of the thesis.

Chapter 2 Theoretical background

In this section, the fundamental theories and models which will be used in following sections are presented. The theories cover different topics, such as plasmonics, elastic scattering, nonlinear optics, electrodynamics and thermodynamics.

2.1 Plasmonics fundamentals

2.1.1 Propagating surface plasmon

Surface plasmon polaritons (SPPs) are electromagnetic excitations propagating at the interface between a dielectric and a conductor, evanescently confined in the perpendicular direction.[1] These surface waves arise via the coupling of the electromagnetic fields to oscillations of the conductor's electron plasma. To be simple, a single and flat interface between a conducting half space (Z<0) described by a dielectric function $\varepsilon_1(\omega)$ and a dielectric half space (Z>0) with positive real dielectric constant ε_2 sustains the SPPs, as shown in Fig. 2.1(a). Maxwell's equations can be solved using TM polarization, which finally gives the dispersion relation of SPPs propagating at the interface:[1]

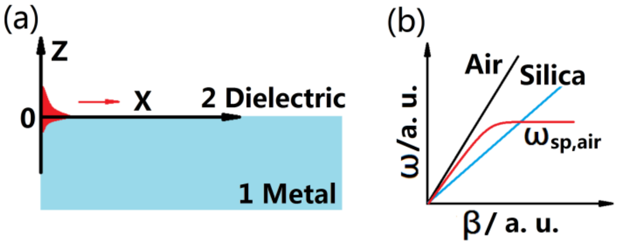

Figure 2.1 (a) The single interface between a metal and a dielectric for calculating SPPs. (b) The dispersion relation of SPPs at the interface between a metal and different dielectric mediums.

$$\beta = k_0 \sqrt{\frac{\varepsilon_1 \varepsilon_2}{\varepsilon_1 + \varepsilon_2}} \tag{2.1}$$

where β is the propagation constant in the direction of propagation ($x$axis); [1] k_0 is the wave vector in the vacuum; ε_1 is the real part of dielectric constant of metal and ε_2 is the dielectric constant of dielectric medium. The dielectric function of the free electron where the damping is negligible can be expressed as:[1]

$$\varepsilon(\omega) = 1 - \frac{\omega_p^2}{\omega^2} \tag{2.2}$$

where $\varepsilon(\omega)$ is predominantly real; $\omega_p^2 = ne^2/\varepsilon_0 m$ is the plasma frequency of the free electron gas. Inserting equation (2.2) into (2.1), when β approaches infinity, the frequency approaches the surface plasmon frequency $\omega_{sp} = \omega_p/\sqrt{1+\varepsilon_2}$ .The wave vector in the dielectric medium is $k_d = w/c\sqrt{\varepsilon_2}$. From eq. (2.1) we can clearly see that the propagation constant β is always greater than k_d, as shown in Fig. 2.1(b) the SPP dispersion curve lies to the right of the light line of the same dielectric (air as an example in Fig. 2.1(b). The dephase leads to the impossibility of excitation of SPP.[1] However, the presence of a second dielectric layer owning a higher dielectric constant than the first can fix such phase-matching problem, as shown the dispersion relations in Fig. 2.1(b) (here silica is the second dielectric). The common SPP coupling schemes includes prism coupling such as Kretschmann and Otto configurations and grating coupling.[1] Other coupling schemes such as illumination in the near-field and employing the scattering of NPs are also feasible for the excitation of SPPs.

2.1.2 Localized surface plasmon

One of the important characteristics of SPPs is propagating along the interface of metal and dielectric on the scale of skin depths. LSPs, however, are non-propagating excitations of the conduction electrons of metallic NPs coupled to the external electromagnetic field,[1] as shown in Fig. 2.2. The curved surface of NPs excerts an effective restoring force on the driven electrons, so that a resonance can arise, leading to field amplification both inside and in the near-field zone outside the NPs.[1] This resonance is namely LSPR.

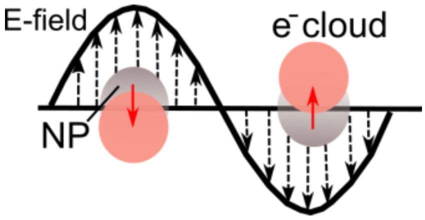

Figure 2.2 The excitation of localized surface plasmons

The polarizability α of a nanosphere with radius of a can be calculated in quasi-static approximation by solving the Laplace equation and boundary conditions:[1]

$$\alpha = 4\pi a^3 \frac{\varepsilon_1 - \varepsilon_2}{\varepsilon_1 + 2\varepsilon_2} \tag{2.3}$$

The resonance takes place when the Frohlich condition is met: $Re[\varepsilon_1(\omega)] = -2\varepsilon_2$ in accordance with the eq. (2.3). The energy of LSPR depends on the material ($\varepsilon_1(\omega)$ function), the size (parameter a for the sphere) and the shape of NPs.

The LSPR can be measured via the far-field extinction, absorption or scattering spectra in practice. One of the most popular theoretical models for simulating such linear optical responses is the Mie theory.

2.2 Linear optical responses based on Mie theory

In 1908 Mie developed a complete theory to calculate the scattering and absorption of electromagnetic radiation by a homogenous sphere.[35] The approach is known as Mie theory, which expands the internal and scattered fields into a set of coefficients. Later these coefficients were expanded for more complex shapes, such as coated sphere, anisotropic sphere and infinite cylinder.[35] Here a homogenous sphere is taken for an example to show how Mie theory works for calculating the scattering and absorption cross section.

According to the Mie theory, the coefficients of the field inside the particle are:[35]

$$\begin{cases} c_n = \dfrac{\mu_1 j_n(x)[xh_n^{(1)}(x)]' - \mu_1 h_n^{(1)}(x)[xj_n(x)]'}{\mu_1 j_n(mx)[xh_n^{(1)}(x)]' - h_n^{(1)}(x)[mxj_n(mx)]'} \\ d_n = \dfrac{\mu_1 m j_n(x)[xh_n^{(1)}(x)]' - \mu_1 m h_n^{(1)}(x)[xj_n(x)]'}{m^2 j_n(mx)[xh_n^{(1)}(x)]' - \mu_1 h_n^{(1)}(x)[mxj_n(mx)]'} \end{cases} \tag{2.4}$$

and the scattering coefficients are:[35]

$$\begin{cases} a_n = \dfrac{m^2 j_n(mx)[xj_n(x)]' - \mu_1 j_n(x)[mxj_n(mx)]'}{m^2 j_n(mx)[xh_n^{(1)}(x)]' - \mu_1 h_n^{(1)}(x)[mxj_n(mx)]'} \\ b_n = \dfrac{\mu_1 j_n(mx)[xj_n(x)]' - j_n(x)[mxj_n(mx)]'}{\mu_1 j_n(mx)[xh_n^{(1)}(x)]' - h_n^{(1)}(x)[mxj_n(mx)]'} \end{cases} \tag{2.5}$$

where m is the refractive index of the sphere relative to the ambient medium. $x = ka$ is the size parameter, a the radius of the sphere and $k = 2\pi/\lambda$ is the wave number and λ the wavelength in the ambient medium. μ_1 is the relative magnetic permeability of metallic sphere to dielectric medium. The functions $j_n(z)$ and $h_n^{(1)}(z) = j_n(z) + iy_n(z)$ are spherical Bessel functions of order n (n=1,2,…) and of the given arguments, $z = x$or mx respectively. Primes represent derivatives with respect to the argument.[35]

The scattering, extinction and absorption cross section then can be calculated as:[35]

$$\begin{cases} \sigma_{sca} = \dfrac{2\pi a^2}{x^2} \displaystyle\sum_{n=1}^{\infty} (2n+1)(|a_n|^2 + |b_n|^2) \\ \sigma_{ext} = \dfrac{2\pi a^2}{x^2} \displaystyle\sum_{n=1}^{\infty} (2n+1) Re(a_n + b_n) \\ \sigma_{abs} = \dfrac{2\pi a^2}{x^2} \left| \displaystyle\sum_{n=1}^{\infty} (2n+1)(-1)^n (a_n - b_n) \right|^2 \end{cases} \tag{2.6}$$

A Au nanosphere with a diameter of 100 nm in air is taken for an example. When the nanosphere is excited by a plane wave with the polarization along the x axis and the propagation direction along the z axis, Fig. 2.3(a) shows the calculated extinction, absorption and scattering cross sections, and Fig. 2.3(b) shows the near-field electromagnetic field distributions.

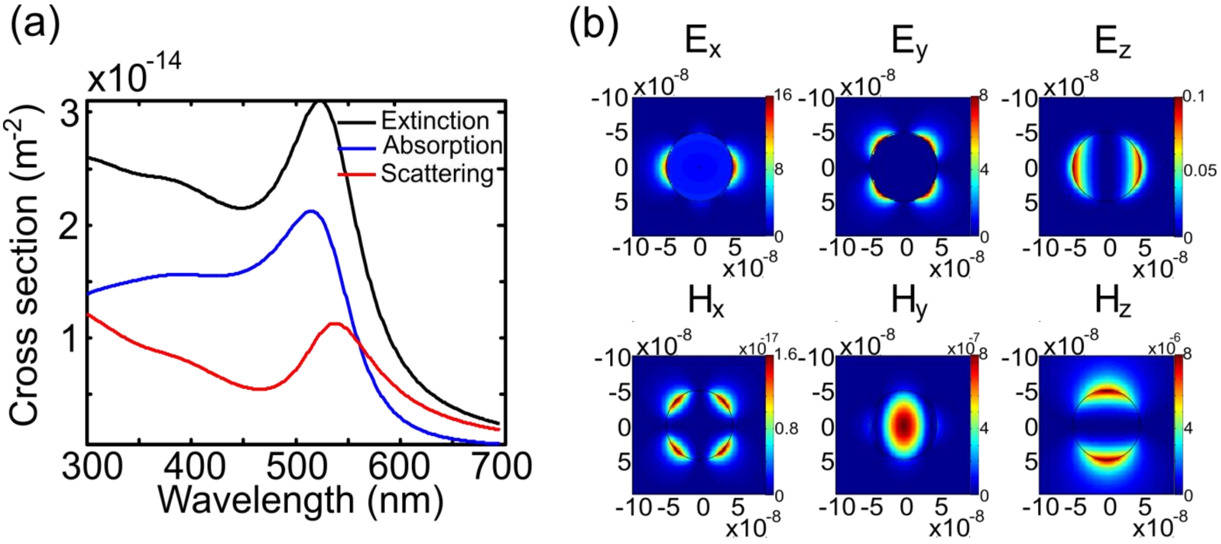

Figure 2.3 The extinction, absorption, scattering cross sections (a) and the electromagnetic near-field distributions (b) of a gold sphere with a diameter of 100 nm which is calculated according to the Mie theory. The dielectric medium is air. The excitation wave is propagating along the z axis and is polarized along the x axis.

2.3 Phenomenological approach to light-matter interactions

When a metallic NP is excited by an electromagnetic wave, the polarization can be analogically regarded as the mechanical vibration under the periodic driving force for a damped single degree-of-freedom system. The Lorentzian oscillator is basically a special application based on such classical vibration theory, where the driving force is replaced by electric force. Such mechanical analogues are necessary to the understandings of the LSPRs, the resonant excitation, the driven amplitude and phase during the light-matter interactions and especially the couplings between two or more NPs. In the following, we start with a single degree-of-freedom system, and then generalize the main conclusions to the multiple degree-of-freedom system.

The differential equation of motion for the single degree-of-freedom system with viscous damping show Fig. 2.4(a), when the excitation is a force $F = F_0 \sin \omega t$ applied to the mass, is:[36]

$$m\ddot{x} + c\dot{x} + kx = F_0 \sin \omega t \tag{2.7}$$

The solution can be obtained:[36]

$$\frac{x}{F_0/k} = \frac{\sin(\omega t - \theta)}{\sqrt{(1-\omega^2/\omega_n^2)^2 + (2\zeta\omega/\omega_n)^2}} = R_d \sin(\omega t - \theta) \tag{2.8}$$

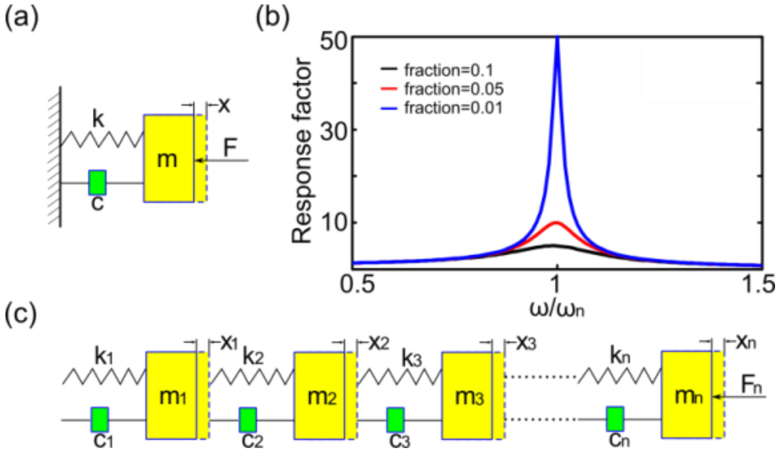

Figure 2.4 (a) Single degree-of-freedom vibration with driving force and viscous damping. (b) Dimensionless response factor R_d as a function of ω/ω_n. (c) Multiple degree-of-freedom vibration with driving force and viscous damping.

where $\omega_n = \sqrt{k/m}$ the natural frequency of an undamped oscillator; $\zeta = c/c_{cr} = c/(2\sqrt{km})$ is fraction of critical damping; $\theta = \tan^{-1}(2\zeta\,\omega/\omega_n/1 - \omega^2/\omega_n^2)$ is the phase angle. R_d is a dimensionless response factor giving the ratio of the amplitude of the vibratory displacement to the spring displacement that would occur if the force F were applied statically. At very low frequencies R_d is approximately equal to 1, and it has a peak near the natural frequency. At very high frequencies, it approaches 0. Fig. 2.4(b) shows R_d as a function of ω/ω_n.

A nanostructure consisting multiple NPs can be analogized a linear multiple degree-of-freedom system, as shown in Fig. 2.4(c). The coupling effect can be simplified as springs which connect two point masses in vicinity. Similar expression of each mass replacement can be generalized as:[36]

$$x_k = \sum_{i=1}^{n} \frac{D_{ki}}{\omega_i^2} \frac{F_i}{m_i} R_i \sin(\omega t - \theta_i) \tag{2.9}$$

where x_k: displacement of structure in kth degree-of-freedom; n: number of degree-of-freedom, including those of the foundation; D_{ki}: amplitude of in kth degree-of-freedom in ith normal mode; F_i: generalized force for ith normal mode; m_i: generalized mass for ith normal mode; R_i: response factor for ith normal mode; θ_i: phase angle for ith normal mode.

The normal mode indicates the solutions for the differential equations without external forces, which satisfy the orthogonalities.

2.4 Nonlinear optical properties of nanoparticles

When the excitation electric field becomes intensive, especially in the focus volume of ultrafast laser pulses, the polarization induced involves not only linear responses, but also nonlinear parts. Wave equation of nonlinear polarization can be obtained by solving the Maxwell equations:[37, 38]

$$\nabla^2 \boldsymbol{E} - \mu_0 \frac{\partial^2 \boldsymbol{D_L}}{\partial^2 t^2} = \mu_0 \frac{\partial^2 \boldsymbol{P_{NL}}}{\partial^2 t^2} \tag{2.10}$$

where$\boldsymbol{D_L} = \varepsilon_0 \boldsymbol{P_L} = \varepsilon_0 \chi^{(1)} \boldsymbol{E}$ is the linear electric displacement vector. $\boldsymbol{P_{NL}}$is the nonlinear polarization, which can be expressed by:[37, 38]

$$\boldsymbol{P_{NL}} = \varepsilon_0 (\chi^{(2)} \boldsymbol{E}^2 + \chi^{(3)} \boldsymbol{E}^3 + \cdots) \tag{2.11}$$

$\chi^{(1)}$, $\chi^{(2)}$, $\chi^{(3)}$,…, are the first three terms of susceptibilities, which are described as a second, third, fourth,… rank of tensor in practice. $\chi^{(1)}$ leads to the linear optical responses, as introduced in previous section. Higher orders of susceptibilities lead to the study of nonlinear optics, such as second-harmonic generation (SHG), third harmonic generation (THG), two-photon photoluminescence (TPL), four waves mixing (FWM) and so on, which becomes the hot topics nowadays. The wave equation (2.10) implies not only the derivation of nonlinear polarizations, but also the generation of new electric fields induced by such nonlinear polarizations.

In later sections, discussions on SHG and TPL are focused, to introduce their physical origins, and quantitative calculating methods. In the following chapters, corresponding experiments and simulations are presented.

2.4.1 Second-harmonic generation

The application of second-order nonlinear optical techniques such as SHG and sum frequency generation (SFG) for studying properties of various small particles has been a subject of considerable interest. SHG is a coherent scattering process in terms of the second order of susceptibility. From the quantum view, SHG can be considered as "absorbing" two photons with the frequency of ω from a lower energy level to a virtual energy level followed by the generation of one photon with doubled frequency 2ω,[39] as shown in Fig. 2.5. It is well known that SHG is forbidden in the bulk of centro-symmetric media within the dipolar approximation.[38] Nevertheless, this symmetry is broken at the interface between two centro-symmetric medias, and SHG can arise from metallic nanostructure surfaces.[23, 40-42] In 1968, Bloembergen et. al. attributed SHG from centro-symmetric material to bulk contribution induced by electric quadrupole and magnetic dipole, as well as surface contribution arising from dipole approximation at the interface where symmetric break exists.[43] The surface SHG becomes more and more predominant as the ratio of surface to volume increases. With respect to NPs, the bulk SHG can be neglected due to the high surface to volume ratio.[23, 24]

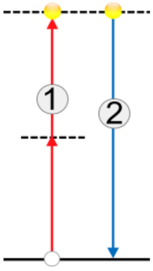

Figure 2.5 An illustrative description of the SHG process. "Absorbing" two photons with the frequency of ω from the ground state through virtue energy states (step 1), electrons finally scatter one photon with doubled frequency 2ω (step 2).

The first step to derive the SH field is to calculate the vector potential$\boldsymbol{A}(\boldsymbol{r})$. Within Lorentz gauge, the vector potential $\boldsymbol{A}(\boldsymbol{r})$ for SHG arising from a current-density source $\boldsymbol{J}(\boldsymbol{r}')$ or nonlinear polarization $\boldsymbol{P}^{(2\omega)}(\boldsymbol{r}')$ is given by:[40]

$$\boldsymbol{A}(\boldsymbol{r}) = \frac{1}{c}\int \frac{exp(iK_1|\boldsymbol{r}-\boldsymbol{r}'|)\boldsymbol{J}(\boldsymbol{r}')}{|\boldsymbol{r}-\boldsymbol{r}'|}d\boldsymbol{r}' = \frac{K}{i}\int \frac{exp(iK_1|\boldsymbol{r}-\boldsymbol{r}'|)\,\boldsymbol{P}^{(2\omega)}(\boldsymbol{r}')}{|\boldsymbol{r}-\boldsymbol{r}'|}d\boldsymbol{r}' \tag{2.12}$$

where r and r' denote the field and source points respectively; $K_1 = n(2\omega)2\omega/c = n(2\omega)K$ is the magnitude of the scattered wave vector $\boldsymbol{K}_1 = K_1\vec{r}$; K is the magnitude of vacuum SH wave vector; and n is the refraction index of the medium. The electromagnetic field can then be deduced by:[44]

$$\begin{cases} \boldsymbol{H}^{(2\omega)}(\boldsymbol{r}) = \dfrac{\boldsymbol{B}^{(2\omega)}(\boldsymbol{r})}{\mu_1} = \dfrac{\nabla\times\boldsymbol{A}^{(2\omega)}(\boldsymbol{r})}{\mu_1} \\ \boldsymbol{E}^{(2\omega)}(\boldsymbol{r}) = \dfrac{-i}{2\omega\varepsilon_1\mu_1}\nabla\times\boldsymbol{B}^{(2\omega)}(\boldsymbol{r}) = \dfrac{-i}{2\omega\varepsilon_1\mu_1}\nabla\times(\nabla\times\boldsymbol{A}^{(2\omega)}(\boldsymbol{r})) \end{cases} \tag{2.13}$$

So now the problem turns to how to solve the nonlinear polarization $\mathbf{P}^{(2\omega)}(\boldsymbol{r}')$. According to the previous discussion, the bulk SHG can be neglected if the investigating object is NPs. The surface contribution is :

$$\boldsymbol{P}_s = \delta\big(r - h(r)\big)\boldsymbol{\chi}_s\colon\boldsymbol{EE} \tag{2.14}$$

$\delta\big(r-h(r)\big)$ denotes that the surface topography depicted by $h(r)$; $\boldsymbol{\chi}_s$ is the surface susceptibility, which is described as a third rank tensor including 27 elements. The non-zero independent elements decrease considering the surface symmetry. Taking crystal direction (0,0,1) of C_{4v} for example, three independent elements of surface susceptibility are:[45]

$$\begin{cases} \chi_{s,xxz} = \chi_{s,yyz} = \chi_{s,xzx} = \chi_{s,yzy} \\ \chi_{s,zxx} = \chi_{s,zyy} \\ \chi_{s,zzz} \end{cases} \tag{2.15}$$

Assuming that the surface is parallel to xy plane, z direction is represented by '⊥', and x or y direction '∥'. Then the three independent non-zero susceptibility elements are: $\chi_{s,\parallel\parallel\perp} = \chi_{s,\parallel\perp\parallel}$, $\chi_{s,\perp\parallel\parallel}$, $\chi_{s,\perp\perp\perp}$.

The surface susceptibility is expressed as$\mathbf{P}_s = \mathbf{P}_{s,\perp\perp\perp} + \mathbf{P}_{s,\perp\|\|} + \mathbf{P}_{s,\|\perp\|}$, with[45]

$$\begin{cases} \mathbf{P}_{s,\perp\perp\perp} = \chi_{s,\perp\perp\perp} E_r^2 \hat{r} \\ \mathbf{P}_{s,\perp\|\|} = \chi_{s,\perp\|\|}\left(E_\theta^2 + E_\emptyset^2\right)\hat{r} \\ \mathbf{P}_{s,\|\perp\|} = 2\chi_{s,\|\perp\|}(\hat{\theta} E_r E_\theta + \hat{\emptyset} E_r E_\emptyset) \end{cases} \tag{2.16}$$

E_r, E_θ, $E_\emptyset$ are fundamental electric field components in spherical coordinate, and $\hat{r}$, $\hat{\theta}$, $\hat{\emptyset}$ are unit vectors. The conversion of electric field from the Cartesian coordinate to the spherical coordinate can be obtained via:[44]

$$\begin{pmatrix} \boldsymbol{E}_r \\ \boldsymbol{E}_\theta \\ \boldsymbol{E}_\emptyset \end{pmatrix} = M \begin{pmatrix} \boldsymbol{E}_x \\ \boldsymbol{E}_y \\ \boldsymbol{E}_z \end{pmatrix} \tag{2.17}$$

with

$$M = \begin{pmatrix} \sin\theta\cos\emptyset & \sin\theta\sin\emptyset & \cos\theta \\ \cos\theta\cos\emptyset & \cos\theta\sin\emptyset & -\sin\theta \\ -\sin\emptyset & \cos\emptyset & 0 \end{pmatrix} \tag{2.18}$$

2.4.2 Two-photon photoluminescence

The metallic photoluminescence was observed by Mooradian from copper and gold in 1969.[18, 46]In his experiment, excited by 488 nm monochromatic light, a broad peak centered near the interband absorption edge was observed. They attributed this peak to direct radiative recombination of electrons near the Fermi level with holes in the first d band. Due to the high density-of-state, the interband transition will preferentially occur near the specific symmetry points of the Brillouin zone. Rosei developed quantitative model to calculate the inter-conduction-band transitions involving the Fermi surface.[47-49] G. T. Boyd et. al. measured the single-photon and multiphoton-induced luminescence from silver, copper and gold with both smooth and rough surfaces.[18] A classical model combining the Fresnel coefficients and Rosei's interband transitions was put forward for the smooth metallic film to calculate the photoluminescence intensity. Regarding the rough film, the Fresnel factors were corrected by macroscopic local-field factors, where the rough surface was modelled as hemispheroids situating on a smooth metallic film.[18]

MPL can be described as a three-step process,[24, 50, 51] as shown in Fig. 2.6. (1) Absorption stage. An electron from the ground state is promoted to the excited state by absorbing one (leading to single-photon-induced PL) or more photons (leading to MPPL), leaving a hole behind. (2) Relaxation stage. Excited electrons reach the thermal equilibrium stage via electron-electron, electron-phonon scattering. (3) Emission stage. The electrons in the emitting state recombine with the holes in the ground state in step (1) either radiatively in terms of PL (solid arrow) or non-radiatively in terms of heat dissipation (dashed arrow).

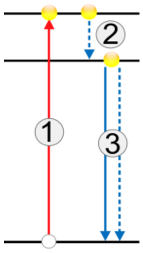

Figure 2.6 PL generation described by a three-step process: absorption, relaxation and emitting steps. Electrons in the emitting state recombine with holes in the ground state either radiatively in terms of PL (solid arrow) or non-radiatively in terms of heat dissipation (dashed arrow).

However, for MPPL the absorption stage can't be described using the above simple statement. Taking TPL from gold crystal for an example, two different absorbing mechanisms were proposed: coherent two-photon absorption process and two sequential one-photon absorption processes, as depicted in Fig. 2.7(a) and (b), respectively. [52]

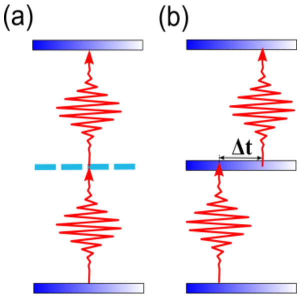

Figure 2.7 Two absorption models for explaining the excitation mechanism of TPL. (a) Coherent two-photon absorption; (b) Two sequential one-photon absorptions.

The former model involves the simultaneous absorption of two photons through a virtual intermediate state. However, the latter model argues that the excitation involves two sequential one-photon absorption steps through real intermediate states. Xiaofang Jiang et. al proved that in gold nanorods the excitation process arises from two sequential one-photon absorptions by power dependence measurements.[52] To be exact, e.g. for gold, two sequential one-photon absorptions are further understood that the first photon is absorbed by sp electron below Fermi level E_f, which is followed by intraband transition and excited to the state above E_f. The second photon excites the d band electron to the sp band through interband transition, which finally creates a hole in d band at the same time.[27, 53] The whole process can be illustrated through Fig. 2.8, which shows the intraband transition (step 1) and interband (step 2) transition of electrons near the symmetry points of X (Fig. 2.8 (a)) and L (Fig. 2.8 (b)) of the first Brillouin zone of gold due to the high joint density of state. [18, 53-55]

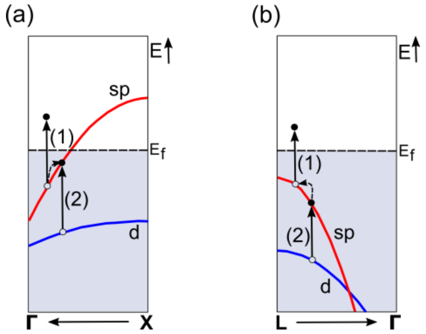

Figure 2.8 Two sequential one-photon absorption involving the intraband transition (step 1) and interband (step 2) transition of electrons near the symmetry points of X (a) and L (b) of the first Brillouin zone of gold.

The hole in the d band and electron in the sp band can recombine radiatively to yield TPL directly. In the following section, the classical model for calculating the PL intensity which is based on the work of Rosei, G. T. Boyd et. al will be introduced first.[18] As to the PL of NPs, due to the local field enhancement and the role that surface plasmon plays, optional channels exist which allow the rediative decay through different surface plasmon modes. This will be explained from the quantum field theory based on the work done by T. V. Shahbazyan.[56-58]

The single-photon-induced luminescence from a derivate width dz at a depth z into metal can be described as :[18]

$$I_{em}(\omega_2)dz = I(\omega_1, z)Y_{1abs}Y_RY_{em}dz \tag{2.19}$$

where ω_1 and ω_2 are the incident and luminescence frequencies, respectively; $I(\omega_1, z)$ is the excitation intensity at a depth of z; Y_{1abs} is the absorption probability for a single-photon at ω_1; Y_R is the relaxation probability of the electrons and holes from the excited states to the emitting states; Y_{em} is the emission probability of radiative recombination at ω_2. The excitation intensity is given by[18]

$$I(\omega_1, z) = I_0(\omega_1)|L(\omega_1)|^2 \exp(-\alpha\omega_1 z) \tag{2.20}$$

where $I_0(\omega_1)$ is the source intensity; $|L(\omega_1)|^2$ is the Fresnel transmission coefficient at ω_1 and α is the absorption coefficient. For TPL, $I(\omega_1, z)Y_{1abs}$ becomes $I(\omega_1, z)^2Y_{2abs}$, where Y_{2abs} is the two-photon absorption probability at $2\omega_1$. The emission probability is given by[18]

$$\begin{aligned} Y_{em} \propto\ & \omega_2 d\omega_2 d\Omega|L(\omega_2)|^2 \exp(-\alpha\omega_2 z) \\ & \times \iint \{|\boldsymbol{p}_2|^2\delta[E - E_U(\boldsymbol{k})]\delta[E - \hbar\omega_2 - E_L(\boldsymbol{k})]f_e(E)f_h(E \\ & - \hbar\omega_2)\}\, dEd^3\boldsymbol{k} \end{aligned} \tag{2.21}$$

where E_U and E_L are the energies of the upper electron and lower hole bands, respectively; $\boldsymbol{p}_2$ is the momentum matrix element between the bands; $|L(\omega_2)|^2$ is the Fresnel transmission coefficient at ω_2; the function f_e and f_h are the electron- and hole-population distributions, respectively, which result from the excitation and relaxation processes.

Because of the largest joint density of states for emission, the above integration over the Brillouin zone can be simplified by only taking the regions close to the symmetric points into account. Further approximations can be made by considering only the direct recombination between electrons and holes, and by that momentum matrix elements are independent of $\boldsymbol{k}$ over such regions. Thus the PL intensity can be described as:[18]

$$I_{em}(\omega_2) \propto F(\omega_1, \omega_2) \int dE[D(E, \hbar\omega_2)f_e(E)f_h(E - \hbar\omega_2)] \tag{2.22}$$

where $(\omega_1, \omega_2) = \omega_2|L(\omega_1)|^2|L(\omega_2)|^2 z_0(\omega_1, \omega_2)$, $z_0(\omega_1, \omega_2) = 1/[\alpha(\omega_1) + \alpha(\omega_2)]$, $D(E, \hbar\omega_2) = \int d^3\boldsymbol{k}\ \delta[E - E_U(\boldsymbol{k})]\delta[E - \hbar\omega_2 - E_L(\boldsymbol{k})]$. $D(E, \hbar\omega_2)$ is the joint density of state, which can be evaluated by the energy of the Bloch state near the L and X symmetry points.[18]

With the development of fabrication techniques of nanostructures, the PL of metallic NPs starts to attract more and more attention. The LSPR modulated PL was observed by many studies.[24, 50, 59, 60] The role of surface plasmon during the emission process is still debating. T. V. Shahbazyan et. al established a model for calculating plasmon-assisted metallic PL from the view of quantum field theory.[51, 57] In the following section, we will briefly introduce his theory, with the purpose of applying part of the conclusions for understanding the experiments, which will be demonstrated in Chapters 6 and 7.

In addition to the spontaneous emission via the direct recombination of electrons and holes, surface plasmon modes are excited by the non-radiative decay via Auger scattering of d band holes.[51] This supplementary channel actually influences strongly the generation of PL from metallic NPs, due to the efficient radiative decay rate of resonant plasmons, as reported in several previous studies.[24, 50] The surface plasmon mediated scattering rate of conduction band electron is[57, 58]

$$\gamma_e^s(E) = 9\pi \frac{E_0^2}{\omega_s}\frac{E}{E_F}\left(\frac{E-\omega_s}{E_F}\right)^{1/2}[1-f(E-\omega_s)] \tag{2.23}$$

where $E_0 = (2mR^2)^{-1}$, R is the radii of nanosphere; ω_s is the surface plasmon frequency; $f(E)$ is the Fermi-Dirac distribution. For multiphoton-induced PL from gold NPs, the scattering rate of d hole to conduction band is[57, 58]

$$\gamma_h^s(E) = -\frac{9e^2\mu^2}{m^2(E^{cd})^2R^3} Im \frac{N(E^c-E)+f(E^c)}{\varepsilon_s(E^c-E)} \tag{2.24}$$

where$E^{cd} = E^c - E^d$ is the energy difference between conduction band and d band; μ is the interband dipole matrix element; $N(E)$ is the Bose distribution.

$$\varepsilon_s(\omega) = \varepsilon_d(\omega) - \omega_p^2/\omega(\omega + i\gamma_s) + 2\varepsilon_m \tag{2.25}$$

where ε_m is the dielectric constant of embedded medium; ε_d is the dielectric constant considering the interband contribution; ω_p is the bulk plasmon frequency and γ_s is the damping constant.

Equations (2.23) and (2.24) are the critical results to understand the role surface plasmon plays on the generation of single-photon- and multiphoton-induced PL.

2.5 Thermal properties

When the ultrafast pulse laser is employed, the heat becomes an inevitable issue for optical measurements due to the high peak intensity and ultrafast repetition rate. Many previous studies investigated the electrodynamics in the condition that the metallic film or NPs avoid from being damaged. Nevertheless, at or beyond the threshold of optical breakdown induced by laser pulses, the nonlinear optical signals involving SHG and TPL show lots of new characteristics. The nonlinear optical responses in the strong electromagnetic field have not been well explored yet. The full interpretation of the novel nonlinear effects requires the considerations of electrodynamics or more generalized thermodynamics.

2.5.1 Electron-thermalization dynamics

Once the metal surface situates in the focus of ultra-fast pulse laser, the original Fermi-Dirac distribution of electron is perturbed. Electrons in the outermost surface experience a transient high temperature, and thus in a highly non-equilibrium state.[61] Excited electrons in the conduction band above E_f will undergo sub-picosecond electron thermalization via electron-electron scattering. The initial non-Fermi electron distribution will be thermalized to hot Fermi distribution when electrons reach the thermal equilibrium. The electron dynamics can be studied by the transient transmissivity and reflectivity as well as time-resolved photoemission spectroscopy on thin films or NPs in the colloidal solution.[62, 63] After the electron thermalization, due to the temperature gradient, the thermal energy transfers to the lattice via electron-phonon coupling on a time scale of several tens of picoseconds.[61-63] As time goes on, hot lattices will diffuse into deeper part of the metal via phonon-phonon interactions.[21] The evolution of electron-phonon coupled system usually is explained by the two-temperature model (TTM).[62, 64, 65]

(a) TTM

The time-resolved electron and lattice temperatures can be obtained via the TTM with source term:[62, 64-67]

$$\begin{cases} C_e(T_e)\dfrac{\partial T_e}{\partial t} = -G(T_e - T_l) + S(z,t) \\ C_l\dfrac{\partial T_l}{\partial t} = G(T_e - T_l) \end{cases} \tag{2.26}$$

where C and T are the heat capacities and temperatures of the electrons and lattice as represented by the subscripts e and l. The energy diffusion terms are omitted, considering the ultrafast repetition rate and strong radiation field. The electron-phonon coupling constant G and electron capacity are temperature dependent, according to the literature.[66] The source term $S(z,t)$ is expressed as:[62]

$$S(z,t) = I(t)(1-R) \times \frac{\exp\left(-\frac{z}{\lambda_0+\lambda_{ball}}\right)}{(\lambda_0 + \lambda_{ball})\left(1 - \exp\left(-\frac{d}{\lambda_0+\lambda_{ball}}\right)\right)} \tag{2.27}$$

where $I(t)$ is the laser intensity, R is the reflectivity, λ_0 is the optical absorption depth, λ_{ball} is the ballistic range, and d is the height of Au NPs. The reflectivity and the absorption depth are determined by the Fresnel expressions: $R = (f_1 - 1)^2 + {f_2}^2/(f_1 + 1)^2 + {f_2}^2$ and $\lambda_0 = \lambda/4\pi f_2$, where f_1, f_2 are the real and imaginary parts of refractive index of Au excited at the fundamental wavelength λ.

(b) Time resolved electron/phonon temperature detection

For the very small induced temperature changes, the contribution of the thermalized distribution to the transient reflection and transmission is directly proportional to the electron temperature change.[61, 68]A linear relationship between $\Delta R/R$ ($\Delta T/T$) and electron temperature T_e provides a simplified way for the non-contact detection of transient electron temperature. The transient reflectivity or the transmission can be detected via the time-resolved pump-probe technique.

The changes of transient optical properties such as reflectivity and transmissivity are also related to the changes of the real and imaginary part of dielectric constant[61, 68]

$$\begin{cases} \frac{\Delta R}{R} = \frac{\partial lnR}{\partial \varepsilon_1} \Delta\varepsilon_1^{'} + \frac{\partial lnR}{\partial \varepsilon_2} \Delta\varepsilon_1^{'}{}' \\ \frac{\Delta T}{T} = \frac{\partial lnR}{\partial \varepsilon_1} \Delta\varepsilon_1^{'} + \frac{\partial lnR}{\partial \varepsilon_2} \Delta\varepsilon_1^{'}{}' \end{cases} \tag{2.28}$$

where R, T denote the reflection and transmission of probe signals; $\varepsilon_1^{'}, \varepsilon_1^{'}{}'$ are the real and imaginary parts of dielectric constant of the metal.

The changes of imaginary part of dielectric constant can be related to the changes of the electron distribution in accordance with the model developed by Roseiet. al for (cw) thermodulation measurements.[47, 48, 54] By assuming that the matrix element is constant, the change of the imaginary part of dielectric function can then be given by[48, 68]

$$\Delta\varepsilon_1^{'}{}'(\hbar\omega) = \frac{1}{(\hbar\omega)^2} \int D(E, \hbar\omega) \Delta\rho(E) dE \tag{2.29}$$

where$D(E, \hbar\omega)$ is the joint density of state and $\Delta\rho$ is the change of electron distribution.

The change of the real part of the dielectric constant can be computed using the Kramers-Kronig relationship[61]

$$\Delta\varepsilon_1^{'}(\hbar\omega) = \frac{2}{\pi} P \int \frac{\hbar\omega^{'} \Delta\epsilon_1^{''}(\hbar\omega^{'})}{(\hbar\omega^{'})^2 - (\hbar\omega)^2} d(\hbar\omega^{'}) \tag{2.30}$$

where P denotes a Cauchy principle value integral which extends over the whole frequency range.

2.5.2 Photoionization in strong electromagnetic field

With the development of laser techniques, the pulses down to time scale of sub-picosecond have been widely used, especially in the field of nonlinear optics. When the metallic nanostructure or other solids are illuminated by sub-picosecond laser pulses, the absorbed energy by electrons become difficult to diffuse to the lattice, and finally the hot carries and optical breakdown which are neglected in weak excitation become apparent.

Optical breakdown is described as a strong local ionization of the medium, where the plasma reaches densities beyond the critical value (between 10^{20} and 10^{22} electrons/cm³).[69, 70] Once the plasma critical density is achieved, energy is very efficiently absorbed from the light pulse, and the local plasma temperature increases dramatically. It is believed that optical breakdown in condensed material is proceeded by avalanche ionization, in which initial (seed) unbound electrons in the target material are accelerated by the laser electric field to create a cascade of free electrons through collisions.[69] Thus in order for avalanche ionization to occur, the necessary process is to supplying the ‘seed’ electrons. The seed electrons can be generated through defect and impurity, or photoionization (PI) where the electrons are from the valance band. The former induced optical breakdown is usually referred as electron impact ionization and subsequent avalanching, which becomes considerable when the duration of pulse is longer (>ps). When the duration is at sub-picosecond regime, rather than existing defects or impurities, PI results in what is commonly referred to as self-seeded avalanche ionization.[70] Depending on the properties of incident pulse and the target material, two contributions to PI are always involved: multiphoton ionization (MPI) and tunneling ionization (TI).[71]

The MPI takes place when the material’s band gap energy exceeds that of a single photon of incident laser. The electrons in the valence band have such probability that they are excited to the conduction band by absorbing multiple photons. The excitation process can be illustrated as Fig. 2.9(a).[72] The second form of PI is TI, which occurs when a strong electric field is presented. The Coulomb potential can be suppressed enough so that an electron is able to tunnel through the reduced barrier, as shown in Fig. 2.9(b).[72] These bound electrons become free and many of them serve as ‘seed’ electrons for avalanche ionization. In the Fig. 2.9, the black solid curves represent the Coulomb potential, the red vertical arrows absorbed photons, the red fluctuated curves the laser pulses, the solid circles excited electrons, the empty circles holes, and the red dashed curves the tunnelling effects.

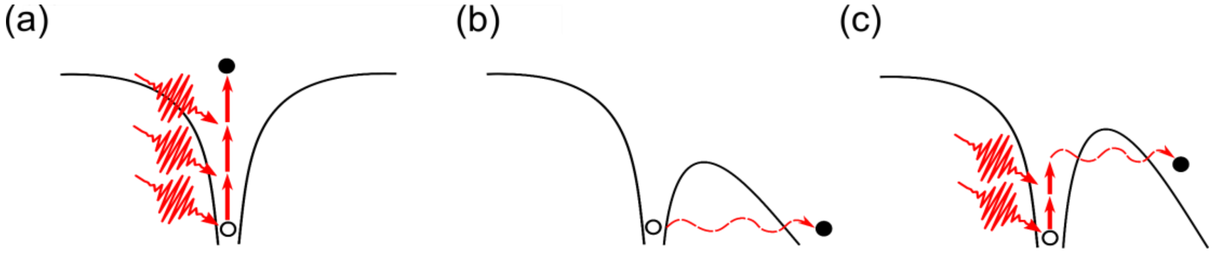

Figure 2.9 (a) Multiphoton ionization. (b) Tunneling ionization. (c) The photoionization induce by the combination of multiphoton absorption and tunneling effect. The black solid curves represent the Coulomb potential, the red vertical arrows absorbed photons, the red fluctuated curves the laser pulses, the solid circles excited electrons, the empty circles holes, and the red dashed curves the tunneling effects.

The exact contribution of each process can be referred from Keldysh Theory. The electron tunnelling rate without MPI contribution is expressed:[71]

$$W_{tun} = \frac{2}{9\pi^2}\frac{E_g}{c}\left(\frac{m_e E_g}{\hbar^2}\right)^{3/2}\left(\frac{e\hbar F}{{m_e}^{1/2}{E_g}^{3/2}}\right)^{5/2} \times \exp\left[-\frac{\pi}{2}\frac{{m_e}^{1/2}{E_g}^{3/2}}{e\hbar F}\left(1-\frac{m_e\omega^2 E_g}{8e^2F^2}\right)\right] \tag{2.31}$$

where E_g is the band gap; m_e is electron effective mass; e is the electron charge; ω is the angular frequency of the laser; F is the electric field strength, defined as $F = \sqrt{2I/en\varepsilon_0}$, I is the intensity of incident beam, n is the refractive index and ε_0 is the permittivity in free space.

The MPI rate equation without the electron tunnelling effect is given:[71]

$$W_{mpi} = \frac{2}{9\pi^2}\omega\left(\frac{m_e E_g}{\hbar^2}\right)^{3/2}\phi\left[\left(2\left(\frac{E_g^*}{\hbar\omega}+1\right)-\frac{2E_g^*}{\hbar\omega}\right)^{1/2}\right] \times \exp\left[2\left(\frac{E_g^*}{\hbar\omega}+1\right)\left(1-\frac{e^2F^2}{4m_e\omega^2E_g}\right)\right]\times\left(\frac{e^2F^2}{16m_e\omega^2E_g}\right)^{\left(E_g^*/\hbar\omega+1\right)} \tag{2.32}$$

whereE_g^* is the effective ionization potential given by $E_g^* = E_g + e^2F^2/4m_e\omega^2$; ϕ denotes Dawson's Integral and is given by $F(x) = e^{-x^2}\int_0^x e^{-t^2}dt$. The full rate equation involving electron tunnelling effect and multiphoton absorption is given:[71]

$$W_{full} = \frac{2}{9\pi^2}\left(\frac{\sqrt{1+\gamma^2}}{\gamma}\frac{m_e\omega}{\hbar}\right)^{3/2} Q(\gamma,\frac{E_g^*}{\hbar\omega}) \times \exp\left\{-\pi\left(\frac{E_g^*}{\hbar\omega}+1\right)\times\frac{\left[K\left(\frac{\gamma}{\sqrt{1+\gamma^2}}\right)-E\left(\frac{\gamma}{\sqrt{1+\gamma^2}}\right)\right]}{E\left(\frac{1}{\sqrt{1+\gamma^2}}\right)}\right\} \tag{2.33}$$

where

$$Q(\gamma,x) = [\pi/2K(\frac{1}{\sqrt{1+\gamma^2}})]^{1/2} \times \sum_{n=0}^{\infty}\exp\left\{-\pi\left[K\left(\frac{\gamma}{\sqrt{1+\gamma^2}}\right)-E\left(\frac{\gamma}{\sqrt{1+\gamma^2}}\right)\right]n/E\left(\frac{1}{\sqrt{1+\gamma^2}}\right)\right\} \times \phi\{[\pi^2(2<x+1>-2x+n)\big/2K\left(\frac{1}{\sqrt{1+\gamma^2}}\right)E(\frac{1}{\sqrt{1+\gamma^2}})]^{1/2}\} \tag{2.34}$$

E_g^* takes a new form $E_g^* = \frac{2}{\pi}E_g\frac{\sqrt{1+\gamma^2}}{\gamma}E(\frac{1}{\sqrt{1+\gamma^2}})$. In equations from (2.33) to (2.34), K and E are complete elliptic integrals of the first and second kind. γ is referred as Keldysh parameter, which is defined as:[71]

$$\gamma = \frac{\omega}{e}[\frac{m_e c n \varepsilon_0 E_g}{I}]^{1/2} \tag{2.35}$$

where$c$ is the speed of light; other parameters have the same definitions as above.

γ is usually used to determine which contribution (mulitiphoton ionization or tunneling ionizaiton) is dominant during the process of photoionization induced avalanching. The critical value is 1. When γ is smaller than 1, PI is dominated by tunnelling effects. On the other hand, when γ is greater than 1, then MPI will dominate. The last case is when γ is almost equal to 1. In this case, both processes will be involved, as shown in Fig. 2.9(c).

Chapter 3 Materials and methods

The linear and nonlinear optical responses of the material-, size- and shape-tuned plasmonic nanostructures are systematically investigated. The materials studied here involve gold and aluminum, whose surface plasmon resonances can be tunable ranging from visible to infrared and from ultraviolet to visible spectral regimes, respectively. In order to explore the plasmonic coupling effects of different systems, dimers involving homodimers (Au-Au dimers and Al-Al dimers) and heteodimers (Au-Al dimers) were investigated by varying the size and spacing separately. The nanostructures were fabricated by electron-beam lithography (EBL) followed by lift-off. The linear optical properties of plasmonic nanostrtures were characterized by extinction microscopy and dark-field scattering microscopy. The nonlinear optical characteristics were investigated by confocally scanning optical microscopy combined with femtosecond pulses laser. The thermodynamics of nanostructure was studied in terms of excitation power dependence and polarization dependence.

In parallel, theoretical modelling on the linear, nonlinear optics and thermodynamics were performed. Linear optical responses such as the extinction, scattering or absorption of plasmonic nanostructures of different dimensions, shapes and interdistances were simulated by various approaches, such as Mie theory, Green tensor method (GTM), boundary element method (BEM) and finite-difference time-domain (FDTD) method. The nonlinear optical responses such as SHG and TPL were analyzed with the assistance of a surface integral equation (SIE) method. Different models on the electrodynamics and thermodynamics were adapted and realized by Matlab program in order to obtain in-depth physical interpretations.

3.1 Fabrication

Nanostructures can be fabricated by various approaches currently developed, such as EBL, Focused-ion-beam, Nano-print lithography and chemical synthesis.[73] Because of the high resolution, stable reproducibility, homogenous in producing nano-scale and complex shapes with pre-designable spacing, EBL becomes more and more popular in the field of nano fabrication.[74-76] The normal EBL process involves resist coating, exposure, development, evaporation and lift-off, as illustrated in Fig. 3.1.

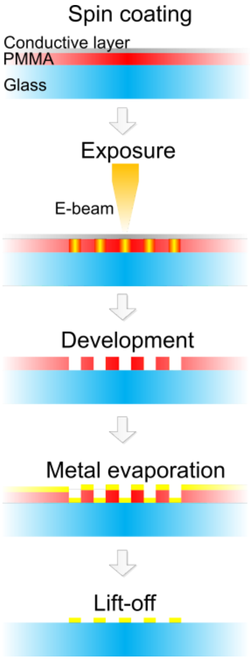

Figure 3.1 The electron-beam lithography processes

To be exact, after cleaning by acetone and isopropanol in an ultrasonic bath, the substrateis coated with a layer of electron-sensitive resist (Poly-Methyl-Metacrylate (PMMA)) 950K diluted in Methyl-Iso-Butyl-Ketone (MIBK) at 30g/L in a spin-coater (spinning speed: 3000 rpm, acceleration speed: 4000 rpm/s, duration: 30 s).[24] The thickness of the resist is expected to be 3 times thicker than the height of designed nanostructures, according to the empirical curve of the spinning speed versus the film thickness. After soft baking (convection oven at 170 °C for 3 hours), spin-coat a thin layer of conductive polymer (Espacer 300Z from Showa Denko Europe) to prevent charge accumulation during the exposure.[24] Then the resist is exposed with pre-designed patterns by electron beam. After the conductive polymer is removed in water, the written patterns are developed via a solution of MIBK (diluted with isopropanol).[24]At the development step, the resists at exposed areas are removed. Afterwards a physical vapour deposition (PVD) process is used to coat the sample with a 2~3 nm thick adherent layer (Cr or TiO_2) and expected metal layer. The sample is finally immersed in acetone for more than 3 hours to lift-off the resist residuals.[24] Fig. 3.2 shows some examples of nanostructures fabricated by single EBL processes.

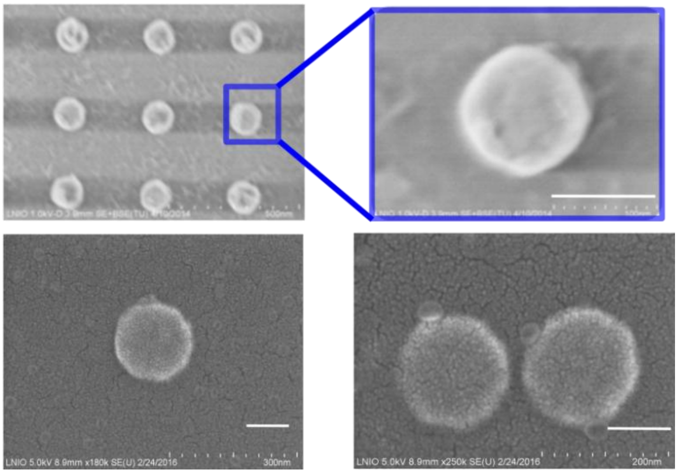

Figure 3.2 SEM images for the nano discs fabricated by EBL. Upper rows: Au discs assemble with diameter of 100 nm; lower rows: single Al monomer and Al-Al dimer with the diameter of 160 nm. Al-Al homodimer has an edge-to-edge gap of 20 nm. The white scale bars in the figure represent 100 nm.①

In order to fabricate the heteodimer, the second-time EBL is mandatory, which is referred to the double EBL technique. The basic procedure is shown in Fig. 3.3.

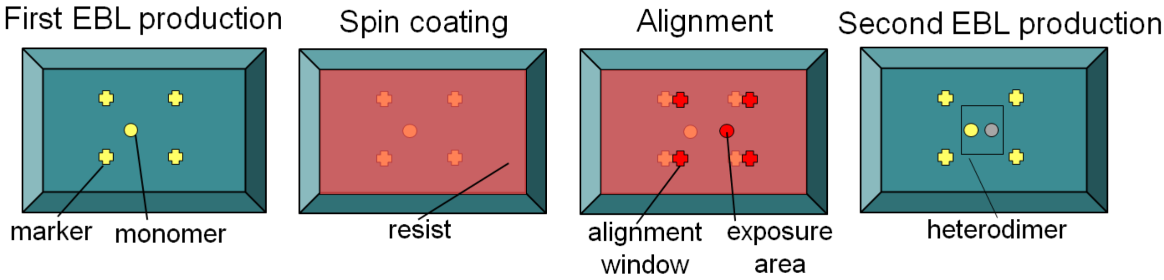

Figure 3.3 The double electron-beam lithography processes.

---

①The SEM images in Fig. 3.2 lower row are provided by Dr. Anne-Laure Baudrion in University of Technology of Troyes.

To conduct the double EBL, it's necessary to maintain the aligning markers during the first lithography process, due to the high requirement of gap between two particles. After covering the first lithographical nanostructure with a layer of e-resist, the alignment process allows us to only scan the area of aligning window which has reciprocal patterns as the aligning marker. The second exposure, PVD and lift-off are preceded after the alignment. Fig. 3.4 shows some SEM images of Au-Al heterodimers. The diameters of Au and Al disc are 80 and 120 nm. The edge-to-edge gaps are 20, 40, 60, 80, 100 and 250 nm, respectively.

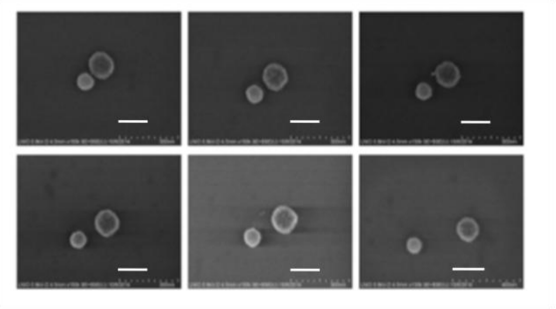

Figure 3.4 SEM images of Au-Al heterodimers. The diameters of Au and Al disc are 80 and 120 nm. The edge-to-edge gaps are 20, 40, 60, 80, 100 and 250 nm. The white scale bars represent 100 nm ①

3.2 Characterization of linear optical responses

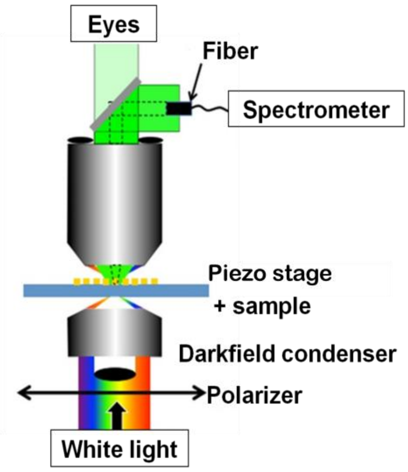

Figure 3.5 The scheme of dark-field scattering microscopy.②

---

① SEM images in Fig. 3.4 are provided by Dr. Anne-Laure Baudrion in University of Technology of Troyes.
② Fig. 3.5 is from Dr. Anne-Laure Baudrion in University of Technology of Troyes.

A home-built dark-field scattering microscopy, as illustrated in Fig. 3.5,is used to measure the linear optical properties of the single nanostructure. For the single nanostructure measurement, the interdistance between each structure should be at least 5 um to prevent the plasmonic coupling effects. The sample, placed on an inverted microscope (Nikon Ti-U), is illuminated from the air side by a halogen lamp through a dark-field condenser (NA 0.8-0.95).[24] The scattered light coming from the nano-structures is collected from the glass side by a 20x objective with a numerical aperture (NA) of 0.5 and sent to a spectrometer (Ocean Optics QE 65000) through a pin-hole (200 μm diameter).[24] The measured intensity curves is background corrected (using intensity curves measured in an unstructured area of the sample) and normalized by dividing the (dark-current corrected) lamp spectrum. In front of the entrance of the white light, a polarizer can be installed as a complementary element in order to obtain linear excitation polarization dependence.

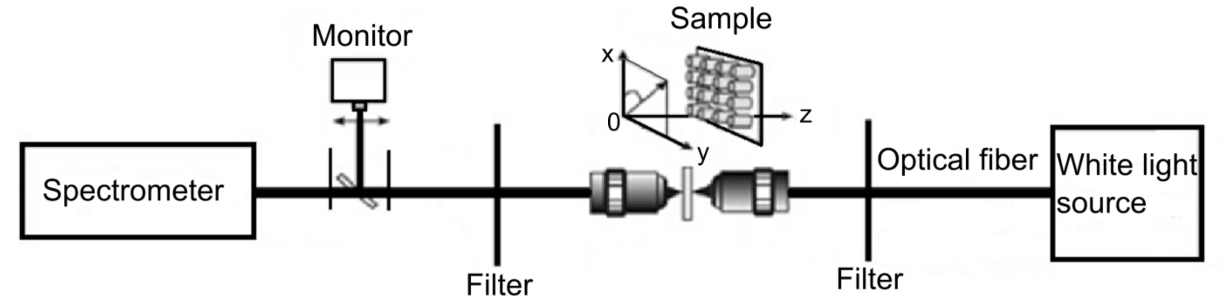

Figure 3.6 Illustration of a home-built extinction microscope.

For the NP assembly, as shown in Fig. 3.6, a home-built confocal extinction microscopeis used to record the extinction spectra from different zones of sample in the UV−vis−NIR range (300 nm to 1100 nm). The optical setup contains a white light source, two optical fibers (one for illumination and the other for collection), two band-pass(300 nm-900nm) filters, two objective lens (20x) and an adjustable sample holder.[77] It should be noted that due to the optical fibbers and lens combinations used in the confocal setup, the incident beam is focused perpendicularly onto the patterned glass during all the measurements giving a spatial resolution of 10 μm. Fig. 3.7 shows one example of extinction spectra of Au nano disc array. The Au disc was fabricated on glass, and the diameter varies from 100 nm to 150 nm as a step of about 10 nm. The edge-to-edge distance between each NP is 330 nm.

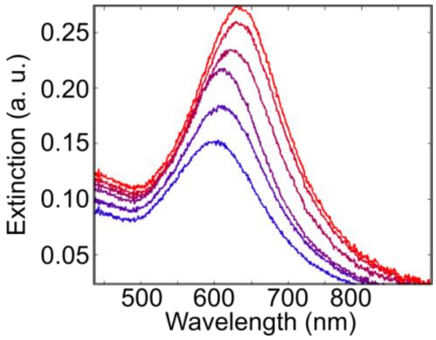

Figure 3.7 Extinction spectra of Au nano disc array on glass with diameters from 100 nm to 150 nm.

3.3 Characterization of nonlinear optical responses

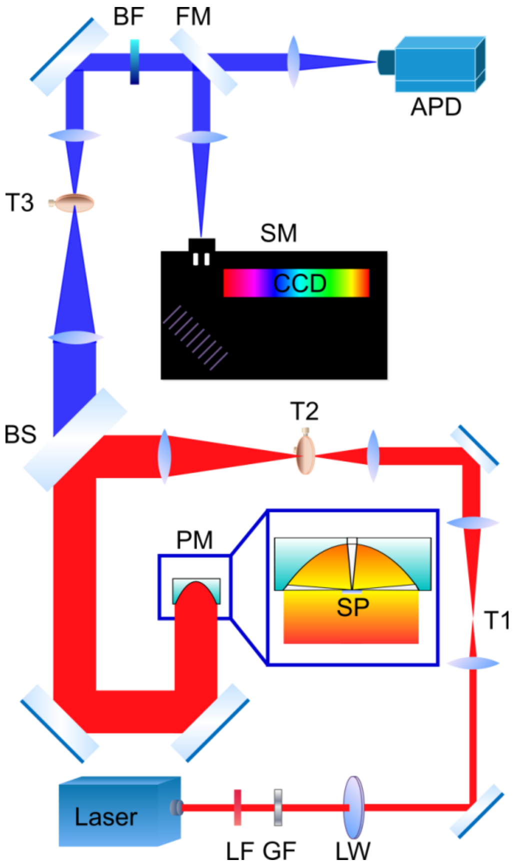

Figure 3.8 Sketch of the nonlinear optical set-up based on a parabolic mirror. Laser: 774 nm (110 fs, 89 MHZ); LF: line filter; GF: gray filter; LW: Lambda half wave plate; T1,2,3: telescopes; BS: beam splitter; PM: parabolic mirror; SP: sample; BF: band pass filter; FM: flipping mirror; APD: avalanche photo-diode; CCD: charge-coupled device; SM: spectrometer. [24]

The nonlinear optical responses of the plasmonic nanostructures are collected using a home-built confocal scanning optical microscope, as shown in Fig. 3.8. A femtosecond (fs) laser generates ultra-short pulses (~110 fs, 89 MHz, 774 nm) and is employed to excite the sample.[24] After a laser line filter and a gray filter, the beam passes through a lambda-half wave plate, to be able to turn the linear polarization freely by 360°. Afterwards the beam was expanded by two telescopes. By using a pinhole within the second telescope, undesired polarization and scattered light are filtered out to obtain a homogeneous Gaussian mode. The linearly polarized light is reflected by a non-polarizing dichroic beam splitter towards the parabolic mirror. The parabolic mirror serves both as the focusing element and the signal collector. In air its NA reaches 0.998.[78] Such a high-NA and low-chromatic-aberration mirror enables a high resolution down to the diffraction limit. The emitted optical signal of the NPs was collected and sent through the beam splitter. The dichroic beam splitter (transmitting light range: 360 nm~ 700 nm) excludes the light at the fundamental and longer wavelengths and only transmits the nonlinear information. After reducing the beam size with a third telescope, scattered light is excluded by a pin-hole, and the detection wavelength range was selected by a band-pass filter. With a flipping mirror, the beam was either directed towards the spectrometer (Princeton Instruments) to obtain spectral information or to an APD (Single Photon Counting Module - COUNT® BLUE) for point-by-point optical imaging.

3.4 Elastic scattering simulation

Elastic scattering can be normally simulated by FDTD. It is a state-of-the-art method for solving Maxwell's equations in complex geometries. Being a direct time and space solution, it offers a unique insight into most types of problems in electromagnetics and photonics. In general cases, such as monomers, homodimers and the heterodimers with gaps, FDTD can supply quite proper results. This method will be introduced in Chapter 4 to treat most of simple cases. However, in order to simulate the dark-field scattering in accordance with our experimental conditions, a volumic Green's tensor method was used to refine the simulation.[79] In the model system, the dimer is located on a substrate of refractive index n=1.5, excited by several polarized plane waves coming from the air side of the interface. The angle of incidence is θ = 63°, corresponding to the average angle of incidence through the dark-field condenser in the experiment. In order to take into account the finite numerical aperture for the collection of light, the scattering spectra are computed by integrating the asymptotic Poynting vector in a cone of 20° around the normal to the interface in the glass (see Fig. 3.9). The contributions of two plane waves are incoherently summed for each polarization: in direction (1), the plane wave is incident at $\theta = 63°$, the incidence plane being parallel to the dimer long axis, in direction (2), the plane wave is incident at $\theta = 63°$, the incidence plane being perpendicular to the dimer long axis. Hence, for longitudinal illumination, the in-plane component of the *p*-polarization of direction (1) is summed with the *s*-polarization of direction (2). The same procedure is also performed for the transversal illumination, where the s-polarization of direction (1) is summed with the in-plane component of the p-polarization of the direction (2).[24] This method will be employed to treat more complex cases, such as the contacted dimers, which will be discussed in Chapter 5.

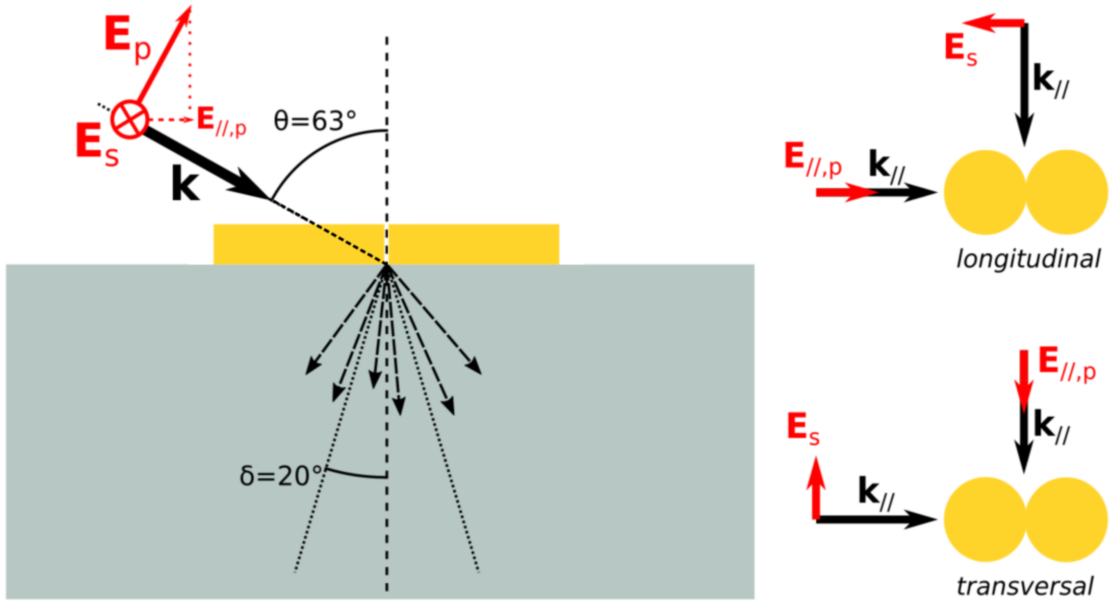

Figure 3.9 The illumination and signal collection schemes of the dark-field optical microscope, the polarizations as well as the dimer geometries considered in the numerical calculations. The illumination angle is 63° and the collection angle is 20°.[24]

3.5 Nonlinear optical signals simulation

SHG and MPL especially TPL are our main investigating targets in terms of nonlinear optical responses. To disclose the physical origin of the TPL and SHG responses and explain the results of the experiments, numerical simulations were performed with an in-house SIE code giving accurate results for both the near- and the far-field distributions, even in resonant conditions.[80] Two distinct numerical schemes are used for the computation of the SHG and TPL responses. Let us first describe the SIE method for surface SHG. It is well known that SHG is forbidden in the bulk of centro-symmetric media within the dipolar approximation.[81, 82] Nevertheless, this symmetry is broken at the interface between two centro-symmetric media, and SHG arises from metallic nanostructure surfaces.[83, 84] SIE methods only require the discretization of the surfaces of the metal NPs, exactly where the SHG sources are located, and are therefore extremely well suited for an accurate surface SHG computation.[81, 82] Here Only the component of the surface tensor $\chi_{surf,\perp\perp\perp}$ is considered, where $\perp$ denotes the component normal to the surface, which is known to dominate the surface response for metallic NPs.[83, 84]The nonlinear polarization can be written as $P_{surf,\perp\perp\perp}(r,2\omega) = \chi_{surf,\perp\perp\perp}E_n(r,\omega)E_n(r,\omega)$, as discussed in "Theoretical background" section. The SH surface currents are obtained solving the SIE formulation taking into account the nonlinear polarization and enforcing the boundary conditions at the nanostructure surfaces. As the linear surface currents, the SH surface currents are expanded on Rao-Wilton-Glisson basis functions. The expansion coefficients are found applying the method of moments with Galerkin testing. A Poggio-Miller-Chang-Harrington-Wu formulation is used to ensure accurate solutions even at resonant conditions.[80] The SH electric field is then deduced from the SH surface currents using a two-term subtraction method for the evaluation of the Green functions.[25, 30] To compare the numerical results with the experimental observations, the SH intensity is integrated over a hemisphere reproducing the light collection performed by the parabolic mirror.

The approach used for the evaluation of the TPL signal is fundamentally different owing to its distinct physical origin. Contrary to SHG, which is a coherent surface process, TPL is a process involving the excitation of an electron-hole (e-h) pair by the absorption of two incident photons, the relaxation of the excited electron and hole, and the emission of light due to the recombination of the electron with the hole.[24, 51] The numerical calculation of TPL induced by direct e-h pair recombinationcan refer from G. T. Boyd in the theory part (section 2.4.2). LSPR also plays of importance role in both excitation and radiation processes of TPL, the influence of which will be discuss in chapter 6.

Chapter 4 Elastic scattering of Au and Al nanoantennas

The elastic scattering properties reflect the LSPRs of specific nanoantennas, which is the first step to interpret the optical enhancement observed in surface enhanced spectroscopy and microscopy. In this section, the dark-field scattering spectra① of Au and Al nanoantennas will be presented and discussed. The investigated systems② include Au and Al monomers, Au-Au and Al-Al homodimers, and Au-Al heterodimers. For each system, its size and gap (for the homodimers) dependences are studied in different excitation polarizations. The general evolution of LSPRs for each system is our target, rather than discussing every plasmon modes for each nanostructure into detail. The description of dark-field scattering microscope can be found in "Materials and methods" section. FDTD is employed to calculate the elastic scattering spectra and charge distributions, in order to interpret the surface plasmon mode. For simplification, a plane wave propagating along the Z direction will represent the illumination scheme of the actual dark-field scattering microscope. The more accurate models will be introduced in Chapter 5 to treat specific problems.

---

① The experimental dark-field scattering spectra in this chapter are measured by Dr. Anne-Laure Baudrion in University of Technology of Troyes and Andreas Horrer and Prof. Dr. Monika Fleischer in University of Tuebingen.

② The sample investigated in this chapter is fabricated by Dr. Anne-Laure Baudrion in University of Technology of Troyes.

4.1 Au monomer and Au-Au dimer

4.1.1 Au monomers

Dark-field scattering spectra of Au monomers with diameters of 80 nm, 100 nm, 120 nm, 140 nm, 160 nm and 200 nm are measured in longitudinal polarization (LP) and transverse polarization (TP), as shown in Fig. 4.1(a). The peak position shifts from around 580 nm to 800 nm as the size increases. The intensity shows a gradual increase as the NP volume rises. The slight spectral difference in central wavelength between LP and TP may be due to the inhomogeneity of NPs. Corresponding FDTD simulations of Au monomers with diameter ranging from 80 nm to 200 nm as a step of 20 nm are shown in Fig. 4.1(b). The simulation agrees with the experimental result, except there is a slight red shift of the peak position.

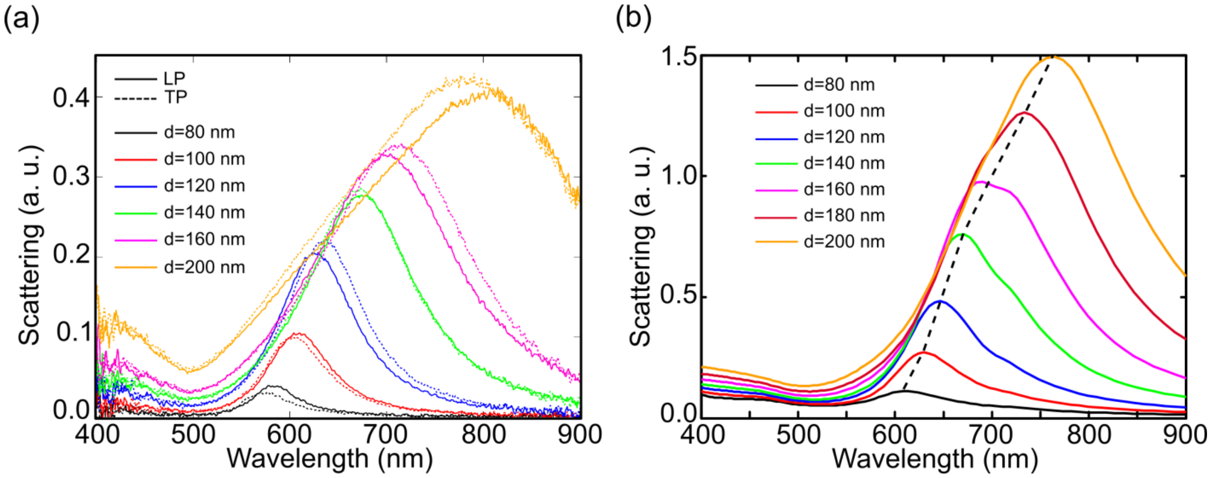

Figure 4.1 (a) Experimental dark-field scattering spectra of Au monomers with diameters of 80 nm, 100 nm, 120 nm, 140 nm, 160 nm and 200 nm in LP and TP. (b) Corresponding FDTD simulations of Au monomers with diameter ranging from 80 nm to 200 nm with a step of 20 nm.

4.1.2 Au-Au dimers

The dimer is the simplest coupled system. Similarly, horizontal dimers are fabricated, in order to investigate their LSPRs and the coupling effect in the gap region. The polarisability of a coupling system can be explained phenomenologically by mechanical vibrations, as described in “Theoretical background” section 2.6. The size and gap dependences for Au dimers are investigated separately.

(a) Size dependence

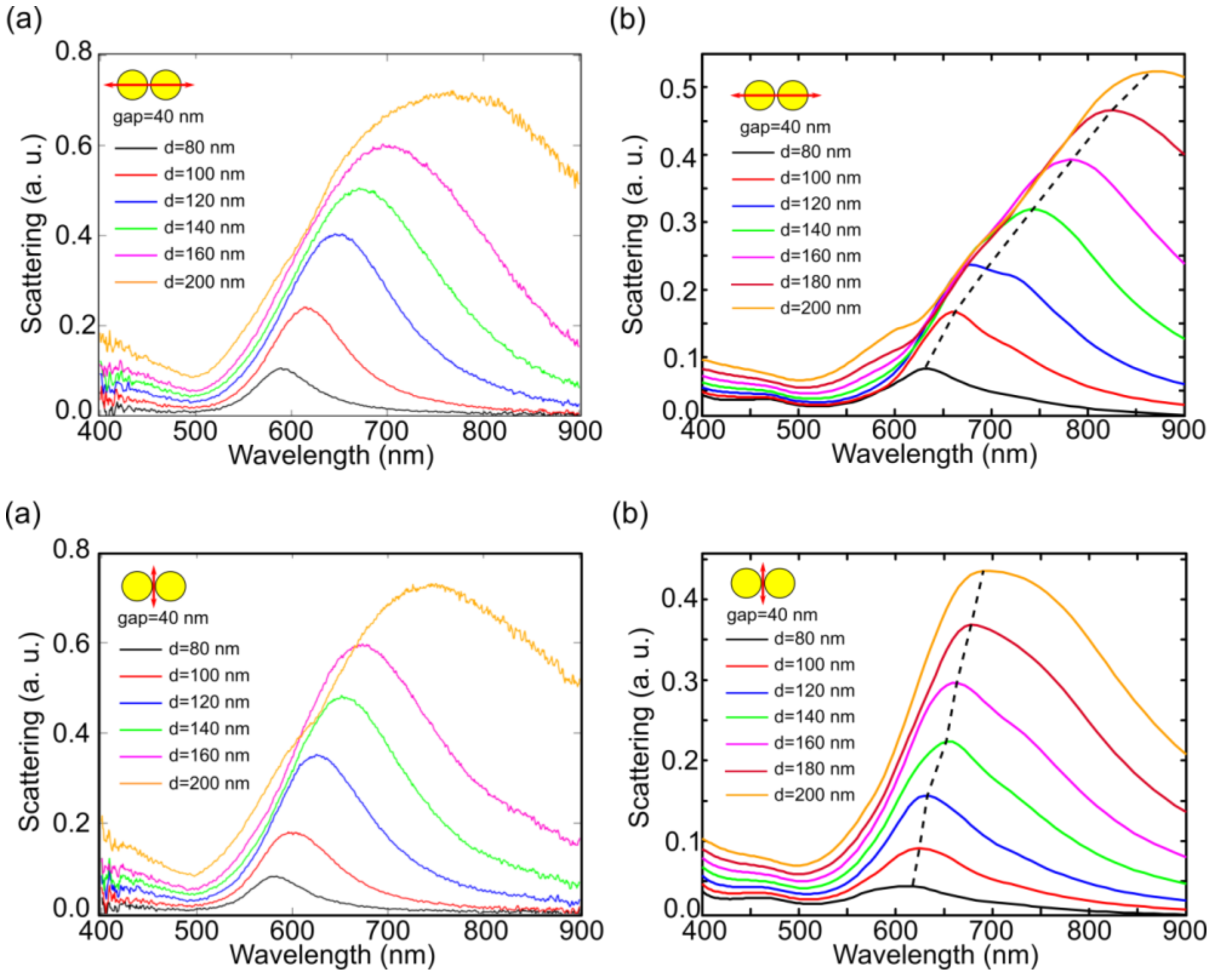

Figure 4.2 Experimental dark-field scattering spectra of Au dimers with a 40 nm gap and diameters of 80 nm, 100 nm, 120 nm, 140 nm, 160 nm and 200 nm underLP (a) and TP (c).Their corresponding FDTD simulations of Au dimers with a gap of 40 nm and diameter ranging from 80 nm to 200 nm with a step of 20 nm are shown in (b) and (d). The plasmon modes are indicated as black dashed lines.

As shown in Fig. 4.2, experimental dark-field scattering spectra of Au dimers with a gap of 40 nm and diameters of 80 nm, 100 nm, 120 nm, 140 nm, 160 nm and 200 nm in LP and TP are show in (a) and (c). Their corresponding FDTD simulations of Au dimers with diameter ranging from 80 nm to 200 nm as a step of 20 nm are shown in (b) and (d). When the excitation polarization is along the dimer long axis, the peak is red-shifted and has a broader full-width at half maximum (FWHM), comparing with the corresponding monomer system. This becomes more obvious in the simulated results, as seen in Fig. 4.2(b). The LSPRs of longitudinal dipole mode shift the peak positions from 620 nm to 850 nm. The reason can be phenomenologically explained by the decreasing restore force and the retardation of the coupling system.[1]

However, such red-shifts are not so apparent, comparing to the corresponding monomers, when the dimers are transversally excited, as shown in Fig. 4.2(c) and (d). The peak position of transverse dipole mode (black dashed line in (d)) shifts from around 600 nm to 700 nm with the increase of disc diameter. This can be explained by the fact that the transverse dipoles are less coupled, comparing with the case in longitudinal excitation..

(b) Gap dependence

The influences of gap dependences of Au dimers on the scattering spectra are studied as well. Experimental dark-field scattering spectra of Au dimmers in LP and TP (c) are shown in Fig. 4.3(a) and (c).The dimer has the diameter of 100 nm and the gap of 0, 20 nm, 40 nm, 60 nm, 100 nm and 250 nm. Their corresponding FDTD simulations of Au dimers with the gap ranging from 0 to 60 nm as a step of 20 nm are shown in Fig. 4.3(b) and (d), respectively. The plasmon modes are indicated as black dashed lines. The contacted dimers are apparently different from the gapped dimers when the excitation polarization is along the dimer long axis. Two plasmon modes can be observed from the contacted dimer in the detectable spectral window: one situates at around 600 nm, and another situates above 900 nm.

However, only the first mode can be detected from the gapped dimers. The first plasmon mode corresponds to the quadruple mode, and the second the longitudinal dipole mode. More in details will be discussed in Chapter 5. For the dimers with gaps, it is clear to see that when the excitation polarization is along the dimer long axis, the peak position generally has a blue shift as the gap increases and is closing to the corresponding monomers. It is easily understandable that a dimer with infinitive large gap should have the same behaviour as the corresponding monomer. In transverse excitation, however, the scattering spectra nearly keep the same, which means that the gap doesn’t influence the LSPRs as much as that from the longitudinal excitation.

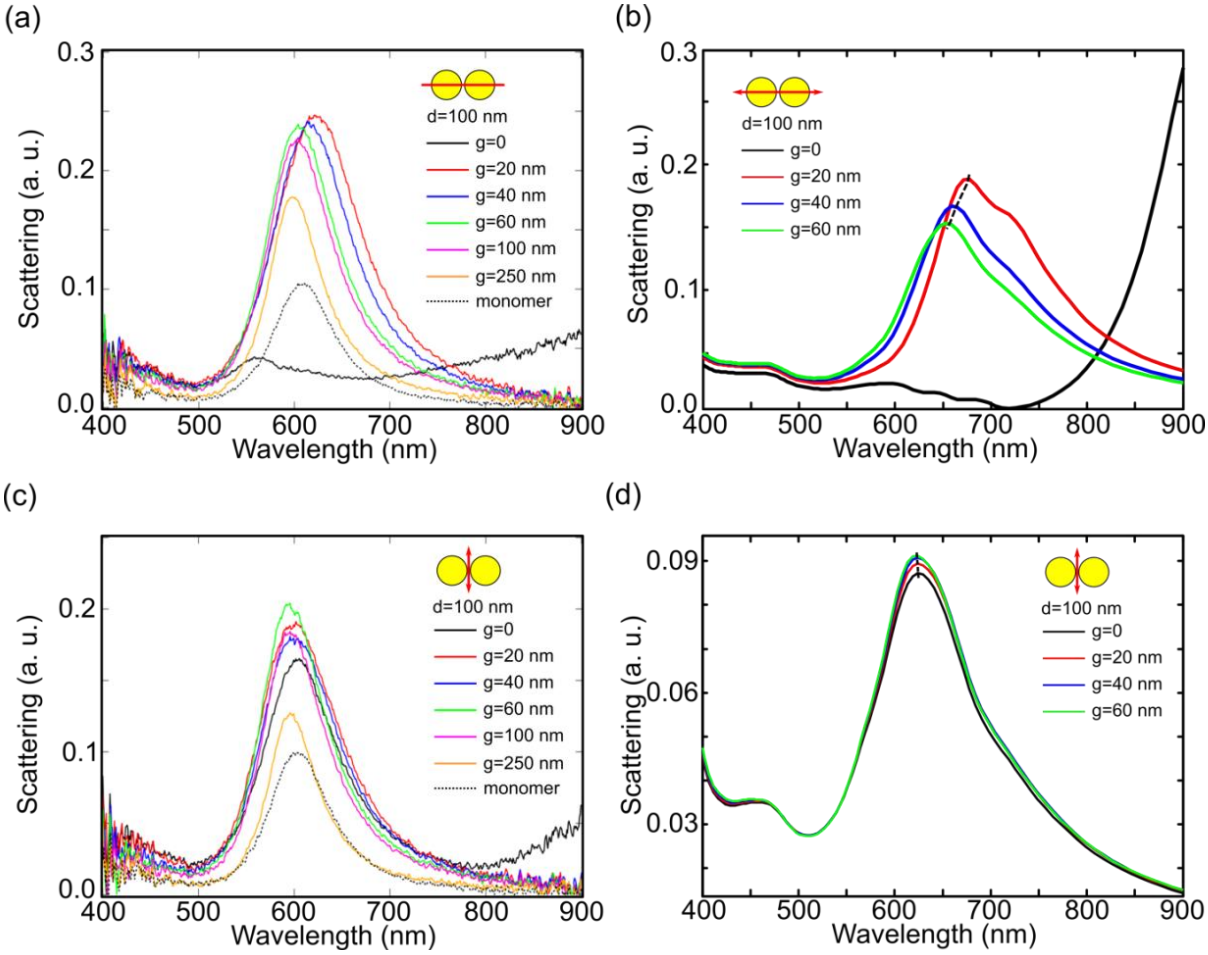

Figure 4.3 Experimental dark-field scattering spectra of Au dimers with the diameter of 100 nm and the gaps of 0, 20 nm, 40 nm, 60 nm, 100 nm and 250 nm in LP (a) and TP (c). Their corresponding FDTD simulations of Au dimers with the gap ranging from 0 to 60 nm as a step of 20 nm are shown in (b) and (d), respectively. The plasmon modes are indicated as black dashed lines.

4.2 Al monomer and Al-Al dimer

4.2.1 Al monomers

Due to the interband transition, LSPR of Au NPs is not able to be tuned lower than 550 nm wavelength. However, it is not the case for Al NPs. The LSPRs of Al NPs can be easily tuned from ultraviolet to the visible region, which generates lots of applications such as LSPR enhanced SHG, double-resonance plasmonic nanostructures and so on.[85-87] Indeed, experimental dark-field scattering spectra of Al monomers with diameters varying from 120 nm to 220 nm as a step of 20 nm in LP and TP are shown in Fig. 4.4(a).Fig. 4.4(b) shows corresponding FDTD simulations. The positions of the simulated plasmon modes are indicated as black dashed lines.

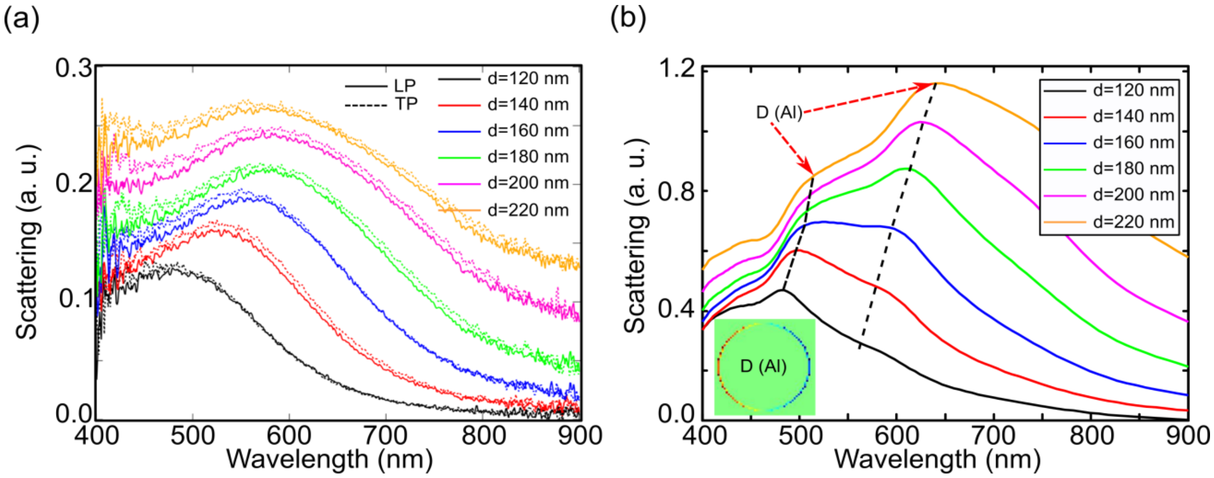

Figure 4.4 (a) Experimental dark-field scattering spectra of Al monomers with diameters varying from 120 nm to 220 nm as a step of 20 nm in LP and TP. (b) The corresponding simulated spectra using FDTD. The plasmon modes are indicated as black dashed lines. The charge distributions excited at resonant frequencies are similar, which implies the dipole mode (D(Al)) and is shown in the inset of (b).

Being different from the experimental results, where there is only one broad peak for each spectrum, two “splitted” peaks are found from each spectrum. The first peak shifts the peak position from 480 nm to 520 nm with the increase of disc diameter. The peak position of the second peak shifts from 550 nm to 640 nm. However, they have the same charge distributions. As an example, the nanodisc with the diameter of 220 nm is excited at resonant wavelengths: 520 nm and 640 nm respectively. The charge distributions show almost no difference, which all implies the Al dipole mode, abbreviated as D(Al), as can be seen in Fig. 4.4(b) inset. This indicates that the two “splitted” peaks might be induced by the same plasmon mode.

Furthermore, similar as Au NPs, the peak position of experimental LSPRs shifts from 480 nm to 620 nm as the diameter increases. Notably, the minimum and maximum peak positions almost correspond to the minimum position of the first peak and the maximum position of the second peak in simulation as the size of NP increases. Thus, the experimental scattering peaks could be the envelope line of two splitting peaks in the simulation.

4.2.2 Al-Al dimers

The general tendencies of the size dependent and gap dependent scattering spectra for Al-Al dimers are similar to Au-Au dimers. However, the red-shifts as NP size increases when the polarization is along the dimer long axis are not as obvious as Au NPs. Furthermore, the two “splitted” peaks which appear in the Al monomers behave differently when the polarization is along the dimer long axis. Hereafter, the size dependence and the gap dependence of Al homodimer will be investigated separately.

(a) Size dependence

Experimental dark-field scattering spectra of Al-Al dimers with a 40 nm gap and diameters from 120 nm to 220 nm as a step of 20 nm in LP and TP are shown in Fig. 4.5(a). The peaks have similar peak positions in two polarizations, but FWHMs in TP are almost 30 nm larger than the ones in LP. For the largest dimers, new peaks appear in the wavelength shorter than 500 nm. Fig. 4.5(b) and (c) shows the corresponding simulations in LP and TP, respectively. Similar as Al monomers, there are two “splitted” peaks for each dimension of Al-Al dimer. In LP, the first one situates at around 500 nm, which keeps almost static as size changes. The second one situates 600 nm for the smallest dimer, and shifts to 650 nm as NP size increases. In TP, the peak position of the first peak shifts from 480 nm to 520 nm, and the second from 600 nm to 620 nm.

Further analysis is made in an Al homodimer with the diameter of 120 nm. When the dimer is excited at the resonant frequencies (500 nm and 600 nm in LP, and 480 nm and 600 nm in TP), the two “splitted” modes appear the same charge distributions. Thus, the two “splitted” spectral peaks might derive from the same plasmon mode. In LP, the plasmon mode is represented as D(Al) + D’(Al), where the ‘prime’ symbol indicates the reversed dipole momentum, and “+” represents the “coupling” mechanism. The plasmon mode is also called dipolar bonding mode. The charge distribution can be seen in the inset of Fig. 4.5(b). Similarly, the plasmon mode of D(Al) + D(Al) can be observed in TP, as shown the charge distribution in Fig. 4.5(c) as inset.

Similar phenomenon can be found that the overall shifting range of two "splitted" peaks in the simulation corresponds to the shifting range of the predominant peak in the experiment. This further supports the deduction: the two "splitted" peaks imply the same plasmon mode, and enveloped as one broad peak in experimental spectra.

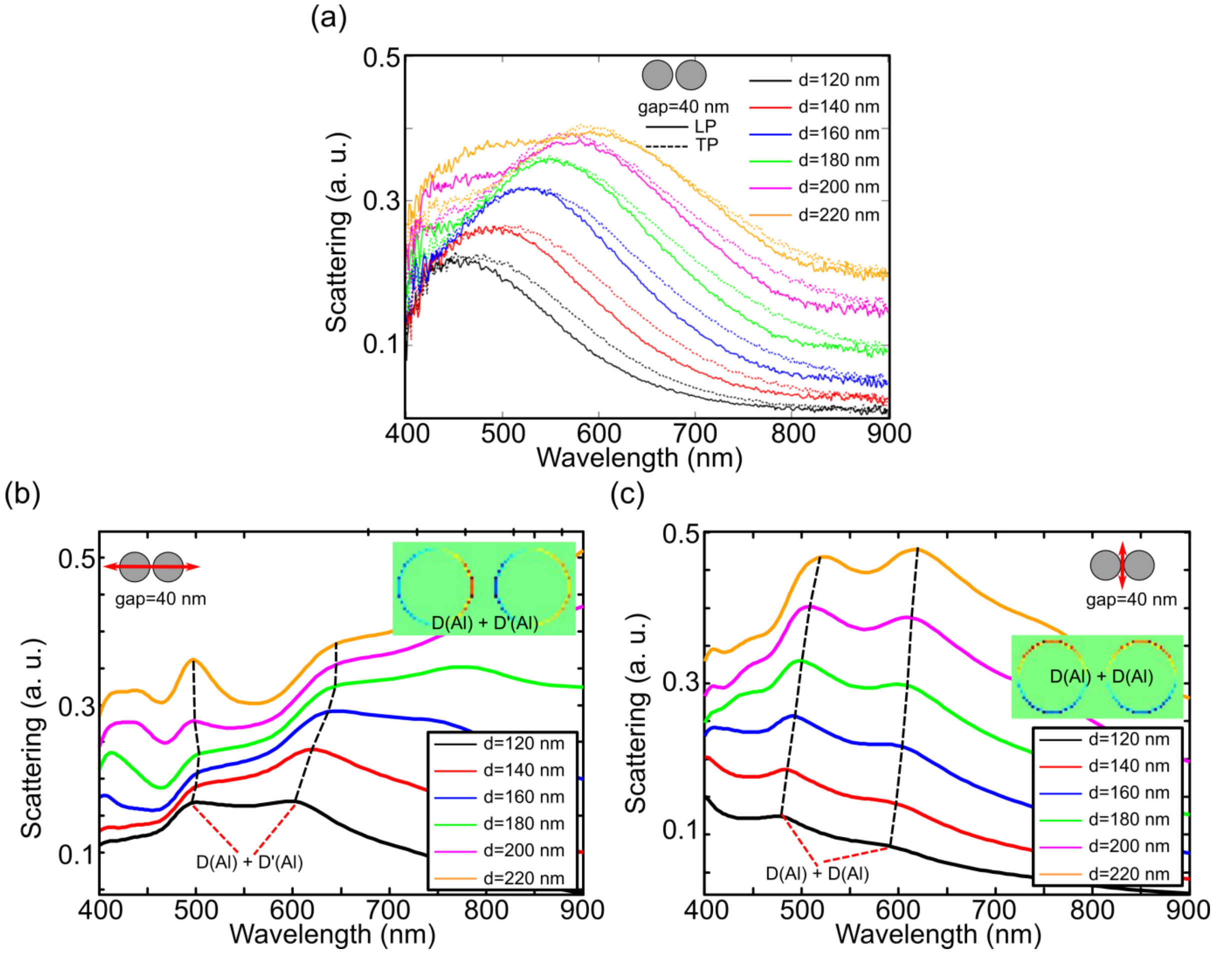

Figure 4.5 (a) Experimental dark-field scattering spectra of Al dimers with a 40 nm gap and varying diameters from 120 nm to 220 nm as a step of 20 nm in LP and TP. Their corresponding simulations using FDTD are shown in (b) and (c), respectively. The plasmon modes are indicated as black dashed lines. Charge distributions of a Al homodimer with diameter of 120 nm that is excited at resonant frequencies in LP and TP are shown in the inset of (b) and (c), respectively.

(b) Gap dependence

Experimental dark-field scattering spectra of Al dimers with the diameter of 120 nm and the gaps of 0, 20 nm, 40 nm, 60 nm, 100 nm and 250 nm excited in LP and TP are shown in Fig.

4.6(a) and (c). Their corresponding FDTD simulations of Al dimers with the gap ranging from 0 to 60 nm as a step of 20 nm are shown in (b) and (d), respectively.

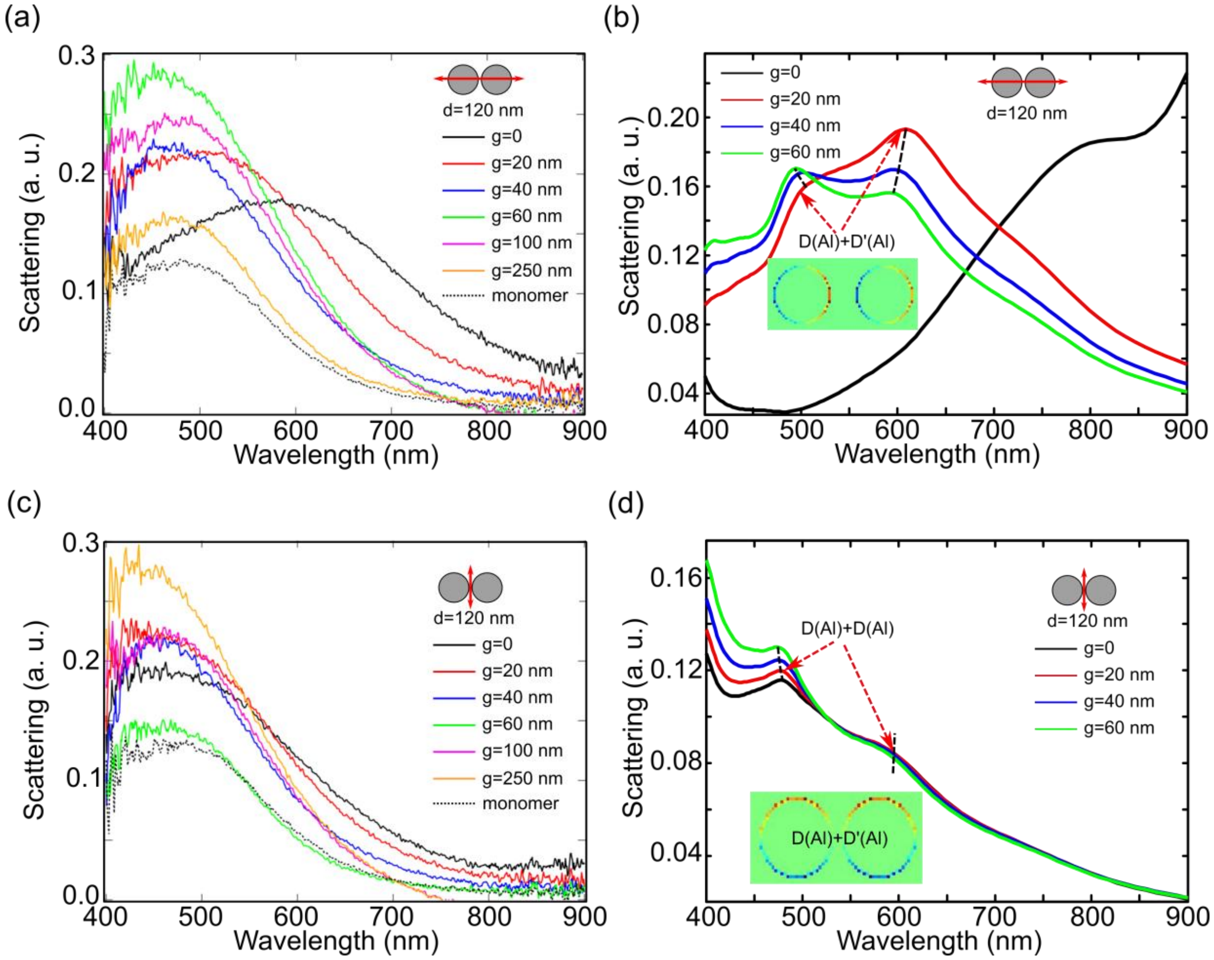

Figure 4.6 Experimental dark-field scattering spectra of Al dimers with the diameter of 120 nm and gaps of 0, 20 nm, 40 nm, 60 nm, 100 nm and 250 nm respectively in LP (a) and TP (c). Their corresponding FDTD simulations of Al dimers with the gap ranging from 0 to 60 nm as a step of 20 nm are shown in (b) and (d), respectively. The plasmon modes are indicated as black dashed lines, and the charge distributions of an Al homodimer with a gap size of 20 nm excited at resonant frequencies are shown in insets.

In LP, the contacted dimer shows apparent difference from the gapped dimers, which has a broad peak at a much longer wavelength (600 nm in experiment and 800 nm in simulation). The experimental peak position of gapped dimer shows a slight blue shift as the gap size increases. In the simulation, the two splitted peaks change with similar trend as the increase of gap size. The first peak starts from 500 nm and gradually shifts to 480 nm as the gap size increases. The second peak has a blue shift which starts from 610 nm to 580 nm. The overall shifting range defined by the minimum of the first peak and the maximum of the second peak in simulation corresponds to the shifting range of the predominant peak in experiment. The similar charge distributions ,as shown in the inset of Fig. 4.6(b), indicate two splitted peaks might derive from the same plasmon mode, represented as D(Al) + D'(Al), when a Al homodimer with a gap of 20 nm is excited at resonant frequencies.

In TP, a slight blue shift (from 500 nm to 450 nm) could be observed from the experimental results. In the simulation, the second splitting peak situating at 600 nm nearly disappears. The first splitted peak is predominant and has a slight of blue shift (from 470 nm to 460 nm). The similar charge distributions ,as shown in the inset of Fig. 4.6(d), offer further evidence that two splitted peaks might derive from the same plasmon mode, represented as D(Al) + D(Al), when a Al homodimer with a gap of 20 nm is excited at resonant frequencies.

4.3 Au-Al dimer

The coupling effects become more complicate when two kinds of materials of NPs are combined together, left alone taking the interband transitions into account during the excitation of LSPRs. Here an example of Au-Al heterodimers with Au NP diameter of 160 nm and Al NP diameter varying from 120 nm to 220 nm is shown. The edge-to-edge gap size is 40 nm. Fig.4.7 shows experimental dark-field scattering spectra in LP (a) and TP (c). Their corresponding simulations using FDTD of Au-Al dimers with Al diameter ranging from 80 nm to 200 nm as a step of 20 nm are shown in (b) and (d), respectively. The plasmon modes are indicated as black dashed lines. The charge distributions of a Au-Al heterodimer with Al NP diameter of 120 nm excited at resonant frequencies are shown in insets.

When the excitation polarization is along the long dimer axis, two peaks can be observed from the experimental scattering spectra, shown in Fig. 4.7(a). The first one is the broad one, which situates at around 800 nm and doesn't shift so much as the size of Al NP increases. The second one situates between 500 nm and 600 nm, and has a red-shift as the size of Al NP increases. The corresponding simulation is shown in Fig. 4.7(b). From the charge distribution, it is clear to see that the broad peak in the scattering spectrum indicates the Au dipole-Al dipole plasmon mode. For a simplification, this mode is written as D'(Au) + D(Al) mode.

This plasmon mode situates at around 650 nm, but has a slight red shift as the diameter of Al NP increases. This can be understood that the D'(Au) + D(Al) mode is mainly contributed to Au dipole mode, and the Al dipole mode is responsible to the slight red shift of the peak position, due to the increase of Al NP diameter.

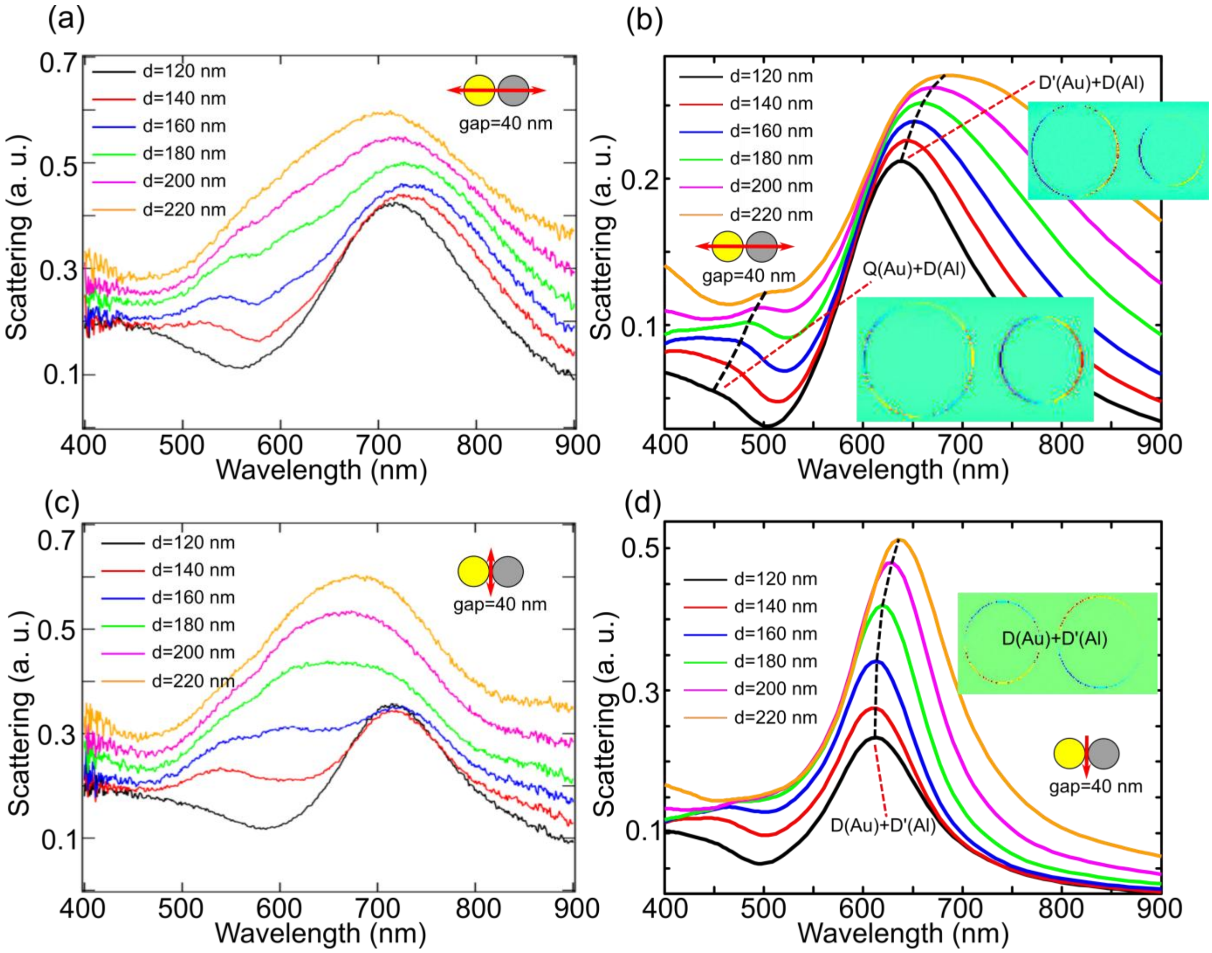

Figure 4.7 Experimental dark-field scattering spectra of Au-Al dimers with a 40 nm gap. The diameter of Au disc is 160 nm, and that of the Al disc diameter varies from 120 nm, 140 nm, 160 nm, 200 nm and 220 nm in LP (a) and TP (c). Their corresponding simulations using FDTD are shown in (b) and (d), respectively. The plasmon modes are indicated as black dashed lines. The charge distributions of a Au-Al heterodimer with Al NP size of 120 nm excited at resonant frequencies in LP and TP are shown in insets of (b) and (d), respectively.

The second peak in the higher energy range is rather complicate, as quadruple-dipole coupling is involved, as can be seen from the charge distribution in Fig. 4.7(b). The plasmon mode of Q(Au) + D(Al) can be observed from the charge distribution. What's more, as the size of Al NP increases, different coupling schemes between Au NP and Al NP appear.

However, such change of coupling schemes follows the same rule. If the diameter of Au NP and the gap size are fixed, as the diameter of Al NP increases, the plasmon modes will behave as: Q(Au) + D(Al) -> D(Au) + D(Al) -> D(Au) + Q(Al). The varying trend of charge distribution is shown as Fig. 4.8. More complicate plasmon mode can be found from the higher energy regime, but it will be out of our scope.

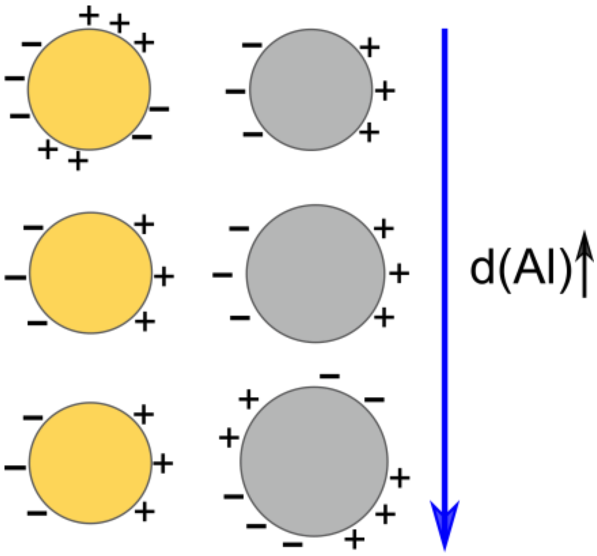

Figure 4.8 The changing trend of charge distribution for the Au-Al heterodimers, where the diameter of Au NP and the gap size are fixed, and the diameter of Al NP increases.

When the excitation polarization is along the short dimer axis, one broad peak can be observed from the experimental scattering spectra, as shown in Fig. 4.7(c). The peak position situates at around 650 nm, and doesn't shift so much as the size of Al NP increases. The corresponding simulation is shown in Fig. 4.7(d). From the charge distribution, it can be seen that this peak represents the D(Au) + D'(Al) mode. The increase size of Al NP is responsible for the slight red shift of the peak position.

4.4 Summary

The elastic scattering for different plasmonic systems is investigated, from the aspects of experiment and simulations. The studying systems include Au and Al monomers, Au-Au and Al-Al homodimers, and Au-Al heterodimers. For each system, their size and gap (for the homodimers) dependences are studied in different excitation polarizations. Corresponding simulations are conducted by means of FDTD. Different coupling schemes of plasmon modes from two NPs are involved in Au-Al heterodimers. The Au-Al heterodimers with fixed gap size and Au NP size are taken for examples to study the different plasmon modes in transverse and longitudinal excitation polarizations. Revealing the general rules is our main target, which paves the roads for the following chapters.

Chapter 5 Far-field SHG radiation from various types of nanoantennas

Plasmonic nanoantennas can be used for the excitation of nonlinear optical processes since the field intensity at the fundamental wavelength is increased in their vicinities thanks to LSPRs. Since the conversion yield of nonlinear optical processes varies nonlinearly with the fundamental intensity, it might be expected to increase with the fourth or a higher power with the local field factor *L(ω)* evaluated at the fundamental frequency. For this reason, it was proposed to use nonlinear optical processes to evaluate the field enhancement in electromagnetic hotspots, *e.g.* nano-gaps, taking advantage of this nonlinear dependence.[24, 34,88] However, such a description of nonlinear optical processes in plasmonic nanoantennas is somewhat limited. For example due to the specific selection rules the SHG from tiny centro-symmetric nano-gaps is weak, despite a strong fundamental field enhancement.[89-91] As a consequence, the relations between the field enhancement and the conversion yields of the various nonlinear optical processes need to be carefully determined and evaluated, before they can be safely used for characterizing the magnitude of the electric field in hot-spots.[24]

Starting from the observation of SHG from plasmonic nanoantennas of varying sizes, the influences of the local near-field intensity distribution on the excitation and emission processes of SHG① is discussed, by varying the plasmon resonances of the nanostructures and the polarization of the incident beam, on a model system consisting of connected spherical dimers. The SH phase interference plays of importance role during radiation from the near-

---

① Theoretical calculations of SHG are contributed by Dr.Jérémy Butet, and Prof. Olivier J. F. Martin in Swiss Federal Institute of Technology, Lausanne (EPFL), Switzerland. The sample of Au-Au homodimers in this section is prepared by Dr. Anne-Laure Baudrion in University of Technology of Troyes.

field to far-field. Both resonant excitation and phase interference should keep in mind when try to interpret the SHG near-field intensity from the far-field detection.

5.1 Flipping effect of far-field SHG radiation

Arrays of connected nanodimers composed of discs with different diameters (d = 80 nm, 100 nm, 150 nm, and 175 nm) are fabricated using EBL. Corresponding gold monomers (d increases from 80 nm to200 nm) are also fabricated to serve as references. The spacing between the individual nanostructures is 10 µm so that the dark-field scattering measurements and the nonlinear optical measurements can be performed at a single particle level with confocal microscopy. The structure height is 50 nm. Detailed description of the fabrication procedure as well as the setups used for the linear and nonlinear optical measurements can be found in the 'Materials and methods' section.

Polarization dependent measurements are performed by rotating the incident beam (TEM00 mode) using a half-wave plate that is positioned in the excitation path. As an example, the spectra recorded for an incident wave polarized along the long axis of a single dimer are shown in Fig. 5.1(a). A weak and narrow peak located at 387 nm can be seen, which corresponds to SHG, and the width of which is related to the bandwidth of the femtosecond laser pulses. The second observed feature is an intense and broad peak, with a maximum at longer wavelengths than the SH peak and moving to lower energies as the diameter of the connected nanodisc increases. This nonlinear emission corresponds to the TPL signal that shows a second order power dependence.

In order to quantify the influence of the incident polarization on the SHG signals, the emission intensities from 380 nm to 390 nm (after subtraction of the PL background) are integrated. The incident polarization was rotated with a step of 20°. Polarization-dependent intensities of SHG from connected dimers with different sizes are shown in Figs. 5.1(b). As clearly can be seen, the maxima of the SHG polarization-dependence plots vary with the particle size. For the smallest dimers, i. e. d = 80 nm and 100 nm, the maxima of the SHG polarization-dependence plots are reached in longitudinal excitation, as observed in the case of TPL. On the other hand, for the largest dimers, i. e. d = 150 and d = 175 nm, the maxima flip by about 90 degrees, and SHG is maximized when the incident wave is polarized along the short dimer axis or transverse excitation. This clearly points out that it is not always straightforward to derive the orientation of a nanodimer only from its incident field polarization-dependent far-field SHG intensity.

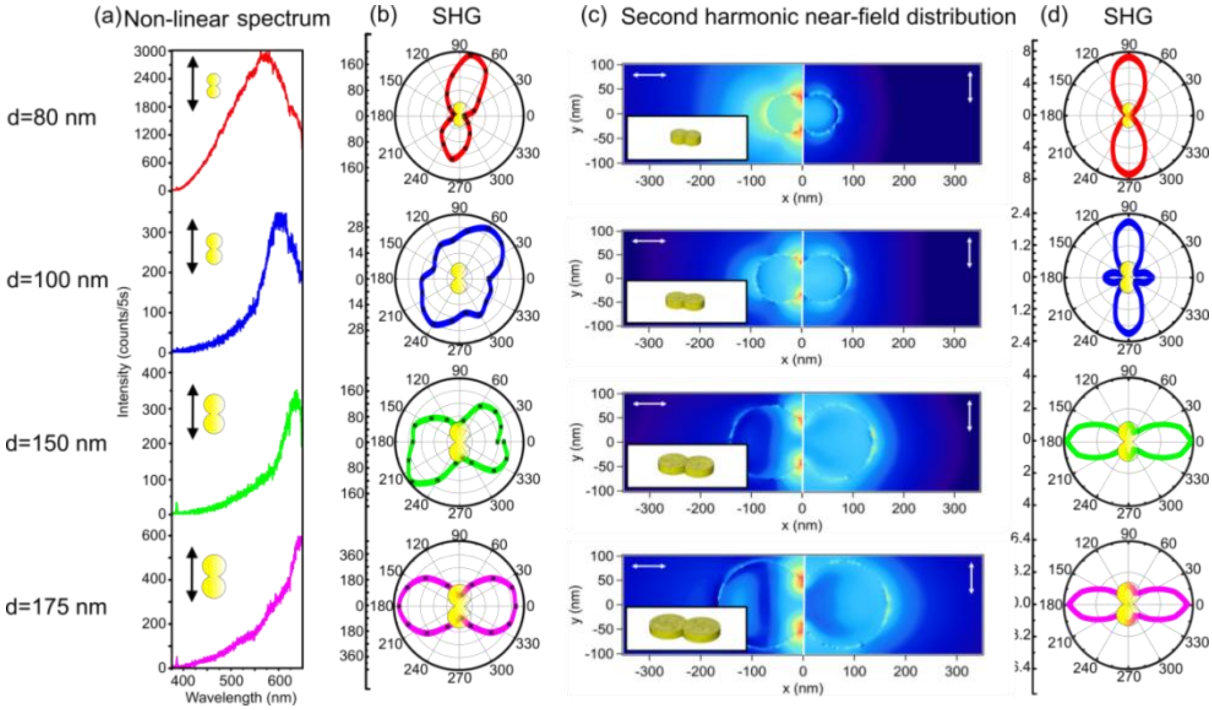

Figure 5.1 (a) Emission spectra, (b) experimental SHG intensity, (c) SH near-field intensity and (d) calculated SHG intensity as a function of the different excitation polarizations for single connected gold nanodimers with NP diameters d = 80 nm, 100 nm, 150 nm, and 175 nm, respectively. In panel (a), the nonlinear spectra were recorded for an incident polarization along the long dimer axis, as represented by the black arrows in the insets. In panel (c), the polarization direction is shown as a white arrow. For simplicity, the field distribution around only half of the nanodimer is shown in each panel. In panels (b) and (d), the starting polarization angle (0°) is perpendicular to the long dimer axis. (c) and (d) is calculated by the SIE method. The figure is adapted from the literature [24].

To understand this particular behavior, simulations were performed using the SIE method.① The processing method in detail can refer the "Materials and methods" section. Numerical results for the different connected dimers are shown in Fig. 5.1, where panels (c) and (d) present the SH near-field intensities and the far-field SHG intensities obtained for different

---

① SIE calculations for SHG in this section are contributed by Dr.JérémyButet, and Prof. Olivier J. F. Martin in Swiss Federal Institute of Technology, Lausanne (EPFL), Switzerland.

incident polarizations, respectively. Comparing the excitation polarization dependences of SHG shown in Figs. 5.1(b) and (d), a very good agreement between the simulations and experiments is clearly seen.

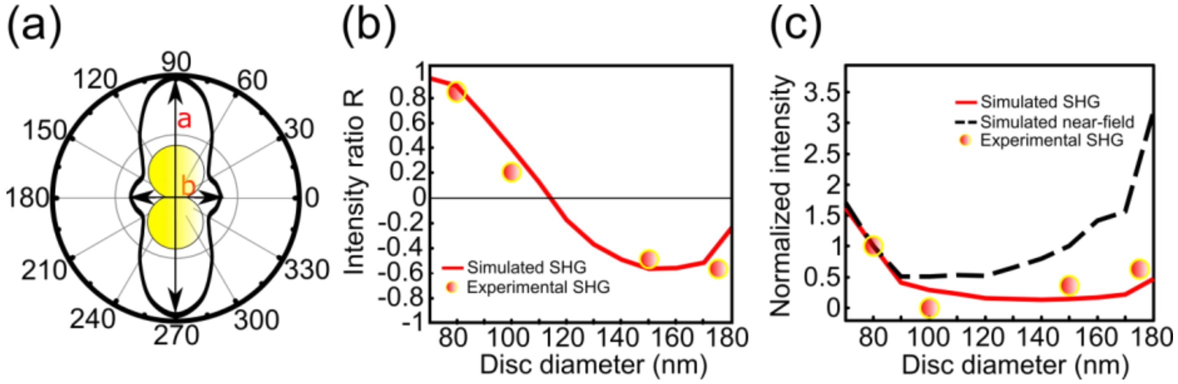

Figure 5.2 (a) The intensity ratio R is defined as (a-b)/(a+b). (b) The intensity ratios R are plotted for SHG as a function of the disc diameter d. The parameter R was evaluated from both the simulation (solid lines, steps of 10 nm) and experimental results (red dots). (c) The different dependences of the simulated far-field SHG (red solid line), fundamental near-field intensity (black dashed line) on the diameters of the discs. The figure is adapted from the literature [24].

To illustrate the gradual evolutions of the polarization-dependences as the nanodimer size changes, simulations have been performed for connected dimers with disc diameters ranging from 70 nm to 180 nm with a step of 10 nm. As shown in Fig. 5.2(a), an intensity ratio R=(a-b)/(a+b) is introduced to quantify the orientation of the polar plots that represent the excitation polarization dependent SHG signals, where a and b are the axial intensity values in the polar excitation plots along the long and short dimer axis, respectively. A positive R indicates that the optical signal maximum is observed by polarizing the incident wave along the long axis; whilst a negative R along the short axis. With this definition, a change in the sign of R implies the ‘flip’ phenomenon. As can be seen from Fig. 5.2(b),the sign of R changes from positive to negative values as the NP diameter increases, as shown by the red curve in Fig. 5.2(b), reproducing the ‘flipping’ phenomenon. These trends agree very well with the intensity ratio observed from our experimental results. The different dependences of the near-field and far-field SHG signals on the NP size are further demonstrated in Fig. 5.2(c). The simulated fundamental near-field intensity corresponds to the maximum of the external fundamental intensity enhancement observed close to the connection between the two NPs.

The experimental SHG is taken from the maximum intensities of the nonlinear spectra shown in Fig. 5.1(b). The incident wave is polarized longitudinally for both the experimental and theoretical results. All the data are normalized to the corresponding ones obtained for a disc diameter d = 80 nm. As one can clearly see, the SHG signals are not proportional to the square of the fundamental near-field intensity observed close to the junction between the NPs.

5.2 Resonant excitation dependence

To interpret the different evolutions of the intensity ratio R for SHG as the NP diameter increases, we now turn our attention to the plasmonic resonances supported by the connected dimers. Single particle dark-field optical spectroscopy was employed to detect the scattering spectra of the dimers, the nonlinear responses of which have been discussed so far. The measured scattering spectra are shown in Figs. 5.3(a), (b) while the corresponding numerical calculations performed using the Green's tensor method① are shown in Figs. 5.3(c), (d). The details about the microscope configuration and simulation can be found in the 'Materials and methods' section. The incident polarization is oriented either along the long axis or the short axis as depicted in the insets. As we can clearly see, there is a good agreement between the experimental and numerical spectra. In the case of the longitudinal excitation, two different maxima are observed in the scattering spectra as shown in Figs. 5.3(a), (c). The first mode appears between 500 and 610 nm corresponding to the coupled two quadrupolar modes, according to the charge distribution (1) shown in Fig. 5.3(c). As seen in Figs. 5.3(a) and (c), this mode shifts from around 550 nm for a disc diameter d = 100 nm to 607 nm (610 nm in the simulation) for d = 175 nm. The second mode is a longitudinal dipolar mode, which resonates at a wavelength around 820 nm for the smallest diameters. It corresponds to charge oscillations along the long dimer axis, the charge distribution of which can be seen in Fig. 5.3(c) as (2). As the diameter increases, this mode shifts to longer wavelengths beyond the spectral range detectable using our experimental setup. For incident light polarized along the short dimer axis, a transverse dipolar mode between 560 nm and 680 nm is observed, corresponding to charge oscillations along the short dimer axis as revealed by the charge

---

① The simulation on the scattering spectra by using Green's tensor method in this section is contributed by Dr.Gaëtan Lévêque in Institute of Electronics, Micro-electronics and Nano-technology, Lille, France.

distribution (3) in Fig. 5.3(d). This mode also red-shifts as the disc diameter increases but remains detectable with our dark-field microscope.

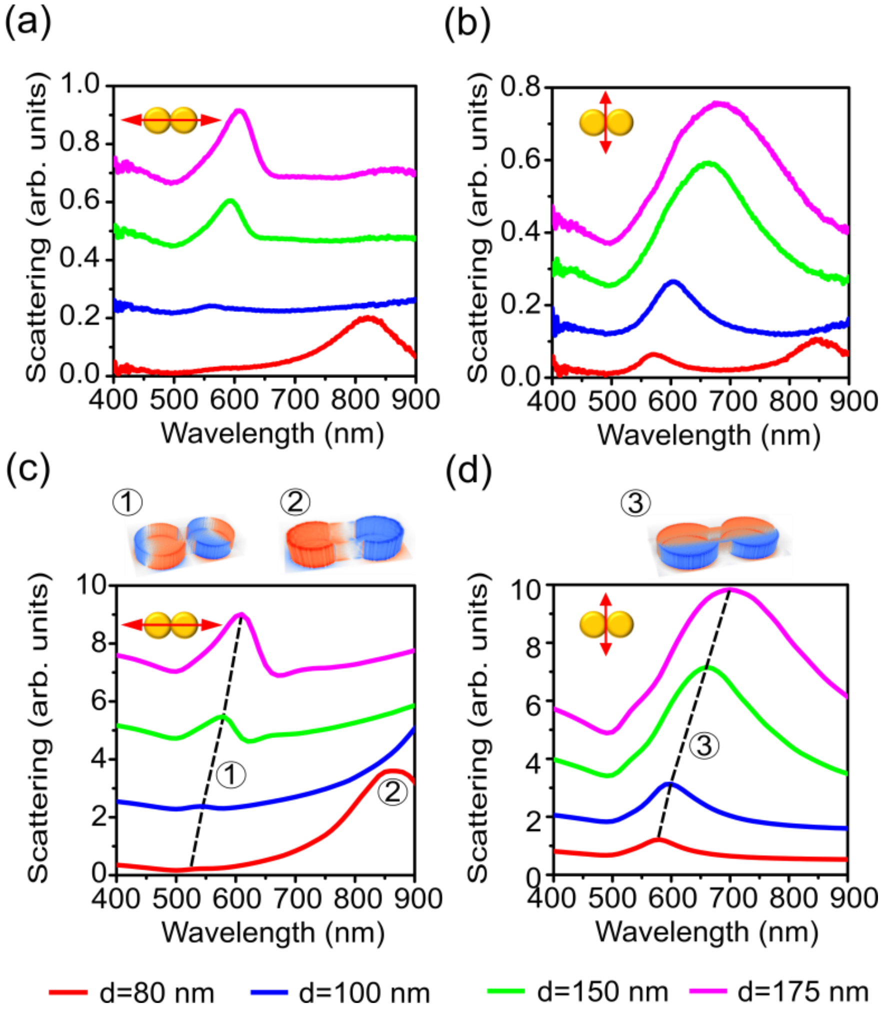

Figure 5.3 (a), (b) Measured dark-field scattering spectra of connected gold dimers with different disc diameters: d = 80 nm (red), 100 nm (blue), 150 nm (green), and 175 nm (magenta). The intensity is normalized to the lamp spectrum. (c), (d) Corresponding numerical calculations performed using the Green's tensor method. The incident polarizations are depicted in the insets as red arrows. The charge distributions associated with the different observed LSP modes are labelled ①,② and ③. The dashed lines in panels (c) and (d) highlight the shift of the LSPRs with the NP size. All the spectra in this figure[24] are offset vertically for a better visibility. The figure is adapted from the literature [24].

The enhancement of the nonlinear signals via the different localized surface plasmon modes can be well understood, with the investigated knowledge of the plasmon resonance properties. For the dimer with disc diameter d = 80 nm, due to the resonant excitation of the longitudinal dipolar mode at our fundamental wavelength, the maximum SHG intensity is achieved for an incident wave polarized along the long dimer axis. As the disc diameter increases, this resonance moves away from the excitation wavelength. On the other hand, the resonance of the transverse dipolar mode approaches to the fundamental excitation (774 nm) as seen in Fig. 5.3(d). The consequence is that the excitation efficiency of the transverse dipolar mode is improved, as seen Fig. 5.1(b). At the SH frequency, the near-field intensities around the dimers increase gradually as the disc diameter evolves from d = 100 nm to 175 nm, for an incident polarization along the short dimer axis. At the end, it outweighs the near-field strength generated with an incident polarization along the long axis. Therefore the SHG polarization-dependence plots 'flip' as the particle size increases.

5.3 Phase interference at SH frequency

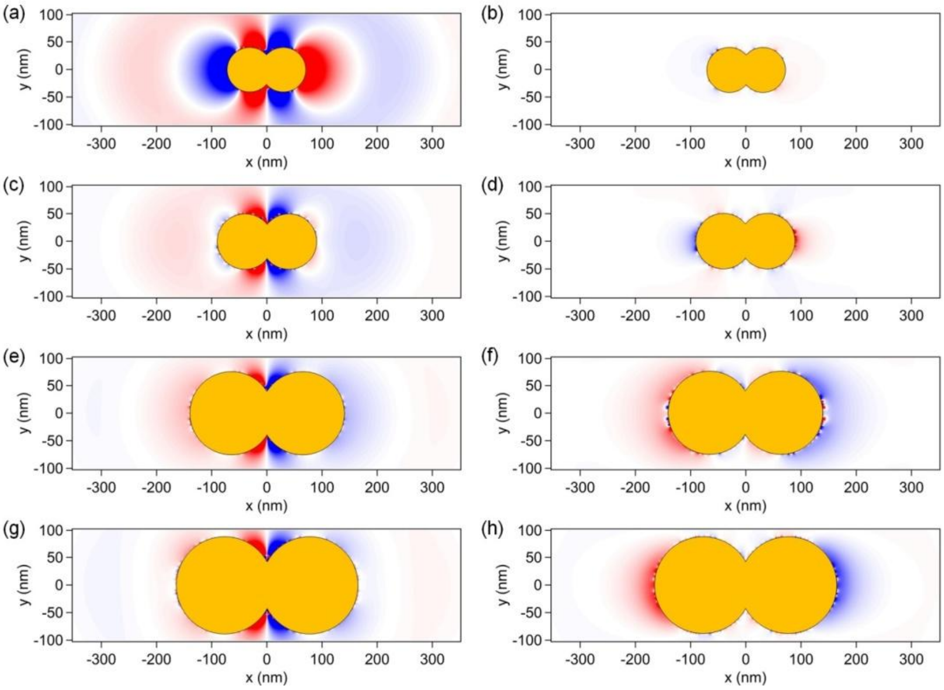

Figure 5.4 Real part of the x-component of the SH electric field in the vicinity of a connected gold dimer with a disc diameter (a) and (b) d = 80 nm, (c) and (d) d = 100 nm, (e) and (f) d = 150 nm, (g) and (h) d = 175nm. The incident wave is polarized either along (a), (c), (e), and (g) the long dimer axis or along (b), (d), (f), and (h) the short dimer axis. Positive and negative values are depicted in red and blue, respectively. The figure is adapted from the literature [24].

Notably, for dimers with disc diameters d = 150 nm and 175 nm, although strong electromagnetic 'hot-spots' at the SH frequencies can be observed around the touching points between the NPs when the incident wave is longitudinal polarized, the SHG intensity is smaller than that of transverse polarization. This phenomenon has been reported as the 'silencing' of the second order nonlinear response.[90] Despite a strong near-field enhancement is present, the nonlinear polarization vectors at each side of the touching point are out of phase and their contributions to the far-field SH wave tend to cancel out each other, as seen Fig. 5.4. The destructive interference finally results in a limited far-field SH signal, despite the amplitude of the nonlinear surface polarization. Note that this 'silencing' effect is present in all the connected dimers, but results in a 'flip' of the SH response only if the SHG for an incident wave polarized along the short dimer axis is high enough, i.e. for large disc diameters.

5.4 Summary

This observation of SHG flipping effect indicates that the measurement of electromagnetic hot-spots using nonlinear optical processes is not direct, since a competition between different enhancement mechanisms of the nonlinear response often occurs. To understand this 'flip' phenomenon of polarization-dependent far-field SHG radiation, both the plasmon resonance and the polarization of the local near-field at the electromagnetic 'hot-spot' should be considered.

Chapter 6 MPL emission channels in the weak electromagnetic field

Classical description on the MPL emission is attributed to the recombination of excited electrons in the higher conduction bands (above Fermi energy levelE_f) and holes in the lower valence bands.[18, 46, 53] The spectral emission are thus mainly determined by their intrinsic material properties, e. g. the energy bands. This mechanism successfully explains most of experimental results from the metallic film or bulky crystal. Rough surface usually gives much stronger MPL due to the lighting rod effect, or the local field enhancement supported by particle plasmons (PPs).[18, 92] That's also the reason for the investigation of MPL on NPs becomes more and more important since the dependence of PPs on their individual shapes, size, and dielectric environment.[1] The role of PPs on the emission of MPL is generally viewed as a source for strong local field enhancement, which is able to modify the radiative decay rate during the electron-hole recombination.[51] Nevertheless, more and more evidence show that the MPL has similar profiles to far-field scatterings, which give the fingerprints of PPs.[16, 50] The emission of MPL is then attributed to the radiative decay from the energy levels of PPs. The PPs supply extra decay channels for the excited electrons.[24, 60, 93] In this way, the surface properties of NPs such as the size, shape and the embedding dielectric environment of the NP, dominate the emission behavior of MPL.

In this section, the MPL emitted from smooth Au films and Au NPs via ultrafast laser pulses in a scanning confocal optical microscope is systemically investigated. By comparing the emission spectra from Au films and Au NPs of varying dimensions with the dark-field scattering spectra, it is found that MPL originates from both contributions: the direct electron-hole (e-h) pairs recombination and the decay channel from PPs. The former is attributed to the radiative decay, namely e-h pairs emission mode. The latter is attributed to the plasmon-assisted non-radiative decay of photo-excited d band holes, namely PPs emission mode. a model of total emission quantum efficiency (TEQE) involving both contributions is introduced, to evaluate the radiative emission capability per e-h pair, and explain the weighting ratio between two emission modes in accordance with the size effect of d hole scattering rate.

6.1 PPs VS MPL

Arrays of Au nano-discs are fabricated on the ITO glass using EBL. The designed diameter of gold NP changes from 80 to 180 nm with a step of 20 nm. For each dimension, five different exposure doses are used to obtain finer dimension differences (~ 5 nm). Two identical zones including the NPs with all dimensions are designed. One of them is for initial characterization with SEM, and the other is for optical measurements. The structure height is 50 nm. The distance between each NP is 5 μm such that the dark-field scattering and the nonlinear optical measurements can be performed at a single particle level with confocal microscopy. A detailed description of the fabrication procedure can be found in the "Materials and methods" section.

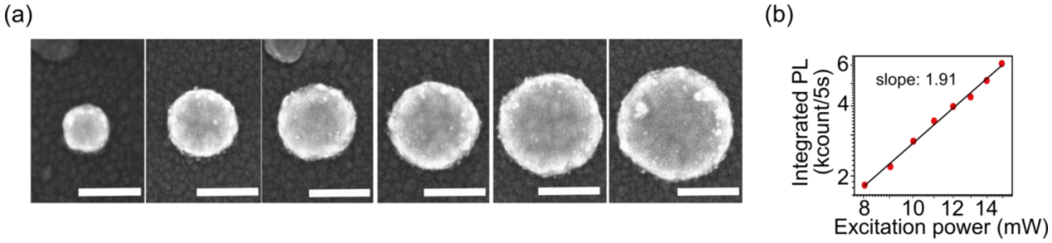

Figure 6.1 (a) SEM images of single Au NPs fabricated by e-beam lithography. The disc diameter from left to right is 80 nm, 100 nm, 120 nm, 140 nm, 160 nm and 180 (5 nm tolerance). The scale bars in each SEM image are 100 nm. (b) Excitation power dependent PL intensity (integrated from 390 to 700 nm) for a single Au NP with a diameter of 100 nm in a double logarithmic coordinate. The slope value of 1.91 indicates a two-photon absorption process. The incident power is measured in front of the parabolic mirror.

The plasmonic nanostructures are then characterized in a dark-field scattering microscope and a home-built scanning confocal optical microscope. Full descriptions of dark-field scattering and nonlinear measurement can be found in the "Materials and methods" section.

Fig. 6.1(a) shows the SEM images of Au discs with the diameter from 80 nm to 180 nm with a step of 20 nm. The scale bars in each SEM image are 100 nm. Fig. 6.1(b) shows the excitation power dependent MPL intensity (integrated from 390 to 700 nm) measured at single Au NP with a diameter of 100 nm in a double logarithmic coordinate. The slope value of about 2 indicates a two-photon absorption process, giving rise to the TPL signals measured in our experiment.

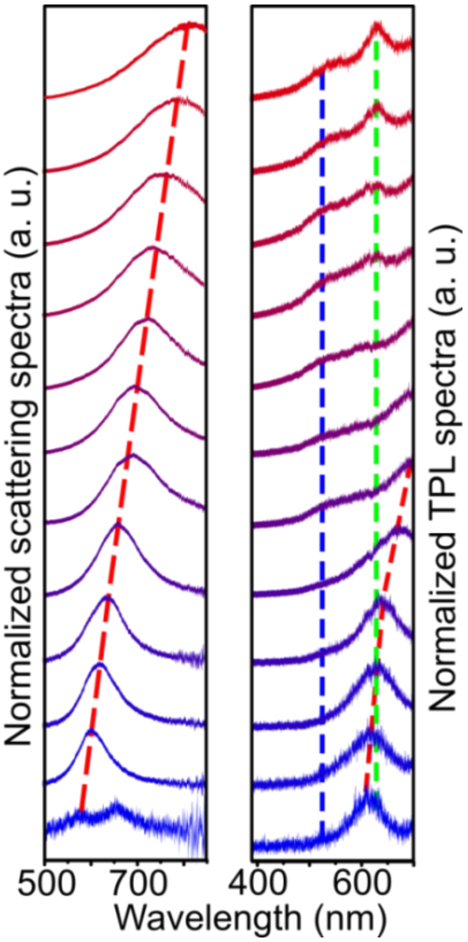

Figure 6.2 The comparisons between normalized dark-field scattering spectra (left column) and MPL spectra (right column) for single Au NPs with varying diameters from 80 (the bottom) to 190 nm (the top) at a step of 10 nm. The red dashed lines show the peak position shifts. Three emission modes are found from the MPL spectra: two static modes with a shoulder centering at 540 nm (blue dashed line), a sharp peak situating at 630 nm (green dashed line) and one shifting mode with a red-shifting peak as disc size increases. The integrating times for the scattering and MPL spectra are 2s and 5s.

The plasmonic nanostructures are characterized in a dark-field scattering microscope and a scanning confocal optical microscope, to explore their linear and nonlinear optical properties respectively. Scattering spectra of single Au discs with varying diameters from 80 (the bottom) to 190 nm (the top) at a step of 10 nm are show in the left column of Fig.6.2. A red shift of peak position and broadening of spectral line width can be clearly seen when the disc size increases. The right column shows their corresponding MPL spectra. Three emission modes are found from the MPL spectra: two static modes and one shifting mode.For the smaller NPs (less than 140 nm), the shifting emission mode (red dashed line) can be clearly seen, and the peak position of which has a gradual red-shift as the size increases until it moves out of our detecting window. In the meantime, two static modes with a broad shoulder centering at around 540 nm (blue dashed line) and a tiny peak situating at 630 nm (green dashed line) starts to be visible and keep the same positions as the diameter increases.

6.2 Shifting emission mode

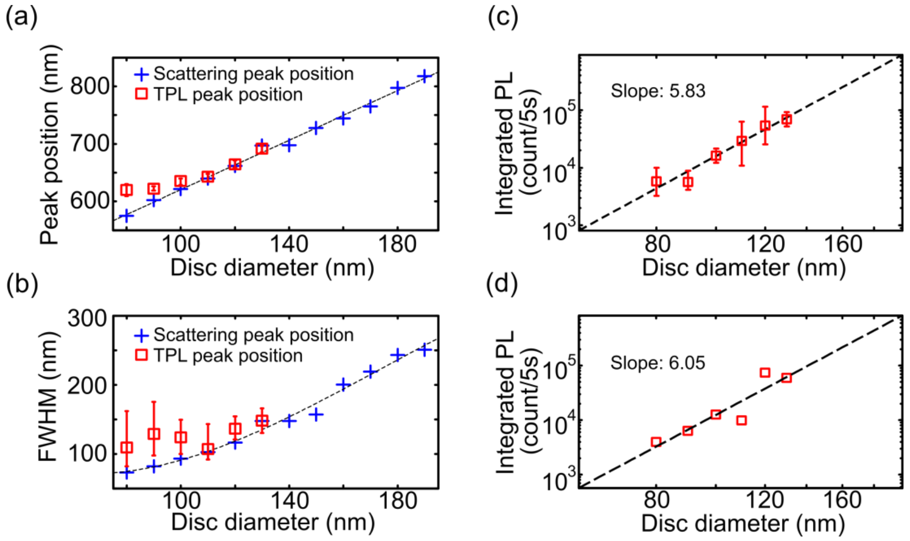

Figure 6.3 The comparisons of peak position (a) and FWHM (b) between the dark-field scattering spectra (blue cross) and the shifting emission mode of MPL (red square) for the smallest Au NPs (less than 140 nm). (c) The integrated PL of shifting emission mode as a function of disc diameter in double logarithm coordinates. The slope value of linear fit line is 5.83. The error bars in (a)~(c) derive from the measurements with different excitation polarizations. (d) is similar to (c) except the discs are excited in the same polarization. The slope value of linear fit line is 6.05.

The peak positions and FWHMs of the shifting emission mode of MPL spectra are compared with the corresponding scattering spectra, as seen in Fig.6.3(a) and (b), respectively. For guiding the eyes, the experimental data are fitted by linear (a) and quadratic (b) functions, depicted as black dashed curves.The peak positions of MPL spectra in the detectable range agree very well with the corresponding scattering spectra, except that there is a slight of red-shifts for the smallest NPs. The MPL spectra generally have wider line widths, comparing with the one of scattering spectra. The red-shift and line width broadening may due to the harmonic oscillator damping in the near-field and the dephasing of polycrystalline.[94] The error bars are derived from measurements with different excitation polarizations, which are turned a round as a step of 20 degrees. As we can see, the peak positions are much less affected by the excitation polarization than it is for the FWHM.

The integrated MPL from the shifting emission mode (integration from 390 nm to 700 nm) for the smallest NPs in different excitation polarizations versus the diameter of Au NPs is shown in a double logarithm coordinate as Fig.6.3(c). The slope value of linear fit line is 5.83.The integrated MPL from the shifting mode as a function of disc diameter of the smallest NPs excited in one polarizations are shown in Fig. 6.3(d). The slope value of linear fit line is 6.05.MPL intensity from the shifting emission mode is proportional to the power 6 of disc size, having the same dependence as the square of NP volume. This can be easily explained by the fact that the one-photon absorption cross-section of NP in the interband absorption region is proportional to the NP volume.

On the whole, the similar dependences of peak position, FWHM of MPL on the particle size to that of NP scattering spectra imply the strong connection between this emission mode and PPs of NPs.The shifting mode is thus called PPs emission mode for a simplification.

6.3 Static emission modes

The emission of MPL is classically explained by the recombination of excited electrons in the conduction bands and holes in the valence bands. The same phenomenology method is used to predict the emission spectra induced by the interband transitions from different high symmetric points, e.g. X and L points (see “Theoretical background” section 2.4.2).[18, 48]

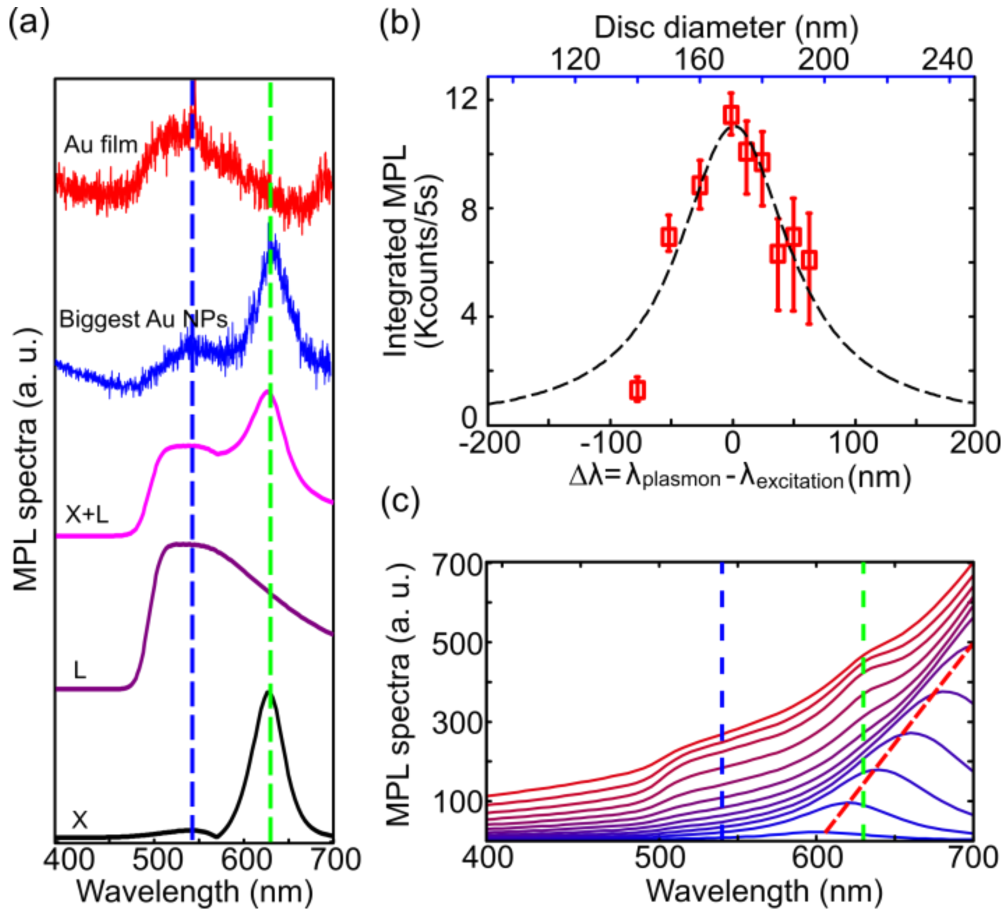

Figure 6.4 (a) Normalized MPL spectra from Au film (red line) and biggest Au NPs (blue line). The PPs mode background is subtracted. The experimental spectra compare with the calculated emission spectra resulting from the direct electron-hole recombination between sp band and d band near the X (black line) and L (violet line) symmetric points in the first Brillouin zone. The superposition of the recombination from two symmetric points is drawn as a magenta line. The peaks situating at 540 nm (blue dashed line) and 630 nm (green dashed line) correspond the e-h radiation mode shown in Fig. 2.(b) The integrated MPL intensity from the e-h pair modes versus the disc diameter (top X coordinate) and the wavelength difference between PPs and the fundamental excitation. The experimental data is fitted with a Lorentzian function (black dashed line). (c) The calculated MPL spectra combining both contributions from PP mode (red dashed line) and e-h pair mode (blue and greed dashed lines) for the Au NPs with the diameter ranging from 80 nm to 190 nm as a step of 10 nm.

Fig. 6.4(a) shows the emission spectra resulted from the direct e-h recombination between sp band and d band near the X (black line) and L (violet line) symmetric points in the first Brillouin zone. The calculated emission spectrum from X symmetric point has two peaks at around 630 nm and 540 nm. The former one is due to the electron density of state and the corresponding distribution, while the latter is due to the d band holes.[18] The two contributions are also the cause for line width broadening of L symmetric point emission. The superposition of the emission spectra from two symmetric points (X+L) is drawn as a magenta line. Clear similarities can be found between the superposed spectra (magenta line) and the static emission modes from the biggest Au NPs (blue line). This implies that the static peaks at 540 nm and 630 nm in Fig. 6.2 (right column) are induced by the e-h recombination from L (blue dashed line) and X (green dashed line) symmetric points. The peak position of static emission modes reflects the bulky properties of a specific material, e.g. the energy band and optical density of state, neglecting the size effect and excitation polarization dependence. This explains the phenomanon that static emission modes maintain their peak positions with the disc size increases in Fig. 6.2 right column.

Further evidence is found from the bulky Au film, which is thermally evaporated with a thickness of 50 nm. The PL spectrum (red solid line) has the similar profile as the calculated emission spectra from the direct e-h recombination from L symmetry point, as shown in Fig. 6.4(a). By the same token, the static emission modes with peaks at 540 nm and 630 nm are also named as e-h pairs emission modes.

The tendency of integrated MPL intensity originated from e-h pairs mode is also investigated as a function of the disc diameter. As shown in Fig. 6.4(b) (blue axis), the integrated intensity from the big NPs (larger than 140 nm) increases with the NP size until the diameter reaches 170 nm. After that, the intensity shows a descend trend with the NP size increases. The error bars come from the data analysis subtracting the PPs emission mode.

Extracting the e-h pairs emission mode of MPL can be simplified by linearly subtracting its spectral background of PPs emission mode. The extracting start is always set as 480 nm, as it is the lowest point in the background. The extracting ends are set as 660 nm (yellow), 665 nm (magenta), 670 nm (green), 675 nm (cyan) and 680 nm (blue), as shown in Fig. 6.5(a). The extracted MPL spectrum (black line) ranging from 480 to 670 nm is then fitted by a two-order Lorentzian function (red dashed line), as seen in Fig. 6.5(b). Two separated peaks situating at 540 nm (blue dashed line) and 630 nm (green dashed line) can be found. The final step of the data analysis is shown in Fig. 6.5(c). The averaged value (black dashed horizontal line) is taken as the intensity of e-h pairs emission mode for such size of Au disc. The biggest and smallest values are used to define the upper and lower limits in the error bars, shown in Fig. 6.4(c).

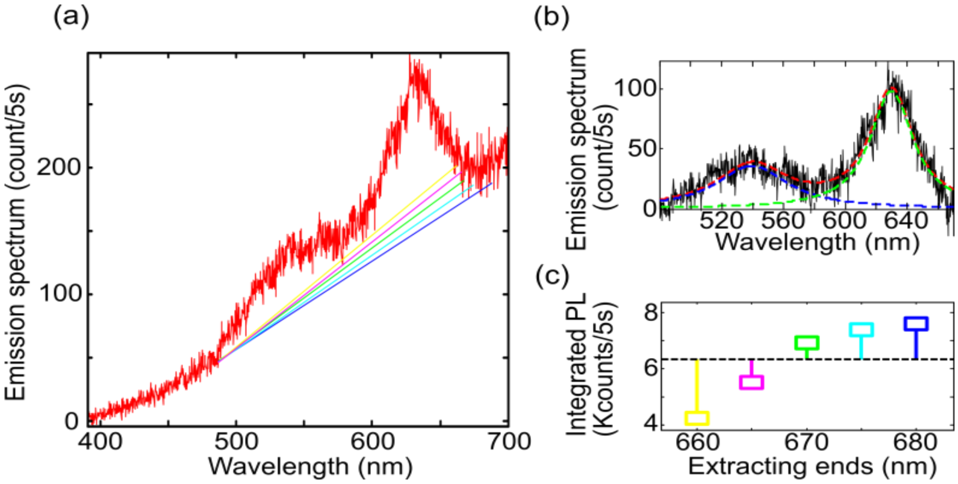

Figure 6.5 (a) The original emission spectrum of a Au disc with the diameter of 185 nm. (b) An example for fitting the extracted e-h pairs mode MPL. The extracted MPL spectrum (black line) ranges from 480 to 670 nm, and it is fitted by a two-order Lorentzian function (red dashed line). Two separated peaks situating at 540 nm (blue dashed line) and 630 nm (green dashed line) can be found. (c) The integrated MPL of the fitted spectra from 5 extracting ranges, which correspond to the ones in (a).

Notably, a clear tendency can be found if the integrated intensity becomes a function of the wavelength difference Δλ between PPs λ_{plasmon} and the fundamental excitation $\lambda_{\text{excitation}}$ (774 nm). Surprisingly it is found that the integrated MPL from e-h pairs emission mode increases with the decrease of the absolute value Δλ and reaches the maximum when Δλ approaches to zero. The phenomenon can be well-explained by the "resonant excitation" effect: the MPL emission becomes stronger when the PP of NP is closing to the fundamental excitation, and vice versa. This can be explained by the Lorentzian oscillator, where oscillation becomes most forceful once the extern oscillating frequency fits with the natural frequency of the object, which has been explained in "Theoretical background" section 2.3.[1, 36] The experimental data is fitted with a Lorentzian function, as indicated by the dashed black line in Fig. 6.4(b). The fit intensity becomes the strongest when the Δλ equals to zero, which agrees very well with the expectation.

So far, MPL comprises two emission modes, namely PPs and e-h pairs modes, has been analyzed separately. The spectral properties of PPs mode, such as the peak position and

FWHM, can be evaluated by the simulated scattering or absorption cross-section of NP, while e-h pairs mode by the superposition of e-h recombination from L and X symmetric points. The amplitudes for both modes have strong dependences on the excitation process, but follow different rules. The emission intensity of PPs mode is proportional to the interband absorption cross-section for each photon, and that of the e-h pairs mode can be explained by a Lorentzian oscillator. The amplitude tendencies of PPs and e-h pairs modes can be fitted by the power of 6 and Lorentzian functions of the NP size, respectively. Combining the calculated spectra properties (peak position and FWHM) and experimentally fitted amplitudes, the MPL spectra can be well predicted, as shown in Fig. 6.4(c). Following this procedure, the MPL spectra of Au NPs with the diameter increasing from 80 nm to 190 nm as a step of 10 nm are calculated. The evolutions of e-h pairs and PPs emission modes are indicated by the blue, green and red dashed lines, respectively. As can be clearly seen, the superposition of the PPs and e-h pairs emission modes agree very well with the experimental results shown in the right column of Fig. 6.2.

6.4 Total emission quantum efficiency

The observation and interpretation of the two different emission channels supply a physical view to understand the radiation nature of MPL. The physical mechanism can be depicted in Fig. 6.6. Suppose that the excited electrons and holes arrive at the emission states, following their individual photo-excitation and relaxation steps. The electrons and holes either recombine radiatively in terms of photons (①), or non-radiatively in terms of phonons (②) and plasmons (③). The energy states of the PPs should be around the Fermi level E_f. The excited PPs either decay radiatively in terms of photon (④), or non-radiatively in terms of phonon (⑤). Therefore, two contributions are responsible for the emission of MPL: radiative recombination of e-h pairs channel ① and radiative decay of PPs channel ④.The double-direction arrows in the channels ① and ② indicate the e-h recombination process: the electrons sink down the upper band and the holes float up the lower band.[18]

The recombination of photo-excited electrons and holes can be treated as a radiation process of a transition dipole which is created by the intra- (most for single-photon induced PL) or interband (most for multiphoton induced PL) transition. The radiative and non-radiative decay rates of the spontaneous emission have been modified, as long as the dipole is at the vicinity of noble metal NPs.

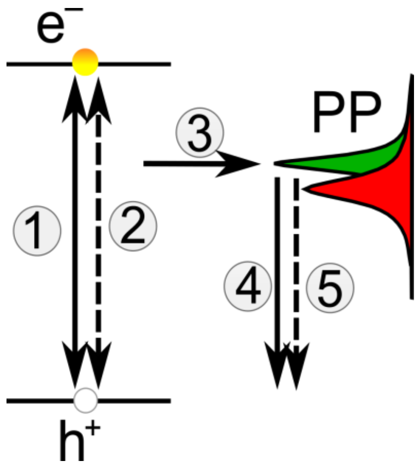

Figure 6.6 A Sketch showing the physical mechanism of the MPL emission. Suppose both photo-excited electrons and holes arrive at the emission state. The electrons and holes either recombine radiatively in terms of photons (①), or non-radiatively in terms of phonons (②) and plasmons (③). The energy states of the PPs are around the Fermi level E_f. The excited PPs either decay radiatively in terms of photon (④), or non-radiatively in terms of phonon (⑤). The MPL therefore derives from two parts: direct e-h recombination and sequentially radiative decay channel(①) and indirect PPs-mediated radiative decay channel (④).

On one hand, the radiative decay rate Γ_r is greatly enhanced by the localized electromagnetic field, comparing with the radiation in free-space.The radiative decay rate $\Gamma_r = M\gamma_0^r = (\mu + \mu_{ind})^2\gamma_0^r/\mu^2$with M represents the local field enhancement factor,$\gamma_0^r = 4\sqrt{\varepsilon_0}k_0^3\mu^2/3$ is the free-space radiative decay rate, μ is the intra- or interband transition dipole moment and μ_{ind} is the dipole moment induced by the electric field.[95]

On the other hand, the non-radiative decay rate Γ_{nr} is modified by the strong localized environment as well, comparing with the case in free-space. Notably, PPs are generated by d-hole Auger scattering during such non-radiative decay process,[95] which supply extra channels for photon emission. For a simplification, $\Gamma_{nr} = \Gamma_0^{nr} + \Gamma_p$, where Γ_0^{nr} is the bulky non-radiative decay rate in free-space (process ②), and $\Gamma_p$is the plasmon-assisted non-radiative decay rate (process ③), which is responsible for the MPL emission at PPs frequency.The bulk non-radiative decay rate $\Gamma_0^{nr} = -2Im(\mu \cdot E)$ with E is the electric field induced by the dipole μ itself,[95] will not change with NP size. The photon emitted from the PPs channel is decided by the scattering rate of excited d holes during the Auger scattering.[51]

Assuming that excited d holes are locating at the centers of NPs, the dipolar approximation of the d hole scattering rate for a resonant PP in multiphoton PL case is defined as:[57, 58]

$$\Gamma_p = \gamma_h^s(E) = -\frac{9e^2\mu^2}{m^2(E^{cd})^2R^3} Im \frac{N(E^c - E) + f(E^c)}{\varepsilon_s(E^c - E)} \tag{6.1}$$

For single-photon PL, the scattering rate becomes:[57, 58]

$$\Gamma_p = \gamma_e^s(E) = 9\pi \frac{E_0^2}{\omega_s} \frac{E}{E_F} (\frac{E - \omega_s}{E_F})^{1/2} [1 - f(E - \omega_s)] \tag{6.2}$$

where $E_0 = (2mR^2)^{-1}$, R is the radii of nanosphere; ω_s is the surface plasmon frequency; $f(E)$ is the Fermi-Dirac distribution; $E^{cd} = E^c - E^d$ is the energy difference between conduction band and d band; $N(E)$ is the Bose distribution; $\varepsilon_s(\omega)$ denotes $\varepsilon_d(\omega) - \omega_p^2/\omega(\omega + i\gamma_s) + 2\varepsilon_m$, where ε_m is the dielectric constant of embedded medium; ε_d is the dielectric constant considering the interband contribution; ω_p is the bulk plasmon frequency and γ_s is the damping constant.

It is further assumed that the radiative efficiency of a PP mode isγ_p. The TEQE of MPL, which represents the average number of radiated photons per excited e-h pair can be defined as:

$$Q(E, R) = \frac{\Gamma_r + \gamma_p \Gamma_p}{\Gamma} = \frac{\Gamma_r}{\Gamma}(1 + \sigma\gamma_p) \tag{6.3}$$

where $\sigma = \Gamma_p/\Gamma_r$.

Besides strong dependences on the excitation process, the photon emission intensities from the two channels also have strong connection with the d-hole scattering rate. In the following, the reason why the emission of MPL behaves more e-h pairs emission channel for the bulk and PPsemission channel for the NPs will be explained from the aspect of emission process.

For the bulky material, such as metallic film, the size parameter R in Eqs. (6.1) and (6.2) will approach to infinitive. Thus, σ approaches to zero, which implies that no plasmon will be generated during the non-radiative decay process of e-h pair recombination. TEQE $Q \approx \Gamma_r/\Gamma \approx \Gamma_r/(\Gamma_r + \Gamma_{nr})$. The emission of MPL is determined by the e-h pairs emission channel, as depicted the channel ①in Fig.6.6.

On the other hand, when the investigating object is NP, e.g.$R < \lambda$,Γ_p becomes comparable withΓ_r. The emission of MPL is the combination of e-h pairs and PPs emission channels, which is the case for our experimental observation. In an extreme situation: $\Gamma_p \gg \Gamma_r$, TEQE $Q \approx \gamma_p \Gamma_p/(\Gamma_p + \Gamma_{nr})$, which indicates that the emission of MPL will be dominated by the PPs channel, as depicted as ④ in Fig.6.6.

6.5 Summary

The MPL emitted from smooth Au films and Au NPs via ultrafast laser pulses in a scanning confocal optical microscope is systemically investigated. By comparing the emission spectra from the Au NPs of varying dimensions with the dark-field scattering spectra, it is found that the MPL consists of the contributions from two channels, namely the PPs and the e-h pairs emission channels. The similar behaviors between MPL from PPs emission channels with corresponding the scattering in terms of peak position and FWHM suggest that this part derives from the radiative decay of PPs. The MPL intensity from the PPs emission channel is proportional to the power of 6 on the NP size. The PPs are excited via Auger scattering of photo-excited d band holes. MPL from the e-h pairs emission channel has the same radiation energies at the e-h recombination from X and L high symmetric points, and strong dependence of intensity on the ‘resonant excitation’, which can be explained by a Lorentzian oscillatior. This part of emission is attributed to the plasmon-enhanced radiative decay of e-h pairs. A physical model of TEQE involving both contributions to quantify the radiative emission capability per e-h pair, and and explain the weighting ratio between two emission channels in accordance with the size effect of d-hole scattering rate.The experiment results and the theoretical model supply a new approach to calculate MPL spectrum.

Chapter 7 AMPL in strong electromagnetic field

Ultrafast laser pulses are usually employed to obtain considerable MPL. The absorbed quantum number of photons can be evaluated by the fitting slope in a double logarithmic coordinate of the emitted MPL intensity versus incident laser intensity, namely power law exponent coefficient. The slope value generally is not larger than two due to the fast relaxation of the first excited electron in the conduction band.[96] Nevertheless, many studies reported that the slope value can reach 18 in the avalanche-like MPL from coupled Au nanowires.[97, 98] Similar phenomenon was observed from the Ag nanowire arrays and monomers.[98-100] The reason was attributed to the local field enhancement contributed by SPR[97] or purely thermal radiation.[98] However, the physical nature is still unclear.

Giant MPLs from the coupled Au-Al nanodimers are observed in our experiment once the incident beam exceeds a critical intensity. At this stage, the emission intensity is shown to be more than one order of magnitude larger than the case before the critical intensity, and shows dramatic changes in spectral profile. The hugely amplified and spectrally irreversible PL is the so-called avalanche multiphoton photoluminescence (AMPL). In the mean time, the nanostructures suffer inevitable thermal damages once AMPL is generated. After a series of incident intensity dependent and excitation polarization dependent experiments on the Au-Al heterodimers with varying sizes and gaps, it is found that it is such thermal damaging process giving rise to the super intensive MPL. Beside the increase of incident intensity, another strategy to trigger the AMPL is to alternate the excitation polarization, where the local field enhancement at the NP should be taken into account. The physical mechanism is explained by Keldysh rate equations, and the optical breakdown threshold is quantitatively evaluated via a two-temperature model. Furthermore, the linear function between power law exponent coefficient and the emitted photon energy supplies an approach to evaluate the emission intensity of AMPL. Finally, the spectral change from the LSPR modulated profile to the one that indicates the direct recombination from hot electron-hole pairs is discussed from the view of temperature dependent d-band hole scattering rate.

7.1 The sample and measurement

Arrays of Au-Al heterodimers are fabricated on the glass using double EBL technique.①The diameter of Au NPs changes from 80 to 200 nm with a step of 20 nm. For each size of Au NP, the diameter of Al NP is varied from 120 to 240 nm with a step of 20 nm. The gap for each Au-Al heterodimer varies from touching (no gap) to 200 nm with a step of 20 nm. The structure height of the NP is 50 nm. The distance between each adjacent heterodimer is 5 µm such that the dark-field scattering and the nonlinear optical measurements can be performed at a single particle level with confocal microscopy. The Au and Al monomers of the same dimensions are also fabricated as reference samples for the homo- and hetero-dimers. For simplification, the expression of "Au120-Al160-g20" is used to represent a heterodimer that is composed of a Au NP with a diameter of 120 nm, and a Al NP with a diameter of 160 nm. The edge-to-edge gap distance between the Au and the Al NPs is 20 nm. For the connected heterodimer, the denotation for the gap distance is omitted. The plasmonic nanostructures are characterized in the home-built scanning confocal optical microscope, as shown in 'Materials and methods' section. To modulate the incident power, a gradient grey filter is used. Once the optical density of the gradient grey filter is changed, the averaged laser power is measured in front of the parabolic mirror. The incident laser intensity is taken as $1/e^2$ of the peak intensity. All the incidence intensity values used in the manuscript are calculated considering the averaged laser power and the size of the laser focus in the parabolic mirror (diffraction limit 380 nm).[28, 78] To achieve the required polarization, the excitation beam is delivered through a lambda-half wave plate. The spectra are taken at the touching points for the connected nanodimers and at the gap centers for the gapped nanodimers, respectively. For the ones with sizes smaller than the dimension of the laser focus, the spectra are collected at the centers of Airy disks appeared in the PL image.

---

① The Au-Al heterodimer samples in this section are prepared by Dr. Anne-Laure Baudrion in University of Technology of Troyes.

7.2 AMPL occurrence

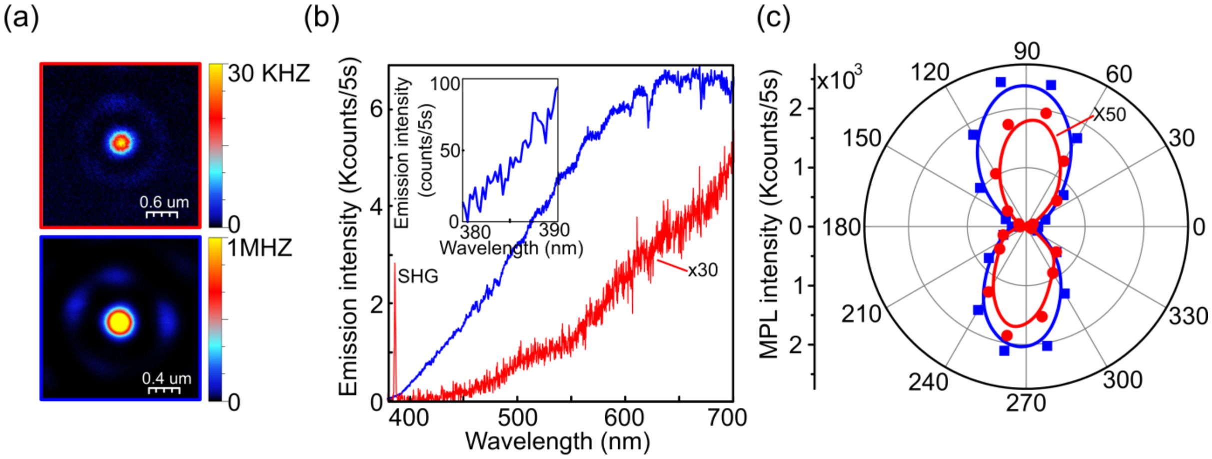

Figure 7.1 The optical images (a), emission spectra (b) and the dependence of integrated intensity on the excitation polarization (c) before (red square in a, red line in b, and red dots and solid line in c) and after (blue square in a, blue line in b, and blue squares and solid line in c) the occurrence of AMPL for a single connected Au120-Al140 heterodimer. For a better visibility, the PL signals in (b) and the integrated intensity in (c) before the AMPL occurrence are multiplied by 30 and 50 times, respectively. The PL intensity in (c) is the integration of the emission spectra from 390 to 700 nm. The dimer long axis situates at around 80 ° in the polar plot (c). The incident beam is linearly polarized along the dimer long aixs and the beam intensity in the focus of parabolic mirror is 69 GW/cm^2.

The AMPL is firstly observed from the contacted heterodimers or the ones with smaller gaps (gap size <40 nm) during a temporary slight increase of incident power (<1mW). The emission intensity turns out more than one order of magnitude larger and shows dramatic spectral changes, comparing with the case before the appearance of AMPL. When the incident power returns to its initial value, the emission intensity and the nonlinear spectral shape doesn’t restore. Fig.7.1 shows a typical example for such a dramatic change before and after AMPL occurrence, from the view of optical image (a), nonlinear spectrum (b), and excitation polarization dependent emission intensity (c), respectively. The incident laser intensity in the focus of parabolic mirror is 69 GW/cm^2, and the incident beam is linearly polarized along the dimer long axis. The optical measurement is taken on a single connected Au120-Al140 heterodimer. As can be seen from Fig.7.1(a), the maximum of integrated nonlinear optical signal (360-680 nm) once AMPL occurs is more than 30 times stronger than that before AMPL. The emission spectrum also shows irreversible change. As shown in Fig.

7.1(b), the PL signals increase by more than 30 times of amplitude after the occurrence of AMPL. On the contrary, the SHG suffers a sharp fall. The excitation polarization dependent PL intensity (integration from 390 to 700 nm in the emission spectra) is shown in Fig. 7.1(c). The red dots represent the dependency before AMPL, which is multiplied by a factor of 50 for a better visibility. The blue squares are the one after AMPL. The dipole-emission-like solid curves serve for guiding the eyes. It can be seen that these patterns change not only in the intensity, but also the orientation after the occurrence of AMPL.

7.3 AMPL trigger strategies

7.3.1 Influences of the incident power

To obtain a complete picture of the whole process of AMPL, the incident beam intensity is increased step by step from an initial value of 34 GW/cm^2 and linearly polarized along the dimer long axis. It is found that once the laser intensity exceeds a critical value (around 70 GW/cm^2), AMPL takes place. To facilitate the discussion, the occurrence of AMPL is defined by two steps: ① pre-AMPL step, when the laser intensity is below the threshold; ② post-AMPL step, when the incident power is beyond the threshold. The laser intensity dependent measurements are conducted on a single connected Au120-Al160 nanodimer. As shown in Fig. 7.2(a), the integrated emission intensity involving MPL and SHG as a function of incident laser intensity is plotted in a double logarithmic diagram. Regarding the MPL, the slope value of 2.1in the pre-AMPL step (red dots) indicates a two-photon absorption process, while the slope value of 2.9 in the post-AMPL step (blue dots) indicates a three-photon absorption process. The MPL intensity increases by around 20 times once beyond the critical laser intensiy. The slope value of SHG (triangles in the inset of Fig. 7.2(a)) is around two in the pre-AMPL step. On the contrary, its intensity falls by around 10 times once the laser intensity exceeds the threshold. The similar phenomenon has also been found from other connected heterodimers, as shown in Fig. 7.2(b). The heterodimers investigated here are Au200-Al200 (green triangle), Au200-Al180 (red circle), Au200-Al120 (blue star), Au120-Al220 (dark green square), Au120-Al120 (magenta diamond) and Au120-Al180 (black pentagram). Their corresponding fitted slopes are 2.0, 2.1, 2.0, 2.9, 3.7 and 4.2, respectively.

The cases before the occurrence of AMPL are marked as ①with a red background; for the ones after the AMPL occurence are marked as ②with blue background.The incident beam is linearly polarized along the short dimer axis. The AMPL of heterodimers in the step ② is triggered by the same strategy as (a) in advance.It can be clearly seen that the excitation of a single connected heterodimer which is absent from the AMPL is a two-photon absorption process, while more than two photons are absorbed once the AMPL takes place.

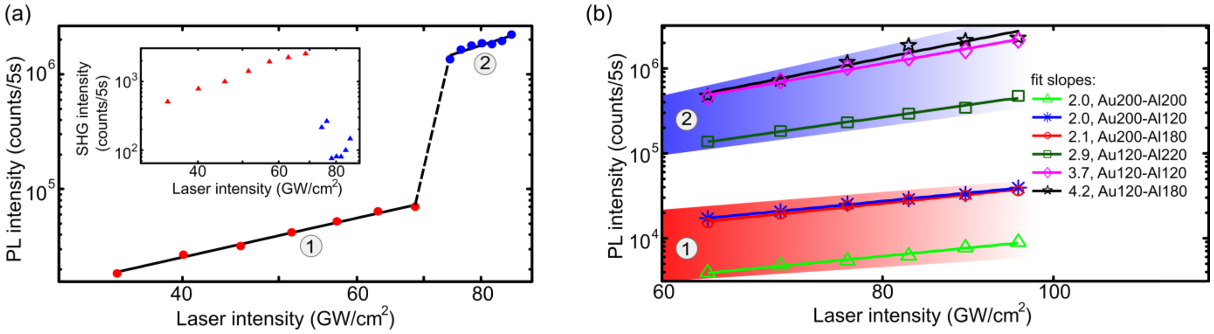

Figure 7.2 Double logarithmic plot of the emission intensity versus the incident beam intensity before and after the AMPL effect for single connected Au-Al heterodimers. (a) The incident beam intensity dependent emission intensity involving MPL (dots) and SHG (triangles in the inset). The AMPL occurs during the incident beam intensity in focus increases from 34 GW/cm^2 to 86 GW/cm^2. The threshold is around 70 GW/cm^2. The whole process is divided into two steps: ① pre-AMPL step and ② post-AMPL step. The slope of SHG during pre-AMPL step in the inset is around two. The optical measurement is taken on a single connected Au120-Al160 heterodimer. The incident beam is linearly polarized along the dimer long axis. (b) Incident beam intensity dependent MPL intensity from several other single connected heterodimers. The incident beam is linearly polarized along the short dimer axis. The AMPL of heterodimers in the step ② is triggered by the same strategy as (a) in advance.The slope values of around two at the pre-AMPL step (red background) indicate two-photon absorption processes. The slope values of fitted line are all greater than two during the post-AMPL step (blue background). The connected heterodimers investigated here are Au200-Al200 (green triangle), Au200-Al180 (red circle), Au200-Al120 (blue asterisk), Au120-Al220 (dark green square), Au120-Al120 (magenta diamond) and Au120-Al180 (black pentagram). The fitted slopes are 2.0, 2.1, 2.0, 2.9, 3.7 and 4.2, respectively.

7.3.2 Influences of the excitation polarization

Another strategy to trigger the AMPL without changing the incident power is to alternate the excitation polarization. As shown in Fig.7.3(a), AMPL is triggered at a single connected Au120-Al180 heterodimer via varying the excitation polarization from along the dimer short axis to the long axis. The dimer long axis is around 80° when a weak excitation intensity (57 $\mathrm{GW/cm^2}$) is used, as can be seen from the dipole-like emission pattern (red dots). The integrated intensities are multiplied by a factor of 10 for a better illustration. The blue dots and squares represent the experimental results obtained around the transition from step ① (before AMPL) to ② (after AMPL), which are excited with an incident intensity of 63 $\mathrm{GW/cm^2}$. The AMPL takes place during the step at which the excitation polarization angle changes from 80° to 100°. The tuning step of excitation polarization is 20°. The time-elapse between two consequential measurements is approximately 20 s.

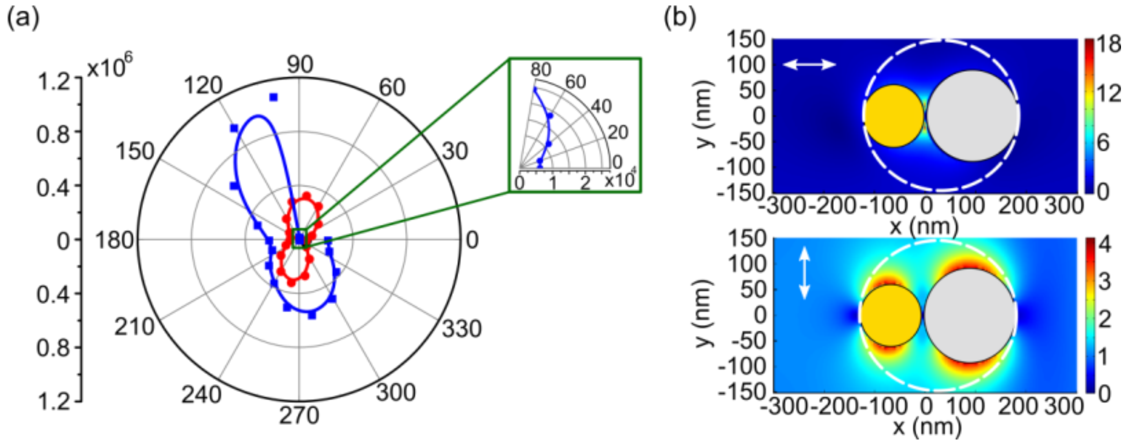

Figure 7.3 (a) The excitation polarization dependent MPL intensity as a step of 20° before (red dots) and during (blue dots in the inset and blue squares) the AMPL occurrence for a single connected Au120-Al180 heterodimer. The incident beam intensity is linearly polarized. The incident intensity in the focus is 57 $\mathrm{GW/cm^2}$ and 63 $\mathrm{GW/cm^2}$ before and during the occurrence of AMPL. The integrated intensities before the AMPL occurrence are multiplied by 10 for a better illustration. The dimer long axis is around 80° as seen in the polar plot. The AMPL takes place when the excitation polarization angle changes from 80° to 100°. The time-delay between two consequential measurements is around 20 s. (b) FDTD simulations of the fundamental near-field distribution under the longitudinal and transverse excitation polarizations for a single Au120-Al180 heterodimer. The double-end arrows in (b) indicate the polarization directions which are either along the dimer long (upper picture) or short (lower picture) axis. The white dashed circles with the diameter of 300 nm mark the areas in which the field enhancement is evaluated.

It is well known that strongly localized field in the nanogap of dimers can be generated when the excitation polarization is along the dimer long axis, which is namely hot-spot. As shown in Fig. 7.3(b), the near-field distributions at the fundamental frequency excited along the dimer long (upper image) and short axis (lower image) are compared. The highest electric field is clearly visible at around the touching point of the heterodimer for the excitation along the long dimer axis. Its field ($E_{longitudinal} = \sqrt{E_x^2 + E_y^2 + E_z^2}$) is more than 4 times stronger than that ($E_{transverse}$) for the excitation along the short dimer axis. An averaged field enhancement factor ratio ($E_{longitudinal} / E_{transeverse}$) of 1.2 is evaluated by taking into account of the areas marked by the dashed white circles in Fig. 7.3(b). What's more, with longitudinal polarization excitation, the electric fields in the hot-spots are parallel to the dimer connections and the electric field can penetrate into the dimers resulting into strong multiphoton absorption.[24] On the contrary, when the incident wave is polarized perpendicular to the dimer long axis, the local electric field is mainly orthogonal to the nanoparticle surface and the internal field is somewhat reduced by the electron screening limiting the absorption process.[24] Thus, the longitudinal excitation enhances not only the local field, but also the far-field MPL radiation.

In summary, the occurrence of AMPL is not only a pure thermal effect, which can be directly triggered by increasing the incident power, but also has close connection with the local field enhancement supported by specific nanostructures. The latter plays an of importance role in the excitation process, which will be discussed in the following.

7.4 Mechanism of AMPL

Comparing with Au NPs, Al NPs rarely luminescent in our experiment, as shown in the Fig. 7.4(a). The Al monomers, and Al-Al homodimers nearly have no MPL signals, while Au-Al heterodimer has the similar MPL as that from the Au monomer of the same size. The sample was taken for optical measurements around one month after the fabrication. The Al NPs could be coated by an oxidation lay of ~5 nm.[101, 102] The PL absence from Al NPs could be due to the oxidized layer rather the luminescent nature of pure Al. One possible reason is that the light-matter interaction will become less active due to the big band gap of alumina. In the mean time, it finds that the nanostructures suffer inevitable thermal damages once AMPL is generated. As show in Fig. 7.4(b), the Au NPs has been reshaped or melted since AMPL takes place. However, the Al NPs almost keep the same shapes as the ones without optical measurement. This might also due to the outer oxidized layer which protects the Al NP from strong thermal damage because of its high melting point. What's more, further evidences show that the Au monomers and homodimers suffer similar thermal reshapes as Au-Al heterodimers. However, this doesn't happen on Al monomers and Al-Al homodimers. Therefore, it's reasonable to attribute the generation of AMPL to the optical breakdown process of Au NPs induced by a strong electromagnetic field.

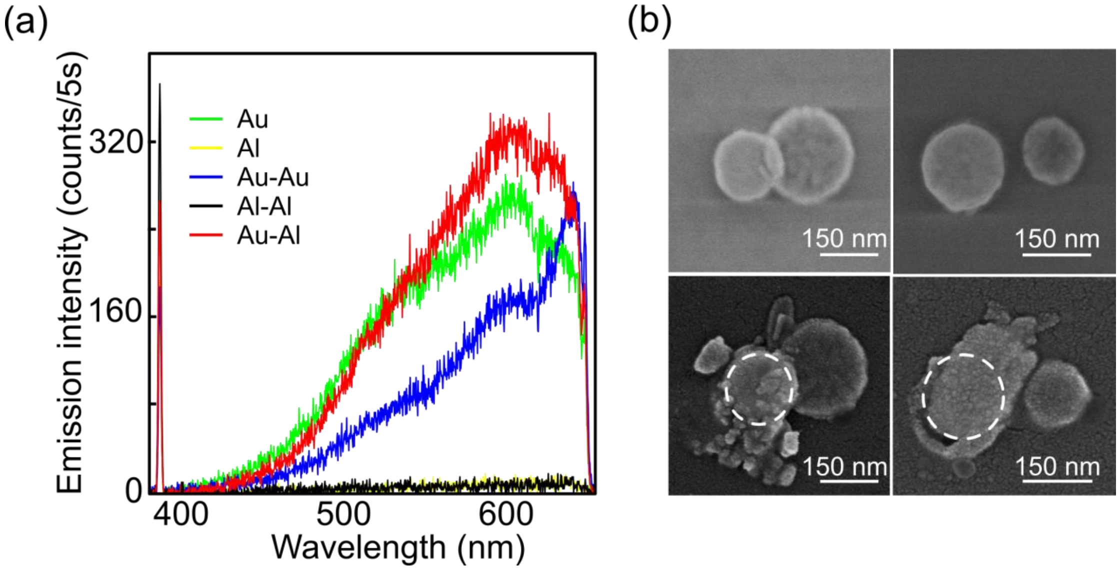

Figure 7.4 (a) Emission spectra of Au monomer (green), Al monomer (yellow), Au-Au dimer (blue), Al-Al dimer (black) and Au-Al dimer (red). The NPs have the same diameter (160 nm) and the dimers have no gap. The incident beam is linearly polarized along the dimer long axis. (b) The SEM images of connected Au160-Al240 (left column) and Au 180-Al120-g40 (right column) heterodimers without (upper row) and with (lower row) the occurrence of AMPL. The heterodimers shown in the upper row are identical as the corresponding lower ones. The white dashed rings indicate the original Au NPs before AMPL occurs.

The excitation of TPL of noble metal in the weak electromagnetic field is described via a sequential absorption of two single photons.[24, 53] In this case, the electron in the *sp*-band below Fermi energy level E_f absorbing the first photon is excited to the conduction band above the E_f via intraband transition, which leaves a hole behind. The second photon excites an electron in the *d*- band, which recombines with the hole created in the previous excitation step. A hole in the d band is then left. The recombination of excited *sp*-band electrons and *d*-band holes give rise to the TPL.[24, 53] The excited electrons achieve, after sub-picosecond thermalization, a thermal equilibrium of the electronic population.[61] Subsequently, the energy is transferred to the cold lattice through electron-phonon and phonon-phonon scatterings. If the electron-phonon coupling as well as the thermal conductivities of the electron and lattice are strong enough, a thermal equilibrium can be reached between the hot and the cold carriers during the emission of photons.

However, this equilibrium can be broken by the interaction with a strong electromagnetic radiation field, where quasi-free electrons in the conduction band can be generated through nonlinear processes such as multiphoton ionization or tunnelling effect.[69] More free carries can be produced through cascade ionization once the free charges gain sufficient kinetic energy from the electromagnetic field.[69] The rapid ionization leads to plasma formation and to a dramatic increase of the absorption coefficient, which in turn give rise to a fast energy transfer from the electric field to the medium.[1, 69] Collisional heating of the electrons occurs before they transfer the energy to the lattice. This heating and energy diffusion, seeded by multiphoton ionization and combined with cascade ionization, result in an electron avalanche.[70] Such huge hot electrons in the conduction bands and hot holes in the valence bands recombine directly and product the giant photons, which finally generates the AMPL.

The ionization of the condense medium induced by a strong electromagnetic field or photoionization (PI) process can be quantitatively described by the Keldysh rate equations.[71] As the dominant PL intensity and the reshaping are dominantly observed at Au nanoparticle (as seen in Fig. 7.4(b)), the discussion about the origin of AMPL on Au NPs is the focus. PI includes the tunneling ionization (TI) and multiphoton ionization (MPI).[71] The contribution between TI and MPI on the full PI can be quantified via the Keldysh parameter γ. In accordance with the Keldysh's theory, when γ is larger than 1, the PI is mainly induced by MPI; when γ is smaller than 1, TI becomes the dominant contribution. The calculation of ionized electron density and Keldysh full rate equation can be found in 'Theoretical background 2.5.2' section.

As shown in Fig.7.5(a), the Keldysh parameter as a function of laser intensity in our tunable range (indicated as grey background) is bigger than 1, which reflects that MPI is the dominant contribution to PI.[71] As also can be seen from Fig.7.5(b), TI (dot line), MPI (dashed line) and PI (solid line) are calculated as functions of incident beam intensity according to the Keldysh rate equation as well. In the tunable range of the laser intensity, PI follows the similar trend as MPI. Based on Figs. 7.5 (a) and (b), it can be seen that the 'seed' electrons are indeed fed by mulitiphoton ionized electrons. This explains the reason why more than two photons will be absorbed during AMPL step, as analyzed in Fig. 7.2.

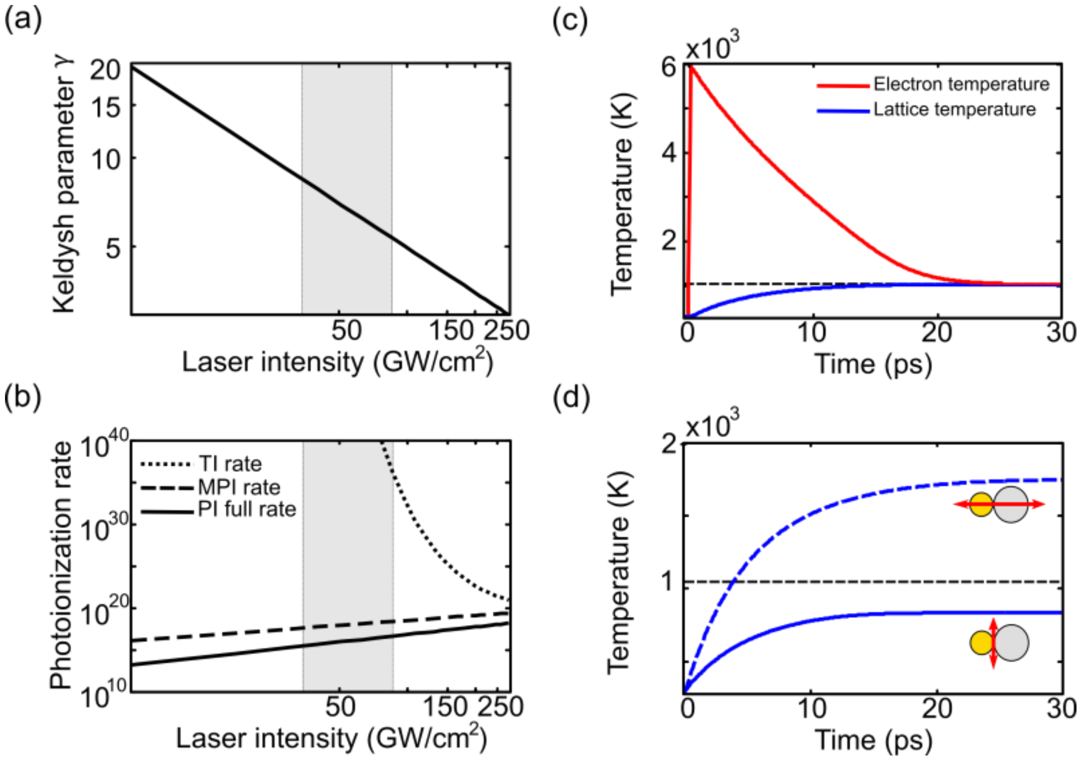

Figure 7.5 (a) The calculated Keldysh parameter as a function of the laser intensity. (b) The calculated TI rate, MPI rate and PI full rate as functions of the laser intensity according to the Keldysh theory. The TI, MPI and PI rates are marked as dot, dashed and solid lines, respectively. (c) Calculated electron (red) and lattice (blue) temperature versus time according to the two temperature model at the critical laser intensity of 71 $\mathrm{GW/cm^2}$. The black horizontal dashed line represents the melting point of Au NPs: 1045 K. (d) Calculated lattice temperature versus time according to the two temperature model at the laser intensity of 63 $\mathrm{GW/cm^2}$ under the transverse (solid curve) and longitudinal (dashed curve) excitation.

The optical breakdown of Au NP induced by a strong electromagnetic field can be evaluated by the two-temperature model (TTM), taking the source term into regard.[62, 64] The criteria adopted here is that the lattice temperature reaches the melting point of Au NP: 1045 K.[64] The temperature dependent electron capacity and electron-phonon coupling are imposed to improve the calculating precision (see 'Theoretical background' section).[66] The calculated electron (red) and lattice (blue) temperature versus time according to TTM at the critical laser intensity of $70.6\mathrm{GW/cm^2}$ is shown in Fig. 7.5(c). The black horizontal dashed line represents the melting point of Au NPs: 1045 K. The initial temperatures of both electron and lattice are set as room temperature (300K). As we can see, the electron and phonon reach the thermal equilibrium after a time scale of tens of picoseconds. The laser intensity is around 70 $\mathrm{GW/cm^2}$ when the maximum lattice temperature reaches the melting point, which agrees with our experimental result shown in Fig. 7.2(a).

TTM is able to evaluate the thermal damage threshold of the bulky metallic material in the focus volume of a strong laser beam. However, the local field enhancement of specific plasmonic structures is omitted. The influence of local field enhancement can be investigated by alternating the excitation polarization. Taking the global local field enhancement factor as 1 when the Au-Al heterodimer in the focus under the transverse excitation, the lattice temperature after the thermalization is below the damage threshold when the incident intensity is 63 $\mathrm{GW/cm^2}$, as shown in Fig. 7.5(d). When the excitation polarization turns to the dimer long axis, the lattice temperature after the thermalization will beyond the threshold taking the averaged field enhancement factor ratio of 1.2 into regard. Therefore, AMPL is triggered.

7.5 Evaluating the emission intensity of AMPL

More interestingly, as shown in Fig. 7.6, the spectrally resolved power law coefficients (slope values) in post-AMPL cases show linear functions of emitted photon energy, rather than keeping a nearly constant of 2 as pre-AMPL. The slope values in the double logarithmic coordinate of the emitted intensity versus each photon energy are plotted with blue marks for the pre-AMPL case, and red marks for the post-AMPL. The phenomenon of power law exponent coefficient as a linear function of the emitted photon energy was well explained by Tobias Haug et. al,[103] which supplies an approach to quantitatively calculate the emission intensity or flux after the occurrence of AMPL.

In the limit $h\nu \gg k_B T_e$, the spontaneous radiative transition rate of Fermi-Dirac distributed conduction-band electrons takes a Boltzmann shape:[103]

$$\phi(\nu) = f(\nu)\exp\left(-\frac{h\nu}{k_B T_e}\right) \tag{7.1}$$

Where h and k_B are the Planck and Boltzmann constants, T_e is the electron temperature and $f(\nu)$ is a function of the photonic mode density.

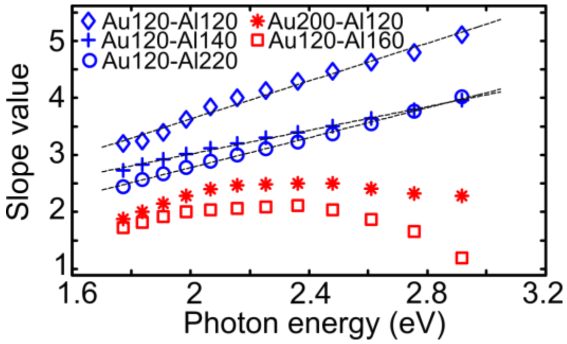

Figure 7.6 Power law coefficients as functions of emitted photon energies in both pre-AMPL (red squares and asterisks) and post-AMPL (blue circles, crosses and diamonds) steps. The power law coefficient (slop value) in the post-AMPL stage is fitted by linear functions (black dashed lines). The connected heterodimers used here are Au120-Al160 (square), Au200-Al120 (asterisks), Au120-Al220 (circle), Au120-Al140 (cross) and Au120-Al120 (diamond). The excitation beam is linearly polarized along the dimer long axis. The red and blue color codes indicate the pre- and post-AMPL processes.

The emission irradiance E is simply assumed to be a power function of T_e and emitted photon energy ν. More generally, let $x \equiv k_B/h\nu$, $E = [T_e(kx+b)]^a$ is assumed, where k and b are constants. Let $T = bT_e$and $K = k/b$, then $E = [T(Kx+1)]^a$ is obtained. When $h\nu \gg k_B T_e$, $x \to 0$, or under the condition $K = 0$ which is the case explained in reference [103]. According to the above equation,

$$log(\emptyset) = \log(f) - \frac{h\nu}{k_B T_e} = \log(f) - \frac{b}{xT} \tag{7.2}$$

Superposing $T = \exp[\log(E)/a]\,/(Kx+1)$ into the above equation, we get

$$log(\emptyset) = \log(f) - b(K + \frac{1}{x})\exp\left[-\frac{1}{a}\log(E)\right] \tag{7.3}$$

Use the first two terms of Taylor series for the exponential term, then

$$log(\emptyset) = \log(f) - b\left(K + \frac{1}{x}\right) + \frac{b}{a}\left(K + \frac{1}{x}\right)\log(E) \tag{7.4}$$

As can be seen from equation (7.4), the power law exponential coefficient $p(\nu) = bh\nu/ak_B + k/a$ shows a linear function of photon energy. $f(\nu)$ has tight connection with its own plasmonic environment, and a depend on the effective excitation cross section and the thermodynamic properties of the nanoscale electron system.[103] Thus, the photon emission of AMPL is a result contributed by the local field environment of a specified plasmonic nanostructure and the thermal effect of hot carriers.

7.6 Spectral interpretation

Dramatic and irreversible spectral change occurs during the AMPL process. During the pre-AMPL step, the MPL of nanostructures shows a predominant LSPR-like profile, which is reported by many studies.[16, 24, 50] As shown in Fig. 7.7(a), the sharp peak at around 650 nm in the PL spectra of a single Au120-Al160-g20 nanodimer reflect the coupling between Au-dipole and Al-dipole modes (plasmon mode 1). As seen the scattering spectra of Au-Al heterodimers in Fig. 7.7(b), which are simulated by FDTD. The Au disc has the same diameter of 120 nm, while the diameter of Al disc varies from 120 nm to 220 nm. The ege-to-ege gap size between Au disc and Al disc is 20 nm. LSPRs situating around 600 nm is marked as plasmon mode 1.The charge distribution of plasmon mode 1 is shown in Fig. 7.7(c), which implies a coupling mode between Au-dipole and Al-dipole mode. This is explained by the fact that in addition to the spontaneous emission via the direct recombination of e-h pairs, there exist extra decay channels via surface plasmon, namely PPs emission channel (see chapter 6). However, during the post-AMPL step, the MPL spectra behave more bulky-like profiles, which show a big broad peak pumping up from 450 nm to maximum wavelength. It is interpreted that e-h pairs emission channel becomes dominant. As shown in the Fig. 7.7(a), AMPL spectrum is compared with the MPL spectrum of 50 nm thickness of Au film. They both show a broad PL centered at around 530 nm, which corresponds to the e-h recombination from near the L symmetric point. The line width broadening could be caused by: 1) emission frequency shifted by interband transitions at other symmetric points from the same or different valence bands; 2) collisional broadening at the high temperature; 3) dephasing broadening due to the morphological inhomogeneities in the NPs ablation process.

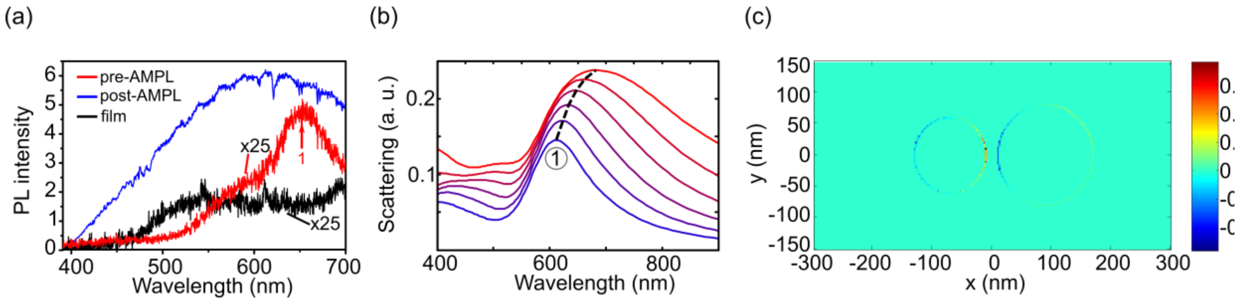

Figure 7.7 (a) PL spectra from the Au film (black) and a single connected Au120-Al160 nanodimer before (red) and after (blue) the AMPL occurrence. The integrating time is 50s and 5s for the Au film (50 nm thickness) and Au-Al NPs. For guiding the eyes, the emission signals of Au film and pre-AMPL are multiplied by 25. The incident beam is linearly polarized and has the same intensity in the focus: 63 $\mathrm{GW/cm^2}$. AMPL occurs when the excitation polarization changes. The red arrows indicate the plasmon mode in a longitudinal excitation. (b) The scattering spectra of Au-Al heterodimers. The Au disc has the same diameter of 120 nm, while the diameter of Al disc varies from 120 nm to 220 nm. The ege-to-ege gap size between Au disc and Al disc is 20 nm. LSPRs situating around 600 nm is marked as plasmon mode 1; (c) The charge distribution of plasmon mode 1 for a Au120-Al160-g20 heterodimer.

The spectra conversion from surface-like to bulk-like behavior can be explained by the temperature dependent d hole scattering rate γ_h^s.[57, 58] For the d-hole at the NP center and in dipole approximation, $\gamma_h^s \propto Im(1/\epsilon_s(\omega))$ (the full expression of γ_h^s can be found from "Theoretical background" section or Chapter 6, where $\epsilon_s(\omega) = \epsilon_d(\omega) - \omega_p^2/\omega(\omega + i\gamma_s) + 2\epsilon_0$. ϵ_d is the interband contribution of dielectric function, ω_p is the bulk plasmon frequency of the conduction electrons, γ_s is the damping constant and ϵ_0 is the medium dielectric function. The imaginary part ${\epsilon_s}''$ will increase as temperature due to the rise of electron density via interband transitions and damping constant of the free electrons in the conduction bands. The interband transition part is contributed by the fact that $\Delta{\epsilon_s}''(\hbar\omega) = 1/(\hbar\omega)^2 \int D(E,\hbar\omega)\, \Delta\rho(E) dE$, where $D(E,\hbar\omega)$ is the joint density of states with respect to the energy of E of the final state of the conduction band and $\rho(E)$ is the density of states (see "Theoretical background" section 2.5.1).[68] Especially once the AMPL occurs, ${\epsilon_s}''$ undertakes a sharp rise due to the dramatic increase of electron density. And the d hole scattering rate nearly vanishes. The contribution to the MPL from e-h pairs emission channel becomes dominant with temperature of hot carriers.

What's more, due to the increase of permittivity of the metal (the real part will increase as well in accordance with Kramers-Kronig relationship, see "Theoretical background" section), not only the dominant surface susceptibility $\chi_{\perp\perp\perp}$, but also the bulk susceptibility γ_{bulk} of SHG will decrease, as:[84]

$$\begin{cases} \chi_{\perp\perp\perp} = -\frac{a}{4}[\epsilon_r(\omega) - 1]\frac{e\epsilon_0}{m\omega^2} \\ \gamma_{bulk} = -\frac{d}{8}[\epsilon_r(\omega) - 1]\frac{e\epsilon_0}{m\omega^2} \end{cases} \tag{7.4}$$

where$e$ and m are the electron charge and mass; $\epsilon_0\epsilon_r(\omega)$ indicates the dielectric function of the metal at the frequency of ω. a and d are the Rudnick and Stern parameters, which have the positive values of 1. This explains the decrease of SHG once the AMPL occurs, as shown in the inset of Fig.7.2(a).

7.7 Summary

In this section, AMPL is observed from the strong coupled Au-Al heterodimers once the incident beam exceeds critical laser intensity. The emission intensity turns out approximately more than one order of magnitude larger and encounters dramatic spectral changes. The intrinsic mechanism is interpreted after a series of laser intensity dependent and polarization dependent experiments on the Au-Al heterodimers varying size and gap. The physical mechanism can be well explained via Keldysh's rate equation in strong-field. It is interpreted that AMPL derives from the recombination of avalanche ionized hot carriers seeded by multiphoton ionization. The multiphoton ionization is greatly assisted by the dramatic local field of coupled Au-Al nanoantennas at the excitation stage. The threshold of optical breakdown can be evaluated via TTM, taking the source term into account. The giant photon emission of AMPL can be quantitatively defined as a function of local field environment of a specific plasmonic nanostructure and the thermal factor of hot carriers. The spectral change from the LSPR modulated profile to the one that indicates the direct recombination from hot electron-hole pair is explained by the diminishment of d-band hole scattering rate as the carriers' temperature increases.

In practice, the experimental results of surface-enhanced Raman scattering or surface-enhanced fluorescence for single molecules should take special care that such huge radiation from the nanoantennas is excluded. On the other hand, the AMPL can be further explored to be as a powerful tool and give assistance to the surface-enhanced spectroscopy and microscopy.The surface enhanced spectroscopy and currently emerged laser-induced breakdown spectroscopy could be benefited from this investigation as well.

Chapter 8 Conclusions and outlooks

The influences of material, size and shape on the linear and nonlinear optical responses of plasmonic nanostructures are systematically investigated. The materials studied here involve gold and aluminum, the surface plasmon resonances of which are tunable ranging from visible to infrared and from ultraviolet to visible spectral regimes, respectively. In order to explore the coupling effects of plasmonic systems, homodimers (Au-Au dimer and Al-Al dimer) and heteodimers (Au-Al dimer) are investigated by varying the size and spacing respectively. The nanostructures are fabricated by EBL followed by lift-off. The linear optical properties of plasmonic nanostrtures are characterized by extinction spectroscopy and dark-field scattering spectroscopy. The nonlinear optical properties are investigated by confocal scanning optical microscopy combining with a femtosecond pulsed laser. The thermodynamics of nanostructure are studied in terms of the power- and polarization-dependence.

In parallel, theoretical modelling involving different theories in the field of linear, nonlinear optics and thermodynamics are performed. To be exact, linear optical responses such as the extinction, scattering or absorption of plasmonic nanostructures of different dimensions, shapes and spacing are simulated by various approaches, e. g. Mie theory, GTM and FDTD method. The nonlinear optical responses such as SHG and TPL are analyzed with the assistance of SIE method. Different models based on the electrodynamics and thermodynamics are adapted to help us to obtain better physical interpretations of MPL radiation in weak and strong electromagnetic fields, respectively.

Regarding the nonlinear optical responses of plasmonic nanoantennas, my work emphasises on SHG and MPL. For SHG, flips of the polarization-dependent far-field radiation pattern are observed. The potential causes are attributed to the resonant excitation condition and SH phase interference with the size changes. The first factor is quantitatively analyzed via GTM, and the latter by SIE method. Our results clearly point out that the characterization of electromagnetic hot-spots using nonlinear optical processes is not straightforward, since competition between different contributions from parameters, such as polarization, geometry and resonance, to the electric field enhancement often occur.

Regarding the MPL, far-field radiations in weak and strong electromagnetic field are studied respectively. The terms 'weak' and 'strong' are defined in terms of the threshold of optical breakdown induced by ultrafast laser pulses. The threshold is strongly related with the laser properties and material properties. In a weak excitation, the MPL emitted from smooth Au films and Au NPs via ultrafast laser pulses in a scanning confocal optical microscope is systematically investigated. By comparing the emission spectra from Au films and Au NPs of varying dimensions with the dark-field scattering spectra, it is found that the MPL consists of two contributions, namely the PPs emission mode and the e-h pairs emission mode. The similar behaviour between PP-mediated MPL with the corresponding scattering in terms of peak position and FWHM strongly suggests that this part indeed originates from the radiative decay of PPs. The PPs are excited via Auger scattering of photo-excited d band holes.[51] The e-h pairs emission mode has the same radiation energies of e-h recombination from X and L high symmetric points, and strong intensity dependence on the 'resonant excitation', which can be quantified by a Lorentzian oscillator. This part of emission is attributed to the radiative decay of e-h pairs. A model of TEQE involving both contributions is established to discuss the radiative emission capability per e-h pair, and explain the size effect regarding the PL difference between the bulk, e.g. film, and the NPs. The experiment results and the theoretical model supply a new approach to calculate MPL.

AMPL is observed from strongly coupled Au-Al heterodimers once the incident beam exceeds the critical laser intensity. The emission intensity is approximately more than one order of magnitude larger than the case without its occurrence and shows dramatic spectral changes. The intrinsic mechanism is interpreted after a series of laser intensity dependent and polarization dependent experiments on the Au-Al heterodimers of varying sizes and gaps. The physical mechanism is explained via Keldysh's rate equation in strong-field. It is interpreted that AMPL derives from the recombination of avalanche ionized hot carriers seeded by MI. The MI is greatly assisted by the local field of coupled Au-Al nanoantennas at the excitation stage. The threshold for inducing optical breakdown can be evaluated via TTM, taking the source term into account. The strong AMPL intensity can be evaluated as a function of local field environment of a specific plasmonic nanostructure and the thermal factor of hot carriers. The spectral change from the LSPR modulated profile to the one that indicates the direct recombination from hot e-h pair is explained by the diminishment of d-band hole scattering rate as the carriers' temperature increases.

Due to the limited time and resources, some specific problems are still waiting for the proper solutions. Single Au, Al monomers and homodimers have been systematically investigated. The understanding of the coupling among the homodimers is relatively straightforward, as the dipole-dipole interaction always dominant. However, the situation becomes more complicate when heterodimers are used. Beside the dipole-dipole modes, other coupling schemes like dipole-quadruple, quadruple-quadruple modes from different materials present. Furthermore, if the influence of LSPRs on the interband transitions is taken into account, e.g. the LSPRs of Al NPs affect the interband transition of Au NPs or the other way round, the analysis of the dimer optical properties will becomes more complex. In this dissertation, the linear optical responses of Au-Al heterodimer are studied in a general way rather than going to details to analyse all possible plasmon modes for each dimer configuration. Further work can be conducted concerning this issue.

The most complicated case, which might be beyond the current study, is the contacted heterodimer. Charge transfer between Au and Al NPs might have to be considered during the interaction between the light and nanostructures. In the strong electromagnetic field, the heterodimer could even be treated as alloy NPs. The simulations including linear and nonlinear calculations about contacted heterodimers are still rarely reported. Further studies on this issue could also be interesting and promising.

Flips of the polarization-dependent far-field SHG radiation pattern depending on the size and gap may lead to potential applications on the antenna, the identifier and sensor. For example, the size difference down to several nm due to the temperature changes can be easily detected if the flip of far-field SHG radiation occurs.

The emission channels of MPL in the weak electromagnetic field have been systematically investigated during my Ph.D work. The emission nature of MPL has been discussed, which supplies a way in theory to understand the emission channels and predict the MPL spectra. This does not only give some hints to better understand the fundamental light-matter interaction mechanism, but also to improve state-of-art techniques of the surface enhanced spectroscopy and microscopy. AMPL occurs often in practice, even though not many studies pay enough attentions, which becomes one of my main concerns. The related investigation supplies a way to predict the optical breakdown threshold and to protect the NPs from damaging. Other applications on the surfaced-enhanced spectroscopy and microscopy are also promising.

Résumé

Les nanostructures métalliques présentent des propriétés optiques linéaires et non linéaires fascinantes lorsqu'elles sont excitées par la lumière incidente. Les plasmons de surface localisés générés par une oscillation collective d'électrons dans les bandes de conduction offrent la possibilité d'exalter et de concentrer le champ électrique dans un volume de dimensionsub-longueur d'onde, ce qui permet aux nanostructures d'agir de manière similaire aux antennes dans le régime des micro-ondes ou des ondes radio. Leurs applications potentielles dans divers domaines, allant de la biosensibilité, des systèmes de collection de lumière, aux transistors à effet de champ ont motivé les chercheurs à comprendre leurs propriétés physiques fondamentales et leurs processus optiques. Les influences des résonances plasmoniques de surface localisées (LSPR) sur les propriétés optiques linéaires des nanoantennesplasmoniques, telles que l'absorption, la diffusion et l'émission de photoluminescence à photonunique ont été intensément étudiées. Pour étudier l'amplitude du champ électromagnétique dans les prétendus points chauds optiques, correspondant aux zones où l'intensité du champ incident est renforcée deplusieurs ordres de grandeur, les chercheurs se sont appuyés sur plusieurs techniques spectroscopiques telles que l'émission de photoluminescence des nanostructures métalliques, la fluorescence ou la diffusion Raman provenant de molécules qui sont immobilisées sur la surface desnanoantennes, et aussi la spectroscopie de perte d'énergie électronique. Plus récemment, l'observation des processus optiques non linéaires à partir de nanoantennesplasmoniques commence à attirer une attention croissante. Différents procédés optiques non linéaires, tels que la génération de seconde harmonique (SHG), la photoluminescence à deux photons (TPL), la génération de troisième harmonique, ainsi que la photoluminescence multiphotons ont été étudiés. Par rapport aux processus optiques linéaires, la génération de signaux optiques non linéaires nécessite une intensité de champ d'excitation beaucoup plus élevée. Les

nanoantennesplasmoniques peuvent être utilisées pour l'excitation de ces processus optiques puisque l'intensité du champ à la longueur d'onde fondamentale est augmentée dans leur voisinage grâce au LSPR.

Dans cette thèse, les nanoantennesplasmoniques sont systématiquement étudiées, impliquant la fabrication et la caractérisation. La lithographie par faisceau d'électrons est imposée comme la principale technique de fabrication, car elle fournit des formes régulières et de haute résolution et des nanostructures reproductibles. Le matériauest axé sur l’or et l’aluminiumen raison de leur capacité accordable de LSPR dans lagamme visible. Les objets de recherche incluent les monomères et les dimères simples avec une taille, une interdistance, une forme et un environnement diélectrique variables. Les propriétés optiques comprennent la diffusion élastique et les réponses non linéaires telles que le SHG et la photoluminescence métallique (MPL). Les méthodes de simulation correspondantes sont étudiées entretemps. En comparant les propriétés optiques pourune faible excitation, il existe des différences dramatiques pour les signaux optiques non linéaires lorsque les nanostructures plasmoniques sont dans un champ électromagnétique fort, ce qui nécessite des recherches essentielles sur l'électrodynamique ou une dynamique thermique plus générale.

L'ensemble de la thèse est organisé comme suit:

Chapitre 1 Introduction. L'état de l'art et l'organisation de la thèse complète seront présentés ici.

Chapitre 2 - Contexte théorique. Dans cette section, les théories fondamentales et les modèles qui seront utilisés dans les sections suivantes sont introduits. Les théories couvrent les domaines de plasmonique, de diffusion élastique, d'optique non linéaire, d'électrodynamique et de thermodynamique.

Dans le domaine de la plasmonique, les plasmons de surface de propagation et les LSP sont introduits, respectivement. La relation de dispersion du polariton de plasmon de surface et la polarisation d'une nanoparticule sphérique (NP) en approximation quasi-statique sont discutées entretemps. La théorie de Mie est introduite ultérieurement, proposant une approche pour calculer quantitativement les réponses optiques linéaires d'une nanostructure plasmonique. L'interaction lumière-matière peut être considérée analogiquement comme la vibration mécanique sous la force d'entraînement périodique pour un système amorti, qui est également le principe de l'oscillateur Lorentzien. De telles analogies mécaniques sont nécessaires pour mieux comprendre les LSPR, l'excitation résonnante et surtout les couplages entre deux ou plusieurs nanoparticules. Nous commençons par un système unique à un degré de liberté, puis généralisons les principales conclusions du système àdegrés de liberté multiples. Les réponses optiques non linéaires telles que SHG et TPL sont introduites suite aux propriétés linéaires. Leurs origines physiques et leurs principes de calcul théorique sont décrits en détail. Lorsque le laser à impulsions ultra-rapide est utilisé, la chaleur devient un problème inévitable en raison de l'intensité crête élevée et du taux de répétition ultra-rapide. Beaucoup d'études dans la littérature ont étudié l'électrodynamique aussi longtemps que le film métallique ou NP évite d'être endommagé. Néanmoins, au-delà du seuilde la dégradation optique induite par le laser à impulsions et du processus, les signaux optiques non linéaires impliquant SHG et TPL présententde nombreuses caractéristiquesnouvelles, auxquelles aucune attention n'a été accordée à notre connaissance. L'interprétation complète des nouveaux effets non linéaires nécessite la connaissance de l'électrodynamique et de la thermodynamique plus généralisée. Dans cette section, le modèle à deux températures, les changements de fonction diélectrique induits par la dynamique des populations d'électrons et la théorie de Keldysh dans un fort rayonnement électromagnétique,sont présentés et seront utilisés dans les chapitres suivants.

Chapitre 3 - matériaux et méthodes. Dans cette section, les configurations pour la fabrication, la caractérisation optique linéaire et non linéaire sont présentées. Des méthodes de simulation multiples sont également introduites.

Les matériaux que nous avons étudiés ici sontl'or et l'aluminium, dont les résonances de plasmon de surface peuvent être accordables, allant respectivement du domaine visibleaux infrarouges et ultraviolets. Afin d'explorer les effets de couplage de différents systèmes, des dimères impliquant des homodimères (dimère Au-Au et dimère Al-Al) et des hétérodimères (dimère Au-Al) ont été étudiés en faisant varier la taille et l'espacement séparément. Les nanostructures ont été fabriquées par lithographie par faisceau d'électrons, puis par décollage. La lithographie à double électron, qui est responsable de la fabrication des hétérodimères, est également décrite. Les propriétés optiques linéaires des nanotechnologies plasmoniques ont été caractérisées par une microscopie d'extinction et une microscopie de diffusion enchamp sombre. Les parties non linéaires ont été étudiées par microscopie optique à balayage confocalecombiné à àunlaser à impulsions femtosecondes. Le miroir parabolique sert à la fois comme élément de focalisation et collecteur de l'émission. Dans l'air, l’ouverture numérique ou NA atteint 0,998. Un tel miroir à haute NA et à faible dispersion chromatique permet une haute résolution jusqu'à la limite de diffraction. La thermodynamique de la nanostructure a été étudiée en termes de dépendance à la puissance et de dépendance à la polarisation dans le microscope à balayage confocal.

En parallèle, des modélisations théoriques impliquant différentes théories sur l'optique linéaire, non linéaire et la thermodynamique ont été réalisées. Plus précisément, les réponses optiques linéaires telles que l'extinction, la diffusion ou l'absorption de nanostructures plasmoniques de différentes dimensions, formes et interdistances ont été simulées par diverses approches, telles que la théorie Mie, la méthode du tenseur de Green(GTM), la méthode des conditions auxlimites (BEM) et laméthode de des différences finiesendomaine temporel (FDTD). La diffusion élastique peut normalement être simulée par FDTD. C'est une méthode de pointe pour résoudre les équations de Maxwell dans des géométries complexes. Étant une solution directe entemps et espace, elle offre un aperçu unique de la plupart des types de problèmes d'électromagnétisme et de photonique. Dans les cas généraux, tels que les monomères, les homodimères et les hétérodimères, la FDTD peut fournir des résultats appropriés. Nous allons présenter cette méthode au chapitre 4 pour traiter la plupart des cas simples. Cependant, afin de simuler la diffusion du champ sombre conformément à nos conditions expérimentales, telles que la simulation de l'angle de focalisation et de l'angle de collecte, la méthodeGTM volumique a été utilisée pour affiner la modélisation.

Le SHG et la MPL, en particulier la TPL, sont nos principales cibles d'investigation en termes de réponses optiques non linéaires. Pour divulguer l'origine physique des réponses TPL et SHG et expliquer les résultats des expériences, des simulations numériques ont été réalisées avec un code de méthode d'intégration de surface interne (SIE) donnant des résultats précis pour les distributions de champ proche et champ lointain, même dans des conditions de résonance. Nous analysons le SHG de surface des NP avecl'aide avec la méthode SIE. Il est bien connu que le SHG est interdit pour des milieux centro-symétriques dans l'approximation dipolaire. Néanmoins, cette symétrie est cassée à l'interface entre deux milieux centro-symétriques, et la SHG apparaît sur des surfaces de nanostructures métalliques. Les méthodes SIE nécessitent uniquement la discrétisation des surfaces des NP métalliques, làoù les sources SHG sont situées, et sont donc extrêmement bien adaptées pour un calcul SHG précis. Pour comparer les résultats numériques avec les observations expérimentales, l'intensité SH est intégrée sur un hémisphère reproduisant la collection de lumière réalisée par le miroir parabolique.

L'approche utilisée pour l'évaluation du signal TPL est fondamentalement différente en raison de son origine physique distincte. Contrairement à la SHG, qui est un processus de surface cohérent, la TPL est un processus impliquant l'excitation d'une paire électron-trou (eh) par l'absorption de deux photons incidents, la relaxation de l'électron et du trou excités et l'émission de lumière due à la recombinaison de l'électron avec le trou. Le calcul numérique de la TPL induit par la recombinaison directe de paire e-h peut se référer aux travaux de G. T. Boyd dans la partie théorique. La LSPR joue également un rôle important dans les processus d'excitation et de rayonnement de la TPL, dont l'influence sera discutée au chapitre 6.

Chapitre 4 - diffusion élastique de Au et Al nanoantennas. Les propriétés de diffusion élastique reflètent les LSPR de nanoantennes spécifiques, ce qui est la première étape pour interpréter les mécanismes d'exaltation de la spectroscopie d’exaltation de surface. Dans cette section, les spectres de diffusion enchamp sombre des nanoantennes Au et Al seront présentés. Les systèmes d'investigation comprennent les monomères Au et Al, les homodimères Au-Au et Al-Al et les hétérodimères Au-Al. Pour chaque système, les dépendances de lataille des nanoparticules et de leur espacement(pour les homodimères) sont étudiées dans différentes polarisations d'excitation. L'évolution générale des LSPR pour chaque système est notre objectif, plutôt que dediscuterendétail les modes plasmon pour chaque nanostructure. La description du microscope de diffusion enchamp sombre se trouve au chapitre 3. LaFDTD est utilisée pour calculer les spectres de diffusion élastique et les distributions de charge, afin de spécifier le mode plasmon de surface. En guise de simplification, une onde plane se propageant selon la direction Z représentera le schéma d'illumination du microscope de diffusion enchamp noir réel, et seuls les modes dipolaires électriques sont pris en compte. Des modèles plus précis seront introduits dans les sections suivantes pour traiter des problèmes spécifiques.

Le monomère Au a un diamètre variant de 80 nm à 200 nm par pas de 20 nm. Le monomère Al a un diamètre variant de 120 nm à 220 nm par pas de 20 nm. L'homodimère Au-Au a la même variationdede diamètre NP que le monomère Au, et l'écart entre deux NPsAu passe ducontact (aucun espacement), à 20 nm, 40 nm, 60 nm, 100 nm jusqu'à 250 nm. L'homodimère Al-Al a la même variationde diamètre de NP que le monomère Al, et l'écart entre deux NPsAl reste le même que pour les homodimères Au-Au. Nous fabriquons également des hétérodimères Au (d1) -Al (d2), où d1 estle diamètre desNP Au et d2 celui des NP Al. D1 varie de 80 nm à 200 nm par pas de 20 nm. Pour chaque diamètre de Au NP (d1), le diamètre de Al NP (d2) varie de 120 nm à 220 nm par pas de 20 nm. L'écart entre les NP Au et les NP Al dans un hétérodimèrepassedu contact (sans espace), à 20 nm, 40 nm, 60 nm, 100 et plasmiques. La simulation correspondante dela diffusion élastique utilisant la FDTD est comparée aux résultats expérimentaux. Nous résumons ici certaines règles générales de l'accord entre l'expérience et la simulation:

(A) dépendance en taille

À mesure que la taille de lananoantenneplasmonique augmente, laLSPR aura un décalage vers le rouge. La raison peut être expliquée phénoménologiquement par la diminution de la force de rappel.

(B) dépendance à l'écart

Les dimères en contact sont apparemment différents des dimères avec espacementlorsque la polarisation d'excitation est le long de l'axe long du dimère, dont le mode plasmon sera discuté en détail au chapitre 5. Pour les dimères avec des écarts, il on observe clairementque lorsque la polarisation de l'excitation est le long de l'axe du dimère, la position du pic subitgénéralement un décalage vers le bleu lorsque l'espace augmente et se rapprochedesmonomères correspondants. Il est facile de comprendre qu'un dimère avec un écart tendant vers l’infini devrait avoir le même comportement que le monomère correspondant. Dans l'excitation de polarisation transversale, cependant, les spectres de diffusion sont presque les mêmes, ce qui signifie que l'écart n'influence pas autant la LSPR.

(C) dépendance à la polarisation

Les LSPR se situent toujours à des longueurs d'onde plus élevées lorsque la polarisation d'excitation est le long de l'axe long du dimère que lorsque la polarisation d'excitation est le long de l'axe court du dimère. Cela s'explique par le fait que dans l'excitation longitudinale, le dimère a un effet de couplage plus fort que dans le cas de l'excitation transversale.

(D) dépendance en matériau

Les LSPR des NP Au peuvent être facilement accordéesdu régime visible vers l'infrarouge. Cependant, la gamme accordable pour les NP Al va du régime ultraviolet au régime visible. Par exemple, les LSPR des monomères Au dans notre cas varient de 600 nm à 800 nm, et les LSPR des monomères Al changent de 450 nm à 650 nm. L'accordabilité du LSPR desNP Au pour réduire la longueur d'onde (par exemple 550 nm) ou pour avoir la LSPR des NPAl à une longueur d'onde plus élevée (par exemple 800 nm) devient difficile car les transitions interbandes pour les deux matériaux ont de grandes possibilités de se produire pendant l'excitation.

Le cas de l'hétérodimère devient plus compliqué, car nous devons prendre en compte plusieurs modes de couplage plasmon, les transitions interbandes pour un matériau spécifiqueet l'influence de la résonance plasmonique d'un matériau sur la transition interbandes d'un autre matériau. Dans le cas idéal, unerésonance de type Fanoest également possible.

Chapitre 5 - Rayonnement SHG de champs étendus de différents types de nanoantennes.

Les nanoantennesplasmoniques peuvent être utilisées pour l'excitation de ces procédés optiques puisque l'intensité du champ à la longueur d'onde fondamentale est augmentée dans leur voisinage grâce aux LSPR. Étant donné que le rendement de conversion des processus optiques non linéaires varie de manière non linéaire avec l'intensité fondamentale, on peut s'attendre à ce que ce rendement de conversion augmente avec la quatrième ou une puissance supérieure avec le facteur de champ local évalué à la fréquence fondamentale. Pour cette raison, il a été proposé d'utiliser des processus optiques non linéaires pour mesurer avec précision l'exaltation du champ dans les points chauds électromagnétiques, p.ex. des nano-gap, profitant de cette dépendance non linéaire. Cependant, une telle description des processus optiques non linéaires dans les nanoantennesplasmoniques est quelque peu limitée. Par exemple, en raison des règles de sélection spécifiques, laSHG de minuscules nano-lacunes centrosymétrique est faible, malgré une forte amélioration du champ fondamental. En conséquence, les relations entre l'exaltation du champ et les rendements de conversion des différents processus optiques non linéaires doivent être soigneusement déterminées et maîtrisées avant qu'elles ne puissent être utilisés en toute sécurité pour caractériser l'amplitude du champ électromagnétique dans les points chauds.

À partir de l'observation expérimentale, nous constatons que le rayonnement de champ lointain dépendant de la polarisation d'excitation de SHG montre un basculementlorsque la taille desnanoantennes Au change. Pour être exact, l'intensité SHG est maximale pour un faisceau incident polarisé le long de l'axe du dimère pour les plus petits diamètres (d = 80 nm et 100 nm), alors qu'il est maximal pour une onde incidente polarisée perpendiculairement à l'axe du dimère pour les plus grands diamètres (d> 115 nm). Pour illustrer les évolutions progressives des dépendances de polarisation à mesure que la taille du nanodimère change, des simulations ont été effectuées pour des dimères connectés avec des diamètres de disque allant de 70 nm à 180 nm par pas de 10 nm. Un ratio d'intensité R = (a-b) / (a + b) est introduit pour quantifier l'orientation des diagrammes polaires, qui représentent les dépendances de la polarisation d'excitation des signaux SHG, où a et b sont les valeurs d'intensité axiale dans les diagrammes polaires,le long de l'axe du dimère et perpendiculairement àl'axe du dimère, respectivement. Avec cette définition, un changement dans le signe de R décrit un basculementdu rapport d'intensité entre a et b pourladépendance de la polarisationd'excitation. L'évolution de R en simulation s'accorde très bien avec nos résultats expérimentaux.

L'influence de la répartition locale de l'intensité du champ proche sur les processus d'excitation et d'émission de SHG est discutée en faisant varier les résonances plasmoniques des nanostructures et la polarisation du faisceau incident, pourun système modèle constitué de nanodimères connectés. Dans le cas de l'excitation longitudinale, deux types différents de modes plasmon sont observés dans les spectres de diffusion. Le premier mode apparaît entre 500 nm et 610 nm, correspondant au couplage entre deux modes quadrupolaires, et le second mode, qui résonne à une longueur d'onde d'environ 820 nm pour les plus petits diamètres, est un mode dipolaire longitudinal. Pour la lumière incidente polarisée perpendiculairement à l'axe du dimère, on observe un mode dipolaire transversal entre 570 nm et 680 nm. Pour les dimères à diamètres de disque les plus petits, on observe des champs proches forts aux fréquences fondamentales et aux fréquences SHG autour du dimère, en raison de l'excitation résonnante du mode dipolaire longitudinal à la longueur d'onde fondamentale. Par conséquent, l'intensité SHG maximale est obtenue pour une onde incidente polarisée le long de l'axe du dimère. A mesure que le diamètre du disque augmente, la résonance du mode dipolaire longitudinal s'éloigne de la longueur d'onde d'excitation. D'autre part, la résonance du mode dipolaire transversal se rapproche progressivement de la longueur d'onde fondamentale et, finalement, l'emporte sur l'intensité de champ proche pour une polarisation incidente le long de l'axe du dimère. Par conséquent, les diagrammesde dépendance à la polarisation SHG basculentà mesure que la taille des particules augmente.

Les interférencesliéesàla phase SHG joue également un rôle important surle rayonnement, du champ proche au champ lointain. Notamment, pour les dimères avec des diamètres de disque d = 150 nm et 175 nm, bien que des points chauds électromagnétiques forts,aux fréquences SHG, puissent être observés autour des points de contact entre les nanodisques lorsque l'onde incidente est polarisée le long de l'axe du dimère, l'intensité SHG est plus faibleque pour la polarisation perpendiculaireàl'axe du dimère. Ce phénomène a été signalé comme l'«extinction» de la réponse non linéaire de second ordre. Bien qu'une forte exaltation du champ proche soit présente, les vecteurs de polarisation non linéaires de chaque côté du point de contact sont en opposition de phaseet leurs contributions à l'onde SHG de champ lointain ont tendance à s'annuler. L'interférence destructrice entraîne finalement un signal SH de champ lointain faible, malgré l'amplitude de la polarisation de surface non linéaire. Notez que cet effet d'extinction est présent dans tous les dimères connectés, mais entraîne un basculement de la réponse SHG uniquement lorquelaSHG pour une onde incidente polarisée perpendiculairement à l'axe du dimère est suffisamment élevée.

Cette observation de l'effet de basculementSHG indique que la mesure des points chauds électromagnétiques utilisant des processus optiques non linéaires n'est pas directe, car une concurrence entre différents mécanismes d'exaltation de la réponse non linéaire se produit souvent, nécessitant une description minutieuse des mécanismes sous-jacents. Pour comprendre ce phénomène il faut tenir compte à la fois de la résonance plasmon et de la polarisation du champ proche local au «point chaud» électromagnétique.

Chapitre 6 - Rayonnement MPL dans un champ électromagnétique faible. Dans cette section, le mécanisme d'émission de MPL dans pour une faible excitation électromagnétique est discuté parune description classique et au-delà de celle-ci.

La description classique de l'émission MPL est attribuée à la recombinaison d'électrons excités dans les bandes de conduction supérieures (au-dessus du niveau d'énergie de Fermi Ef) et detrous dans les bandes inférieures de valence. Les émissions spectrales sont donc principalement déterminées par leurs propriétés matérielles intrinsèques, e. g. les bandes d'énergie. Ce mécanisme explique avec succès la plupart des résultats expérimentaux pour unfilm métallique ou pour uncristal volumineux. Lessurfaces rugueuses donne habituellement un signal MPL beaucoup plus fort en raison de l'effet de seuild'illumination, où l'exaltation du champ local est renforcée par les plasmons de particules (PP). C'est aussi la raison pour laquelle les étudesde MPL sur les NP deviennent de plus en plus importantes en raison de leur dépendance vis-à-vis des PP, sur leurs formes individuelles, leur taille et leur environnement diélectrique. Le rôle des PP sur l'émission de MPL est généralement considéré comme un renforcement du champ local, ce qui permet de modifier le taux de désexcitation radiative lors de la recombinaison électron-trou. Néanmoins, de plus en plus de preuves montrent que la MPL se comporte de manière similaire aux étalages de champ lointain, qui donne les empreintes digitales des PP. L'émission de MPL est alors attribuée à la désexcitation radiative des niveaux d'énergie des PP. Les PP fournissent non seulement une exaltation du champ local pour l'excitation et la recombinaison directe e-h, mais aussi des canaux de désexcitationsupplémentaires pour les électrons excités. De cette façon, les propriétés de surface des NP, telles que la taille, la forme et l'environnement diélectrique, dominent le comportement d'émission de MPL.

Résumé

Nous étudions systématiquement la MPL émise par des films minces Au et des NP Au sous l'excitationd'impulsions laser ultra-rapides dans un microscope optique confocal à balayage. En comparant les spectres d'émission des films minces Au et de NP Au de dimensions variables avec les spectres de diffusion enchamp sombre, on constate que la MPL comporte deux contributions, à savoir le mode plasmonde particule(PP) et les paires électron-trou (eh). Les comportements similaires entre la MPL couplée aux PP avec la spectroscopie dediffusion correspondante en termes de position de pics, de largeur de pic FWHM et de dépendance enpuissance 6 de l'intensité émise en fonction de lala taille des NP confirment que cette émission provient en effet de la désexcitation radiative des PP. Les PP sont excités par la diffusion Auger de trous dans labande d, photo excités pendant les recombinaisons e-h non radiatives.

Nous utilisons la même méthode phénoménologique pour prédire les spectres d'émission induits par les transitions interbandesendifférents points de symétrieélevés. On constate que les modede paires e-hontles mêmes énergies de rayonnement que ceux dela recombinaison e-h à partir des points symétriques X et L de la première zone Brillouin. L'évolution de l'intensité MPL,évaluée à partir du mode de paires e-h, est également étudiée en fonction du diamètre du disque. En particulier, une tendance plus claire peut être trouvée si l'intensité intégrée devient une fonction de la différence de longueur d'onde Δλ entre le λplasmondesPPset la longueur d'onded'excitation λ fondamentale (774 nm). Nous pouvons constater que laMPL des paires e-h augmente lorsquela valeur absolue Δλ diminue et atteint unmaximum lorsque Δλ s'approche de zéro. Ce phénomène correspond exactement à à un effet d'excitation résonnante. Le mode d'émission des paires e-h est alors attribué à une désexcitationradiative des paires e-hexaltée par plasmons. En combinant ces deux modes d'émission MPL, les spectres d'émission peuvent être prédits quantitativement.

Un modèle d'efficacité quantique totale d'émission impliquant les deux contributions est établi pour quantifier la capacité d'émission radiative par paire e-h, et expliquer l'effet de taille des NP sur le signal MPL en comparaison avec un film mince. Les résultats de l'expérience et le modèle théorique fournissent une nouvelle approche vers un calcul quantitatif de laMPL.

Chapitre 7 - photoluminescence multiphotons d'avalanche (AMPL) dans un champ électromagnétique fort. LaMPL dans un régime de forte excitation électromagnétique où les effets thermiques ne peuvent être négligés, est observé en termes de changements spectaculaires sur l'intensité d'émission et sur le profil spectral, en comparaison avec le cas d'une faible excitation.

Une impulsion laser ultra-rapide est généralement utilisée pour obtenir un MPL conséquent. Le nombrede photons incidentsabsorbéspeut être essentiellement évalué par la pente d'ajustement dans une double coordonnée logarithmique de l'intensité MPL émise par rapport à l'intensité laser incidente, ce qui donnel'exposant de la loi de puissance. La valeur de la pente n'est généralement pas supérieure à deux en raison de la relaxation rapide du premier électron excité dans la bande de conduction. Néanmoins, de nombreuses études ont rapporté que la valeur de la pente peut atteindre 18 dans pour laMPL d'avalanche, notamment pourdesnanofils couplés Au. Un phénomène similaire a été observé à partir deréseauxet de monomères de nanofilsAg. La raison a été attribuée àl'exaltation du champ local apportée par la LSPR ou à un rayonnement purement thermique. Cependant, la nature physique du phénomène n'est toujours pas claire.

La MPL géanteprovenant des nanodimères Au-Al couplés estobservée une fois que le faisceau incident dépasse une intensité critique. À ce stade, l'intensité des émissions est supérieure d'un ordre de grandeur compréeaucas de celle avant le seuil et s'accompagnede changements spectraux spectaculaires. Les coefficients d'exposant de la loi de puissance sont toujours plus grands que 2. LaPL géante irréversible et modifiée spectralementest appelée la photoluminescence multiphotoniqued'avalanche (AMPL). Cependant, entretemps, les nanostructures subissent des dommages thermiques inévitables une fois que l'AMPL est générée. Après une série d'expériences en fonction de l'intensité de la lumière incidente et de la polarisation de l'excitation sur les hétérodimères Au-Al avec des tailles et des écarts variables, nous constatons qu'il s'agit d'un processus thermique dommageable qui engendre lasuper MPL. Outre l'augmentation de l'intensité incidente, une autre stratégie pour déclencher l'AMPL consiste à changerla polarisation d'excitation, où l'exaltation du champ local doit être prise en compte. Il est bien connu qu'il existe un champ local assez fort dans le nanogap de dimères lorsque la polarisation d'excitation est le long de l'axe du dimère, ce qui crée un point chaud. De plus, avec l'excitation de polarisation longitudinale, les champs électriques dans les points chauds sont parallèles aux connexions des dimères et le champ électrique peut pénétrer à l'intérieurdes dimères, ce qui entraîne une forte absorption multiphotonique. Au contraire, lorsque l'onde incidente est polarisée perpendiculairement à l'axe du dimère, le champ électrique local est principalement orthogonal à la surface des nanoparticules et le champ interne est quelque peu réduit par l'écrantagedes électrons, limitant le processus d'absorption.

Le mécanisme physique peut être bien expliqué via l'équation des taux de Keldysh dans le domaine d'excitation forte. Il est interprété que l'AMPL découle de la recombinaison de porteurs chauds excités par ionisation multiphotonique. L'excitation de TPL de métal noble dans le régime de champ électromagnétique faible est habituellement décrite par une absorption séquentielle de deux photons simples. Dans ce cas, l'électron dans la bande de conduction spen dessous du niveau d'énergie de Fermi Efabsorbele premier photon et est excité au-dessus de l'énergie Ef par transition intrabande, ce qui laisse un trou derrière. Le second photon excite un électron dans la bande d de valence, qui se recombine avec le trou créé dans l'étape d'excitation précédente. Un trou dans la bande d est alors laissé. La recombinaison des électrons de la bande spet des trous de la bande d donnent naissance à laTPL.

Avant d'atteindre l'état à partir duquel il y aura une émission, les électrons excités atteignent un équilibre thermique par diffusionélectrons-électrons et électrons-phonons. L'effet de la thermalisation électronique rapide (subps) dans le régime de champfaible est souvent négligé. Cependant, dans un champ électromagnétique fort, des électrons quasi libres dans la bande de conduction peuvent être générés par des processus non linéaires tels que l'ionisation multiphotonique ou l'ionisation tunnel. Ainsi plus de transporteurs libres peuvent être créés par ionisation en cascade une fois que les charges libres gagnent une énergie cinétique suffisante du champ électromagnétique. L'ionisation rapide conduit à la formation d'unplasma et à une augmentation spectaculaire du coefficient d'absorption, ce qui à son tour donne lieu à un transfert d'énergie plus rapide du champ électrique vers le milieu. Le chauffage par collisionnsdes électrons se produit avant letransfertd'énergie vers le réseau. Cette diffusion de chaleur et d'énergie, initié par l'ionisation multiphotonique et combinée à l'ionisation en cascade, entraîne une avalanche d'électrons. La grande quantité résultante d'électrons chauds dans labande de conduction et de trous chauds dans labande de valence se recombinent et produit unnombre important de photons, conduisant à l'AMPL. Une fois que l'avalanche d'électrons est déclenchée, soit en augmentant l'intensité du faisceau incident, soit en exaltant le champ électromagnétique local, une ionisation supplémentaire ne s'arrêtera pas avant que tous les électrons de valence soient ionisés.

L'ionisation multiphotonique est grandement assistée par le champ local exaltédesnanoantennes Au-Al couplées . Cela peut être prouvé par la deuxième stratégie de déclenchement del'effet AMPL. Le seuil de ventilation optique peut être évalué via TTM, en tenant compte du terme source.

Pour ce qui est del'étape de l'émission, il est fondamental que les coefficients d'exposant de la loi de puissance résolus spectralement dans le cas post-AMPL traduisent des fonctions linéaires de l'énergie duphoton émis, alors que dans le caspré-AMPLceux-cisont égaux à 2 pour tout le spectre. Ce phénomène de dépendance linéaire du coefficient d'exposant en fonction linéaire de l'énergie du photon émis a été bien expliqué par Tobias Haug, Sebastian Bange et. Al, qui fournit une approche pour calculer l'intensité ou le flux d'émission après l'apparition de l'AMPL. Enfin, l'émission géante d'AMPL peut être définie comme une fonction de l'environnement local d'une nanostructure plasmonique spécifique et du facteur thermique des porteurs chauds. Le changement spectral du profil d'émission, modulé initialement par le LSPR à celui qui indique unerecombinaison directe à partir d'une paire d'électrons-trous chaud s'explique par la diminution du taux de diffusion des trous de bande dlorsque la température des porteurs augmente.

Dans la pratique, les résultats expérimentaux de diffusion Raman exaltée en surface ou de la fluorescence exaltée en surface pour des molécules simples devraient prendre soin d'exclure un tel rayonnement géantdesnanoantennes. D'autre part, l'AMPL peut être exploréecomme un outil puissant pouraider à la spectroscopie et à la microscopie desurface exaltée. La spectroscopie exaltée desurface et la plus récente spectroscopie de choc induite par laser pourraient bénéficier de cette enquête.

Chapitre 8 - conclusions et perspectives. Les conclusions et les perspectives sont présentées dans la dernière section.

En raison du temps et des ressources limitées, certains problèmes spécifiques attendent toujours les solutions appropriées. Les monomères Au, Al et les homodimères ont fait l'objet d'une enquête systématique. Les couplages parmi les homodimères sont plutôt simples, car les modes d'interaction dipôle-dipôle sont toujours dominants. Cependant, la situation devient très compliquée lorsque les hétérodimères sont introduits. Outre les modes dipôle-dipôle, il existe toujours d'autres schémas de couplage comme les modes dipôle quadruple, quadrupôle-quadrupôle de différents matériaux. En outre, si l'influence des LSPR sur les transitions interbande est prise en considération, par exemple laLSPR des NPAl affectent la transition interbande des NP Au ou l'inverse, l'analyse optique devient plus complexe, et encore moins la polarisation d'excitation est prise en compte. Dans cette dissertation, les réponses optiques linéaires de l'hétérodimère Au-Al sont étudiées d'une manière générale, plutôt qu'en détails pour analyser tous les modes plasmon possibles. D'autres travaux pourraient être menés pour approfondirce problème.

Le cas le plus compliqué, qui pourrait allerau-delà de l'étude actuelle, est le hétérodimèreen contact. Le transfert de charge pourrait être ainsi pris en compte lors de l'interaction entre la lumière et la matière. Dans le régimed'excitationforte, l'hétérodimèrepourrait même être traité comme une NP faite d'un alliage. Les simulations, y compris les calculs linéaires et non linéaires sur le cethétérodimèreen contact manquent encore. D'autres études sur cette question pourraient également être intéressantes et prometteuses.

Le basculement du rayonnement de champ lointain SHG en fonction de la taille et de l'espacement entre particulesmontre les applications potentielles sur les nanoantennes, l'identifiant et les capteurs. Par exemple, unedifférence de taille de quelques nm dus à des changements de température peutêtre facilement détectée si le basculementdu rayonnement SHG dechamp lointain se produit. Les canaux d'émission de la MPL dans le régime de champélectromagnétique faible ont été systématiquement étudiés. La nature des émissions de MPL a été clarifiée, ce qui fournit une théorie en vue de quantifier l'émission et de prédire les spectres MPL. Cela peut aider non seulement les théoriciens sur les matériaux métalliques, mais aussi les expérimentateursenspectroscopieetmicroscopie de surface. L'AMPL se produit toujours en pratique, même si peu d'études y prêtentune attention réelle ou évitent son apparition intentionnellement, ce qui est devenu l'un de nos principaux problèmes. L’étude fournit non seulement un moyen de prédire le seuil optique d’endommagement, maisconstitue aussi une protection pour les NP contre ces dommages thermiques, et enfin des conseils pour des études plus richesen spectroscopie exaltée desurface.

Abstrakt

Die auf Material, Größe und Form abgestimmten plasmonischen Nanostrukturen werden per Elektronenstrahllithographie hergestellt. Ihre linearen und nichtlinearen optischen Signale werden mit einem Dunkelfeldmikroskop bzw. einem konfokalen optischen Mikroskop detektiert. Elastische Streuung plasmonischer Nanopartikel (NPs) zeigt die charakteristischen Peaks der lokalisierten Oberflächenplasmonresonanzen (LSPRs). Sie führen zu einer Verstärkungder nichtlinearen optischen Signale, wie der Erzeugung der zweiten Harmonischen (SHG) und der Zwei-Photonen-Photolumineszenz (PL).

Die SHG verschiedener Nanoantennen wird untersucht. Die anregungspolarisationsabhängige SHG Fernfeldstrahlungzeigt einen Flipping-Efekt. Dieser Effekt hängt von der resonanten Anregung, sowie der SH-Phaseninterferenz bei unterschiedlichen NP Größen ab.Die Ergebnisse zeigen deutlich, dass die Charakterisierung der elektromagnetischen Hotspots per nichtlinearer optischer Prozessen nicht direkt möglich ist. Es kommt zu einer Konkurrenz verschiedener SHG Intensitätsanteile aus Parametern wie Polarisation, Geometrie und Resonanz.

Die Strahlung der metallischen PL (MPL) im schwachen und starken elektromagnetischen Feld wird systematisch untersucht, sowohl durch Experimente als auch per theoretischer Modellierung. Bei schwacher Anregung wird festgestellt, dass MPL zwei Emissionskanäle vorweist: 1) derPartikelplasmonen (PPs) und 2) der Elektron-Loch-Paar (e-h) Emissionskanal. PPs werden überAuger-Streuung optisch angeregter D-Band-Löchern angeregt, dieRelaxationof PPs findet per Abstrahlung über den Emissionskanal 1 statt.Der Zweite Kanal leitet sich aus dem Strahlungszerfall von e-h-Paaren ab. Es wird ein Modell fürdie Gesamtemissionsquanteneffizienz aufgestellt, das die beiden Beiträge berücksichtigt, um die Emissionsfähigkeit pro e-h-Paar zu quantifizieren und denGrößeneinfluss bezüglich

der MPL-Differenz zwischen dem Bulk und den NPs vorherzusagen. Die experimentellen Ergebnisse und das theoretische Modell liefern einen neuen Ansatz zur Vorhersage von MPL.

Bei starken Anregung wird Lawinen-Multiphotonen PL (AMPL) bei stark gekoppelten Au-Al-Heterodimeren beobachtet. Der physikalische Mechanismus lässt sich gut mitKeldyshs Ratengleichungen im starken Feld erklären. Es wird abgeleitet, dass AMPL aus der Rekombination von heißen, ionisierten Lawinen-Ladungsträgern stammt, die durch Multiphotonen-Ionisation (MI) entstehen. Die Anregung der MI nimmt durch das dramatische lokale Feld der gekoppelten Au-Al-Nanoantennen stark zu. Der Schwellwert des optischen Durchbruchs kann unter Berücksichtigung des Quellterms über ein Zwei-Temperaturen-Modell bestimmt werden. Im Emissionsschritt wird experimentell eine lineare Beziehung zwischen dem Potenzgesetzkoeffizienten und der emittierten Photonenenergie beobachtet. Die gigantische AMPL-Intensität kann in Abhängigkeit des lokalen Feldes und einem thermischen Faktor der heißen Ladungsträgerbestimmt werden. Die spektrale Änderung des LSPR-förmingen Profilszu dem, der direkten Rekombination von heißen e-h-Paaren, kann erklärt werden durch die Verringerung der D-Band-Lochstreuungsrate, bei höherer Ladungsträger Temperatur.

References

1. Maier, S. A. *Plasmonics: fundamentals and applications*. Springer Science & Business Media: 2007.

2. Bharadwaj, P.; Deutsch, B.; Novotny, L. Optical antennas. *Advances in Optics and Photonics* 2009, 1, 438-483.

3. Barnes, W. L.; Dereux, A.; Ebbesen, T. W. Surface plasmon subwavelength optics. *Nature* 2003, 424, 824-830.

4. Novotny, L.; Van Hulst, N. Antennas for light. *Nature Photonics* 2011, 5, 83-90.

5. Howes, P. D.; Chandrawati, R.; Stevens, M. M. Colloidal nanoparticles as advanced biological sensors. *Science* 2014, 346, 1247390.

6. Stockman, M. I. Nanoplasmonic sensing and detection. *Science* 2015, 348, 287-288.

7. Acimovic, S. S.; Kreuzer, M. P.; González, M. U.; Quidant, R. Plasmon near-field coupling in metal dimers as a step toward single-molecule sensing. *ACS Nano* 2009, 3, 1231-1237.

8. Ahn, T. K.; Avenson, T. J.; Ballottari, M.; Cheng, Y.-C.; Niyogi, K. K.; Bassi, R.; Fleming, G. R. Architecture of a charge-transfer state regulating light harvesting in a plant antenna protein. *Science* 2008, 320, 794-797.

9. Lin, J.; Li, H.; Zhang, H.; Chen, W. Plasmonic enhancement of photocurrent in MoS2 field-effect-transistor. *Applied Physics Letters* 2013, 102, 203109.

10. Guo, N.; Hu, W.-D.; Chen, X.-S.; Wang, L.; Lu, W. Enhanced plasmonic resonant excitation in a grating gated field-effect transistor with supplemental gates. *Optics Express* 2013, 21, 1606-1614.

11. Grand, J.; Adam, P.-M.; Grimault, A.-S.; Vial, A.; De La Chapelle, M. L.; Bijeon, J.-L.; Kostcheev, S.; Royer, P. Optical extinction spectroscopy of oblate, prolate and ellipsoid shaped gold nanoparticles: experiments and theory. *Plasmonics* 2006, 1, 135-140.

12. Gaiduk, A.; Yorulmaz, M.; Orrit, M. Correlated absorption and photoluminescence of single gold nanoparticles. *ChemPhysChem* 2011, 12, 1536-1541.

13. Wackenhut, F.; Virgilio Failla, A.; Züchner, T.; Steiner, M.; Meixner, A. J. Three-dimensional photoluminescence mapping and emission anisotropy of single gold nanorods. *Applied Physics Letters* 2012, 100, 263102.

14. Konrad, A.; Wackenhut, F.; Hussels, M.; Meixner, A. J.; Brecht, M. Temperature dependent luminescence and dephasing of gold nanorods. *The Journal of Physical Chemistry C* 2013, 117, 21476-21482.

15. Crut, A.; Maioli, P.; Del Fatti, N.; Vallée, F. Optical absorption and scattering spectroscopies of single nano-objects. *Chemical Society Reviews* 2014, 43, 3921-3956.

16. Dulkeith, E.; Niedereichholz, T.; Klar, T.; Feldmann, J.; Von Plessen, G.; Gittins, D.; Mayya, K.; Caruso, F. Plasmon emission in photoexcited gold nanoparticles. *Physical Review B* 2004, 70, 205424.

17. Wilcoxon, J.; Martin, J.; Parsapour, F.; Wiedenman, B.; Kelley, D. Photoluminescence from nanosize gold clusters. *The Journal of chemical physics* 1998, 108, 9137-9143.

18. Boyd, G.; Yu, Z.; Shen, Y. Photoinduced luminescence from the noble metals and its enhancement on roughened surfaces. *Physical Review B* 1986, 33, 7923.

19. Kinkhabwala, A.; Yu, Z.; Fan, S.; Avlasevich, Y.; Müllen, K.; Moerner, W. Large single-molecule fluorescence enhancements produced by a bowtie nanoantenna. *Nature Photonics* 2009, 3, 654-657.

20. Nie, S.; Emory, S. R. Probing single molecules and single nanoparticles by surface-enhanced Raman scattering. *Science* 1997, 275, 1102-1106.

21. Martin, J.; Kociak, M.; Mahfoud, Z.; Proust, J.; Gérard, D.; Plain, J. High-resolution imaging and spectroscopy of multipolar plasmonic resonances in aluminum nanoantennas. *Nano Letters* 2014, 14, 5517-5523.

22. Duan, H.; Fernández-Domínguez, A. I.; Bosman, M.; Maier, S. A.; Yang, J. K. Nanoplasmonics: classical down to the nanometer scale. *Nano Letters* 2012, 12, 1683-1689.

23. Butet, J.; Brevet, P.-F.; Martin, O. J. Optical second-harmonic generation in plasmonic nanostructures: from fundamental principles to advanced applications. *ACS Nano* 2015, 9, 10545-10562.

24. Wang, J.; Butet, J.; Baudrion, A.-L.; Horrer, A.; Lévêque, G.; Martin, O. J.; Meixner, A. J.; Fleischer, M.; Adam, P.-M.; Horneber, A. Direct Comparison of Second Harmonic Generation and Two-Photon Photoluminescence from Single Connected Gold Nanodimers. *The Journal of Physical Chemistry C* 2016, 120, 17699-17710.

25. Bouhelier, A.; Beversluis, M.; Hartschuh, A.; Novotny, L. Near-field second-harmonic generation induced by local field enhancement. *Physical Review Letters* 2003, 90, 013903.

26. Butet, J.; Duboisset, J.; Bachelier, G.; Russier-Antoine, I.; Benichou, E.; Jonin, C.; Brevet, P.-F. Optical second harmonic generation of single metallic nanoparticles embedded in a homogeneous medium. *Nano Letters* 2010, 10, 1717-1721.

27. Horneber, A.; Baudrion, A.-L.; Adam, P.-M.; Meixner, A. J.; Zhang, D. Compositional-asymmetry influenced non-linear optical processes of plasmonic nanoparticle dimers. *Physical Chemistry Chemical Physics* 2013, 15, 8031-8034.

28. Reichenbach, P.; Horneber, A.; Gollmer, D. A.; Hille, A.; Mihaljevic, J.; Schäfer, C.; Kern, D. P.; Meixner, A. J.; Zhang, D.; Fleischer, M. Nonlinear optical point light sources through field enhancement at metallic nanocones. *Optics Express* 2014, 22, 15484-15501.

29. Hajisalem, G.; Nezami, M. S.; Gordon, R. Probing the quantum tunneling limit of plasmonic enhancement by third harmonic generation. *Nano Letters* 2014, 14, 6651-6654.

30. Danckwerts, M.; Novotny, L. Optical frequency mixing at coupled gold nanoparticles. *Physical Review Letters* 2007, 98, 026104.

31. Farrer, R. A.; Butterfield, F. L.; Chen, V. W.; Fourkas, J. T. Highly efficient multiphoton-absorption-induced luminescence from gold nanoparticles. *Nano Letters* 2005, 5, 1139-1142.

32. Kauranen, M.; Zayats, A. V. Nonlinear plasmonics. *Nature Photonics* 2012, 6, 737-748.

33. Husu, H.; Siikanen, R.; Mäkitalo, J.; Lehtolahti, J.; Laukkanen, J.; Kuittinen, M.; Kauranen, M. Metamaterials with tailored nonlinear optical response. *Nano Letters* 2012, 12, 673-677.

34. Shen, S.; Meng, L.; Zhang, Y.; Han, J.; Ma, Z.; Hu, S.; He, Y.; Li, J.; Ren, B.; Shih, T.-M. Plasmon-enhanced second-harmonic generation nanorulers with ultrahigh sensitivities. *Nano Letters* 2015, 15, 6716-6721.

35. Bohren, C. F.; Huffman, D. R. *Absorption and scattering of light by small particles*. John Wiley & Sons: 2008.

36. Blake, R. E. Basic vibration theory. *Shock and vibration handbook* 1961, 1, 2-8.

37. Boyd, R. W. Nonlinear optics. In *Handbook of Laser Technology and Applications (Three-Volume Set)*, Taylor & Francis: 2003.

38. Shen, Y.-R. The principles of nonlinear optics. *New York, Wiley-Interscience, 1984, 575 p.* 1984, 1.

39. Loudon, R. *The quantum theory of light*. OUP Oxford: 2000.

40. Dadap, J. I. Optical second-harmonic scattering from cylindrical particles. *Physical Review B* 2008, 78, 205322.

41. Simon, H.; Mitchell, D.; Watson, J. Optical second-harmonic generation with surface plasmons in silver films. *Physical Review Letters* 1974, 33, 1531.

42. Shan, J.; Dadap, J. I.; Stiopkin, I.; Reider, G. A.; Heinz, T. Experimental study of optical second-harmonic scattering from spherical nanoparticles. *Physical Review A* 2006, 73, 023819.

43. Bloembergen, N.; Chang, R. K.; Jha, S.; Lee, C. Optical second-harmonic generation in reflection from media with inversion symmetry. *Physical Review* 1968, 174, 813.

44. Novotny, L.; Hecht, B. *Principles of nano-optics*. Cambridge university press: 2012.

45. Sipe, J.; Moss, D.; Van Driel, H. Phenomenological theory of optical second-and third-harmonic generation from cubic centrosymmetric crystals. *Physical Review B* 1987, 35, 1129.

46. Mooradian, A. Photoluminescence of metals. *Physical Review Letters* 1969, 22, 185.

47. Rosei, R. Temperature modulation of the optical transitions involving the Fermi surface in Ag: Theory. *Physical Review B* 1974, 10, 474.

48. Guerrisi, M.; Rosei, R.; Winsemius, P. Splitting of the interband absorption edge in Au. *Physical Review B* 1975, 12, 557.

49. Rosei, R.; Lynch, D. W. Thermomodulation spectra of Al, Au, and Cu. *Physical Review B* 1972, 5, 3883.

50. Hu, H.; Duan, H.; Yang, J. K.; Shen, Z. X. Plasmon-modulated photoluminescence of individual gold nanostructures. *ACS Nano* 2012, 6, 10147-10155.

51. Shahbazyan, T. V. Theory of plasmon-enhanced metal photoluminescence. *Nano Letters* 2012, 13, 194-198.

52. Jiang, X.-F.; Pan, Y.; Jiang, C.; Zhao, T.; Yuan, P.; Venkatesan, T.; Xu, Q.-H. Excitation nature of two-photon photoluminescence of gold nanorods and coupled gold nanoparticles studied by two-pulse emission modulation spectroscopy. *The Journal of Physical Chemistry Letters* 2013, 4, 1634-1638.

53. Imura, K.; Nagahara, T.; Okamoto, H. Near-field two-photon-induced photoluminescence from single gold nanorods and imaging of plasmon modes. *The Journal of Physical Chemistry B* 2005, 109, 13214-13220.

54. Rosei, R.; Antonangeli, F.; Grassano, U. d Bands position and width in gold from very low temperature thermomodulation measurements. *Surface Science* 1973, 37, 689-699.

55. Christensen, N. E.; Seraphin, B. Relativistic band calculation and the optical properties of gold. *Physical Review B* 1971, 4, 3321.

56. Shahbazyan, T.; Perakis, I.; Bigot, J.-Y. Size-dependent surface plasmon dynamics in metal nanoparticles. *Physical Review Letters* 1998, 81, 3120.

57. Shahbazyan, T.; Perakis, I. Size-dependent correlation effects in the ultrafast optical dynamics of metal nanoparticles. *Physical Review B* 1999, 60, 9090.

58. Shahbazyan, T.; Perakis, I. Surface collective excitations in ultrafast pump-probe spectroscopy of metal nanoparticles. *Chemical Physics* 2000, 251, 37-49.

59. Bouhelier, A.; Bachelot, R.; Lerondel, G.; Kostcheev, S.; Royer, P.; Wiederrecht, G. Surface plasmon characteristics of tunable photoluminescence in single gold nanorods. *Physical Review Letters* 2005, 95, 267405.

60. Horneber, A.; Braun, K.; Rogalski, J.; Leiderer, P.; Meixner, A. J.; Zhang, D. Nonlinear optical imaging of single plasmonic nanoparticles with 30 nm resolution. *Physical Chemistry Chemical Physics* 2015, 17, 21288-21293.

61. Link, S.; Burda, C.; Wang, Z. L.; El-Sayed, M. A. Electron dynamics in gold and gold–silver alloy nanoparticles: The influence of a nonequilibrium electron distribution and the size dependence of the electron–phonon relaxation. *The Journal of Chemical Physics* 1999, 111, 1255-1264.

62. Wellershoff, S.-S.; Hohlfeld, J.; Güdde, J.; Matthias, E. The role of electron–phonon coupling in femtosecond laser damage of metals. *Applied Physics A* 1999, 69, S99-S107.

63. Hohlfeld, J.; Wellershoff, S.-S.; Güdde, J.; Conrad, U.; Jähnke, V.; Matthias, E. Electron and lattice dynamics following optical excitation of metals. *Chemical Physics* 2000, 251, 237-258.

64. Wang, N.; Rokhlin, S.; Farson, D. Ultrafast laser melting of Au nanoparticles: atomistic simulations. *Journal of Nanoparticle Research* 2011, 13, 4491.

65. Chen, J.; Beraun, J.; Grimes, L.; Tzou, D. Modeling of femtosecond laser-induced non-equilibrium deformation in metal films. *International Journal of Solids and Structures* 2002, 39, 3199-3216.

66. Lin, Z.; Zhigilei, L. V.; Celli, V. Electron-phonon coupling and electron heat capacity of metals under conditions of strong electron-phonon nonequilibrium. *Physical Review B* 2008, 77, 075133.

67. Falkovsky, L.; Mishchenko, E. Electron-lattice kinetics of metals heated by ultrashort laser pulses. *Journal of Experimental and Theoretical Physics* 1999, 88, 84-88.

68. Sun, C.-K.; Vallée, F.; Acioli, L.; Ippen, E.; Fujimoto, J. Femtosecond-tunable measurement of electron thermalization in gold. *Physical Review B* 1994, 50, 15337.

69. Noack, J.; Vogel, A. Laser-induced plasma formation in water at nanosecond to femtosecond time scales: calculation of thresholds, absorption coefficients, and energy density. *IEEE Journal of Quantum Electronics* 1999, 35, 1156-1167.

70. Stuart, B. C.; Feit, M. D.; Herman, S.; Rubenchik, A. M.; Shore, B. W.; Perry, M. D. Optical ablation by high-power short-pulse lasers. *Journal of the Optical Society of America B* 1996, 13, 459-468.

71. Keldysh, L. Ionization in the field of a strong electromagnetic wave. *Soviet Physics JETP* 1965, 20, 1307-1314.

72. Ferris, C. Theoretical Modeling of Laser Induced Absorption Phenomena in Optical Materials. Citeseer, 2014.

73. Biagioni, P.; Huang, J.-S.; Hecht, B. Nanoantennas for visible and infrared radiation. *Reports on Progress in Physics* 2012, 75, 024402.

74. Tseng, A. A.; Chen, K.; Chen, C. D.; Ma, K. J. Electron beam lithography in nanoscale fabrication: recent development. *IEEE Transactions on Electronics Packaging Manufacturing* 2003, 26, 141-149.

75. Liu, K.; Avouris, P.; Bucchignano, J.; Martel, R.; Sun, S.; Michl, J. Simple fabrication scheme for sub-10 nm electrode gaps using electron-beam lithography. *Applied Physics Letters* 2002, 80, 865-867.

76. Vieu, C.; Carcenac, F.; Pepin, A.; Chen, Y.; Mejias, M.; Lebib, A.; Manin-Ferlazzo, L.; Couraud, L.; Launois, H. Electron beam lithography: resolution limits and applications. *Applied Surface Science* 2000, 164, 111-117.

77. Jia, K.; Bijeon, J.-L.; Adam, P.-M.; Ionescu, R. E. Large scale fabrication of gold nano-structured substrates via high temperature annealing and their direct use for the LSPR detection of atrazine. *Plasmonics* 2013, 8, 143-151.

78. Lieb, M. A.; Meixner, A. J. A high numerical aperture parabolic mirror as imaging device for confocal microscopy. *Optics Express* 2001, 8, 458-474.

79. Paulus, M.; Gay-Balmaz, P.; Martin, O. J. Accurate and efficient computation of the Green's tensor for stratified media. *Physical Review E* 2000, 62, 5797.

80. Kern, A. M.; Martin, O. J. Surface integral formulation for 3D simulations of plasmonic and high permittivity nanostructures. *Journal of the Optical Society of America A* 2009, 26, 732-740.

81. Butet, J.; Gallinet, B.; Thyagarajan, K.; Martin, O. J. Second-harmonic generation from periodic arrays of arbitrary shape plasmonic nanostructures: a surface integral approach. *Journal of the Optical Society of America B* 2013, 30, 2970-2979.

82. Mäkitalo, J.; Suuriniemi, S.; Kauranen, M. Boundary element method for surface nonlinear optics of nanoparticles. *Optics express* 2011, 19, 23386-23399.

83. Wang, F. X.; Rodríguez, F. J.; Albers, W. M.; Ahorinta, R.; Sipe, J.; Kauranen, M. Surface and bulk contributions to the second-order nonlinear optical response of a gold film. *Physical Review B* 2009, 80, 233402.

84. Bachelier, G.; Butet, J.; Russier-Antoine, I.; Jonin, C.; Benichou, E.; Brevet, P.-F. Origin of optical second-harmonic generation in spherical gold nanoparticles: Local surface and nonlocal bulk contributions. *Physical Review B* 2010, 82, 235403.

85. Thyagarajan, K.; Rivier, S.; Lovera, A.; Martin, O. J. Enhanced second-harmonic generation from double resonant plasmonic antennae. *Optics Express* 2012, 20, 12860-12865.

86. Celebrano, M.; Wu, X.; Baselli, M.; Großmann, S.; Biagioni, P.; Locatelli, A.; De Angelis, C.; Cerullo, G.; Osellame, R.; Hecht, B. Mode matching in multiresonant plasmonic nanoantennas for enhanced second harmonic generation. *Nature Nanotechnology* 2015, 10, 412-417.

87. Aouani, H.; Navarro-Cia, M.; Rahmani, M.; Sidiropoulos, T. P.; Hong, M.; Oulton, R. F.; Maier, S. A. Multiresonant broadband optical antennas as efficient tunable nanosources of second harmonic light. *Nano Letters* 2012, 12, 4997-5002.

88. Ghenuche, P.; Cherukulappurath, S.; Taminiau, T. H.; van Hulst, N. F.; Quidant, R. Spectroscopic mode mapping of resonant plasmon nanoantennas. *Physical Review Letters* 2008, 101, 116805.

89. Black, L.-J.; Wiecha, P. R.; Wang, Y.; De Groot, C.; Paillard, V.; Girard, C.; Muskens, O. L.; Arbouet, A. Tailoring second-harmonic generation in single L-shaped plasmonic nanoantennas from the capacitive to conductive coupling regime. *ACS Photonics* 2015, 2, 1592-1601.

90. Berthelot, J.; Bachelier, G.; Song, M.; Rai, P.; Des Francs, G. C.; Dereux, A.; Bouhelier, A. Silencing and enhancement of second-harmonic generation in optical gap antennas. *Optics Express* 2012, 20, 10498-10508.

91. Butet, J. r. m.; Thyagarajan, K.; Martin, O. J. Ultrasensitive optical shape characterization of gold nanoantennas using second harmonic generation. *Nano Letters* 2013, 13, 1787-1792.

92. Glass, A. M.; Wokaun, A.; Heritage, J.; Bergman, J.; Liao, P.; Olson, D. Enhanced two-photon fluorescence of molecules adsorbed on silver particle films. *Physical Review B* 1981, 24, 4906.

93. Wackenhut, F.; Failla, A. V.; Meixner, A. J. Multicolor microscopy and spectroscopy reveals the physics of the one-photon luminescence in gold nanorods. *The Journal of Physical Chemistry C* 2013, 117, 17870-17877.

94. Zuloaga, J.; Nordlander, P. On the energy shift between near-field and far-field peak intensities in localized plasmon systems. *Nano Letters* 2011, 11, 1280-1283.

95. Hohenester, U.; Trugler, A. Interaction of single molecules with metallic nanoparticles. *IEEE Journal of Selected Topics in Quantum Electronics* 2008, 14, 1430-1440.

96. Biagioni, P.; Celebrano, M.; Savoini, M.; Grancini, G.; Brida, D.; Mátéfi-Tempfli, S.; Mátéfi-Tempfli, M.; Duò, L.; Hecht, B.; Cerullo, G. Dependence of the two-photon photoluminescence yield of gold nanostructures on the laser pulse duration. *Physical Review B* 2009, 80, 045411.

97. Wang, Q.-Q.; Han, J.-B.; Guo, D.-L.; Xiao, S.; Han, Y.-B.; Gong, H.-M.; Zou, X.-W. Highly efficient avalanche multiphoton luminescence from coupled Au nanowires in the visible region. *Nano Letters* 2007, 7, 723-728.

98. Ma, Z.; Yu, Y.; Shen, S.; Dai, H.; Yao, L.; Han, Y.; Wang, X.; Han, J.-B.; Li, L. Origin of the Avalanche-Like Photoluminescence from Metallic Nanowires. *Scientific Reports* 2016, 6.

99. Gong, H.; Zhou, Z.; Xiao, S.; Su, X.; Wang, Q. Strong near-infrared avalanche photoluminescence from Ag nanowire arrays. *Plasmonics* 2008, 3, 59-64.

100. Song, M.; Chen, G.; Liu, Y.; Wu, E.; Zeng, H. Polarization properties of surface plasmon enhanced photoluminescence from a single Ag nanowire. *Optics Express* 2012, 20, 22290-22297.

101. Langhammer, C.; Schwind, M.; Kasemo, B.; Zoric, I. Localized surface plasmon resonances in aluminum nanodisks. *Nano Letters* 2008, 8, 1461-1471.

102. Knight, M. W.; Liu, L.; Wang, Y.; Brown, L.; Mukherjee, S.; King, N. S.; Everitt, H. O.; Nordlander, P.; Halas, N. J. Aluminum plasmonic nanoantennas. *Nano Letters* 2012, 12, 6000-6004.

103. Haug, T.; Klemm, P.; Bange, S.; Lupton, J. M. Hot-electron intraband luminescence from single hot spots in noble-metal nanoparticle films. *Physical Review Letters* 2015, 115, 067403.